The Dynamics of the East Madagascar Current System and Its Influence on the Biological Production Associated to the Shelf -An Observational Study

Master's Thesis in Physical Oceanography

Aksel Voldsund

June the 1st, 2011

UNIVERSITY OF BERGEN
GEOPHYSICAL INSTITUTE

HAVFORSKNINGSINSTITUTTET
INSTITUTE OF MARINE RESEARCH

Acknowledgements

Abstract

The dynamics of the East Madagascar Current (EMC) system, and its influence on the biological production associated to the shelf, is studied by using cruise-data collected onboard the Norwegian R/V. Dr. Fridtjof Nansen between August and October, 2008. The South Equatorial Current (SEC) hits the coast of Madagascar at ∼19°S, bifurcating into a northwards and southwards directed branch of the EMC. The southwards directed branch behaves like a strong (up to 150 cms^{-1}) western boundary current, with a volume transport of ∼26 Sv at 25°S. The volume transport was calculated using geostrophic current profiles adjusted with ADCP measurements at 176 meters depth. At the south-eastern corner of the island, some of the EMC continues south-westwards, and some is retroflected north-eastwards. Cyclonic eddies are expected to be generated inshore of the EMC, while the anticyclonic eddies seem to the shed off the retroflected part of the current.

The currents of the northwards directed branch of the EMC are weaker (up to 60 cms^{-1}) just north of the bifurcation. The volume transport increases between 13.5°S and 12°S. This could be explained by another incoming branch of the SEC. The north-westwards directed volume transport north of the island (12°S) is ∼62 Sv. The wind distribution seems to be the most important factor explaining the current system at the eastern coast.

Wind and current driven upwelling seems to be the most important physical factor stimulating the biological production of the southern and south-eastern coasts. The south-eastern corner of the island could be considered as a biological hot-spot, where a divergent current field contributes to the upwelling. Discharge of nutrient rich water from rivers seems to contribute to the production at the north-eastern coast. The width of the shelf has also turned out to be an important factor.

Contents

Chapter 1

Introduction

Madagascar, the fourth largest island in the world, is located in the South West Indian Ocean (Wright, 1999). The current system at the southern and eastern coast of Madagascar was described by Lutjeharms (2006), and is the basis for the flow field drawn in Figure 1.1. The South Equatorial Current (SEC) flows westward in the Indian Ocean between ∼6°S and 25°S (Swallow *et al.*, 1988). The hitting point of the current at the eastern coast of Madagascar depends on the monsoonal season (Figure 1.2) (Sætre & Da Silva, 1984). When the SEC hits the coast, it bifurcates into a southwards and northwards directed branch of the East Madagascar Current (EMC) (Swallow *et al.*, 1988). The northwards directed branch follows the coast around the northern tip of the island into the Mozambique Channel. The southwards directed branch follows the eastern coast of Madagascar as a relatively narrow western boundary current, close to the coast. The eastern shelf of Madagascar is generally narrow, and the continental slope is steep (Lutjeharms, 2006). When the current reaches the south-eastern corner of the island, it leaves the coast, following the bathymetry. At this location Lutjeharms (2006) expected an upwelling cell (Figure 1.1) to be located inshore of the current.

South of Madagascar, the southwards directed branch of the EMC is perceived to retroflect and cast off eddies and fragments (Lutjeharms *et al.*, 1981). The cyclonic and anticyclonic eddies are travelling south-westwards through the southern region, heading towards the eastern coast of Africa, joining the larger Agulhas current circulation from the Tropics to the Subantarctic (Lutjeharms *et al.*, 1981; de Ruijter *et al.*, 2004). It is important not to separate too much between the EMC and the Agulhas current as they should be seen as two parts of one larger system (Lutjeharms,
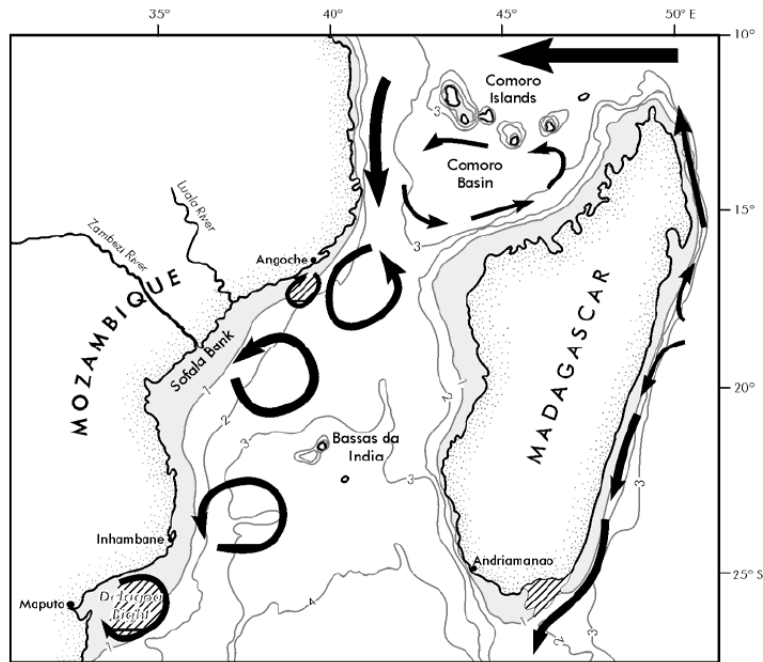
Figure 1.1: *Description of the current system at the eastern coast of Madagascar, with the bifurcation of the SEC into a northwards and southwards directed branch of the EMC. Shaded areas are shallower than 1000 meters and hatched areas denote upwelling (Lutjeharms, 2006).*
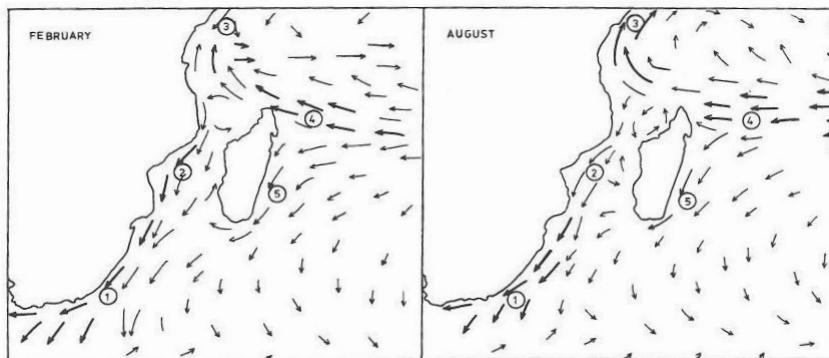
Figure 1.2: *The SEC hitting the coast of Madagascar in two different seasons (Sætre & Da Silva, 1984).*

2006).

Traditionally, there have been little research activity around Madagascar. None of the leading oceanographic research nations share their coastline with the Indian Ocean. Few research vessels has entered it, and even fewer have spent much time there. The situation did not change until the sixties, when more than 40 vessels

from 25 nations participated in the International Indian Ocean Expedition (IIOE) (Tomczak & Godfrey, 2003). Tomczak & Godfrey (2003) states that the hydrography of the Indian ocean still requires much study until a clear picture will emerge. Only certain parts of the shelf regions at the eastern side of Madagascar have been studied intensively, and the current knowledge about the dynamics of the current system relies on a limited and inhomogeneous database (Lutjeharms, 2006). The details of the flow along the coast of Madagascar can not easily be resolved with the available data (Lutjeharms & de Ruijter, 1996). Very little is known about the shelf-circulation inshore of the EMC, neither along the eastern nor along the southern coast of Madagascar, since few hydrographic or current measurements have been made here (Lutjeharms & Machu, 2000). Also when it comes to the biological productivity on the shelf of Madagascar little is known (Lutjeharms, 2006).

Objectives

Most of the studies carried out at the coast of Madagascar are based either on remote sensing methods or by using single point measurements like moorings or drifting buoys (Lutjeharms & Machu, 2000; Lutjeharms *et al.*, 1981). The present study is the first to describe the dynamics of the EMC in its entirety, from in-situ recordings. The data were collected during the East Madagascar Current Ecosystem Survey, conducted from August the 23rd to October the 1st, 2008, by the Norwegian R/V Dr. Fridtjof Nansen.

The main objective of this thesis is to contribute to a better understanding of the dynamics of the East Madagascar Current system, and the relation between the physics and the biological production associated to the shelf of Madagascar. The study of the coupling between the physics and the biology is both interesting and useful. This knowledge is important to be able to manage the fish resources in a responsible way. Without it, it is impossible to explain the patterns of the fisheries, and the synchronous behavior between fish stocks at different locations in the large oceans. This thesis will hopefully be groundwork for further research in this region.

To do this, cruise data will be used. In addition, *MERRA* mean monthly wind, *Sea-WIFS* satellite pictures of sea surface chlorophyll, *Behrenfeld* model of Net Primary Productivity (NPP) through the water column and the *TPXO7.1: Global Inverse Tidal Model* will be used.

General theory and background material with focus on the physics influence on
the biology are given later in this introduction. Chapter 2 contains information
about the data, instrumentation and methods applied in the analysis. Results and
discussion follow in Chapter 3 and 4, respectively. Subsequently, a short summary
with concluding remarks and future work is given in Chapter 5.

Political Background

This project is carried out in co-operation with the Institute of Marine Research
(IMR), and is a part of the Ecosystem Approach to Fisheries management, EAF-
Nansen project. The EAF-Nansen project offers an opportunity to coastal countries
in sub-Saharan Africa, working in partnership with the project, to receive technical
support from Food and Agriculture Organisation of the United Nation (FAO) for the
development of national and regional frameworks for the implementation of Ecosys-
tem Approach to Fisheries management, and to acquire additional knowledge on
their marine ecosystems for their use in planning and monitoring. The project con-
tributes to building the capacity of national fisheries management administrations
in ecological risk assessment methods to identify critical management issues, and
in the preparation, operationalization and tracking the progress of implementation
of fisheries, management plans consistent with the ecosystem approach to fisheries
(EAF-Nansen, 2011).

FAO started the implementation of the project "Strengthening the Knowledge Base
for and Implementing an Ecosystem Approach to Marine Fisheries in Developing
Countries (EAF-Nansen GCP/INT/003/NOR)" in December 2006 with funding
from the Norwegian Agency for Development Cooperation (Norad). The EAF-
Nansen project is a follow-up to earlier projects/programmes in a partnership in-
volving FAO, Norad and the Institute of Marine Research (IMR), Bergen, Norway,
on assessment and management of marine fishery resources in developing countries.
The project works in partnership with governments, and also Global Environmen-
tal Facility (GEF)-supported Large Marine Ecosystem (LME) projects and other
projects that have the potential to contribute to some components of the EAF-
Nansen project (EAF-Nansen, 2011).

The cruise was conducted in cooperation with the United Nation Development Pro-
gram (UNDP)/GEF funded Agulhas and Somali Current Large Marine Ecosystems

(ASCLME) Project (EAF-Nansen, 2011).

Processes on the shelf

Coastal upwelling, shelf-break upwelling, tidal mixing, wind-mixing, breaking of internal waves and river run-off are all important processes for enrichment on the shelf. To understand the dynamics of the phytoplankton production it is necessary to understand the physical processes of vertical distribution of light, heat and nutrients (Mann & Lazier, 2006). The light of the sun penetrates only a short distance below the sea surface, and light levels sufficient to support photosynthesis extend only to a few tens of meters depth. For the photosynthesis to take place, plant cells are using phosphates, nitrates and other nutrient compounds dissolved in the water. The content of nutrients is much higher below the nutricline than above it. The nutricline is usually connected to the pycnocline. The stability of the water column precludes significant transfer of nutrients to the illuminated surface layer. To increase the amount of nutrients in the upper layer (the photic zone), the stratification needs to be broken down. Throughout the open ocean, the energy is carried to larger organisms via a web of trophic levels, where the increasing size of the organisms represent the increasing trophic level. The chlorophyll is at the lowest level and is the basis for all life (Bakun, 1996).

Most phytoplankton cells are denser than water, leading to plant cells being transported out of the illuminated surface layer to the deep ocean. They could e.g. die and sink out of the photic zone, or they could be consumed in the upper layer, transported down to the lower layer, and the nutrients could be released there (Mann & Lazier, 2006; Bakun, 1996). The tropical ocean is often especially stable due to the solar radiation of the upper water. The upward diffusion of nutrients is an extremely slow process (Bakun, 1996).

Because the limiting factor for production at low latitudes are the nutrients, the upwelling has the dominance as a life-giving physical factor of this region (Mann & Lazier, 2006). Some of the most productive regions and largest fish populations of the world ocean, are associated with coastal upwelling systems, where nutrient-rich subsurface water rise to the ocean surface and support high rates of primary production. When the surface drift is away from the coast, influxes of nutrients and properties from the subsurface nutrient pool is brought into the illuminated

surface layer. Coastal upwelling regions also support high populations of seabirds and marine mammals. Areas with a supply of nutrients into the illuminated ocean by upwelling covers only 0.2% of the world ocean, but more than 50% of the fish resources in the world ocean are caught in these areas (Bakun, 1996).

Turbulence and mixing are important processes for the enrichment of the water masses. When the turbulence increases, it seems to have both positive and negative effects on the fish production. The turbulence is important for the first feeding larvae, increasing the encounter rate between the larvae and the food, but it could also break down patches with high concentration of food (Sundby, 1997). Most of the larvae have their habitat in the ocean mixed layer, where the turbulence is mainly wind-driven (Sundby, 1997). Also the coral reefs are dependent on turbulence and mixing, as the primary production and respiration of the coral increases with increasing flow (Mann & Lazier, 2006).

Also important for enrichment, is tidal mixing fronts. The tidal fronts occur over the continental shelves where the tidal currents generate enough turbulence to break down the stratification and completely mix the water column. The stratification could e.g. be set up by a higher surface temperature or fresh water run-off. Tidal mixing has a large influence on the biological production at the continental shelves (Mann & Lazier, 2006). In shallow regions, the turbulence generated by the tidal flows may cause nutrients being redissolved from biological material accumulated at the sea floor to be mixed upward to become available for photosynthesis (Bakun, 1996). Another theory referred to by Mann & Lazier (2006) is related to the movement of the tidal fronts with the cycle of the tidal forces. As the tidal mixing front is moved offshore, new areas with increased amount of nutrients are mixed up, resulting in increased biological production (Pingree *et al.*, 1975).

Internal waves at the shelf-break could contribute to vertical transport of nutrients trapped in the pycnocline. If the internal waves become sufficiently steep, they will break and cause turbulence. The nutrient-rich water from the pycnocline is then mixed into the photic zone, leading to an increased biological production at the shelf-break (Bakun, 1996).

River run-off is another process increasing the amount of nutrients in the surface layer. According to Bakun (1996) the rivers generally contain levels of nutrients that range from a few times to several order of magnitudes higher than the level of nutrients in the surface coastal water. This makes estuaries and ocean areas outside the mouth very productive segments of the marine habitat. In general, the amount

of nutrients in the run-off water has increased during the latest 100 years due to human activity. The small coastal rivers generally carries larger amount of nutrients per volume than the large rivers (Bakun, 1996).

At large shallow banks, or over the continental shelf, the organic matter can sink only to the depth of the shallow sea region, which is within, or at least not far, from the photic zone. The nutrients are often trapped in the pycnocline. Important for the enrichment of the water masses of the upper layer, is also mixing of the waters from the pycnocline up into the photic zone (Bakun, 1996).

The biological production in the research area is generally very small. This could be explained by the sharp pycnocline found in tropical waters (Mann & Lazier, 2006). When referred to large and small amounts of fish in this thesis, it is relative to the standard of the region.

When it comes to fisheries, the observed patterns from these cruise data are very much the same as the observations by Sætre *et al.* (1983) during the cruise carried out by the former R/V Dr. Fridtjof Nansen in June 1983. This cruise was carried out from the southern coast to 17°S. During this first cruise by R/V Dr. Fridtjof Nansen, the objective was to cover the shelf area shallower than 200 meters. This was done by a combined acoustic/trawl survey. Information on fish abundance, species composition and some hydrographic work was carried out. This cruise did not include the long hydrographical transects, and current measurements. The hydrographical profiles were only carried out to maximum 1000 meters depth.

River Run-off

The rivers with outflow at the eastern coast of Madagascar, are in general shorter than those with outflow at the western coast of the island. This could be explained by looking at the topography of the island, with high chains of mountains, splitting the island in two from north to south. The drainage divide is located at the eastern side of the island. Hence, the drainage basins are larger for the rivers flowing westwards to the Mozambique Channel, than for those flowing eastwards to the Indian Ocean (Aldegheri, 1972).

The Global River Discharge Database shows the average monthly discharge from some of the rivers on the eastern coast of Madagascar. There are large seasonal variations in the discharge, but a general trend for all the three rivers representing
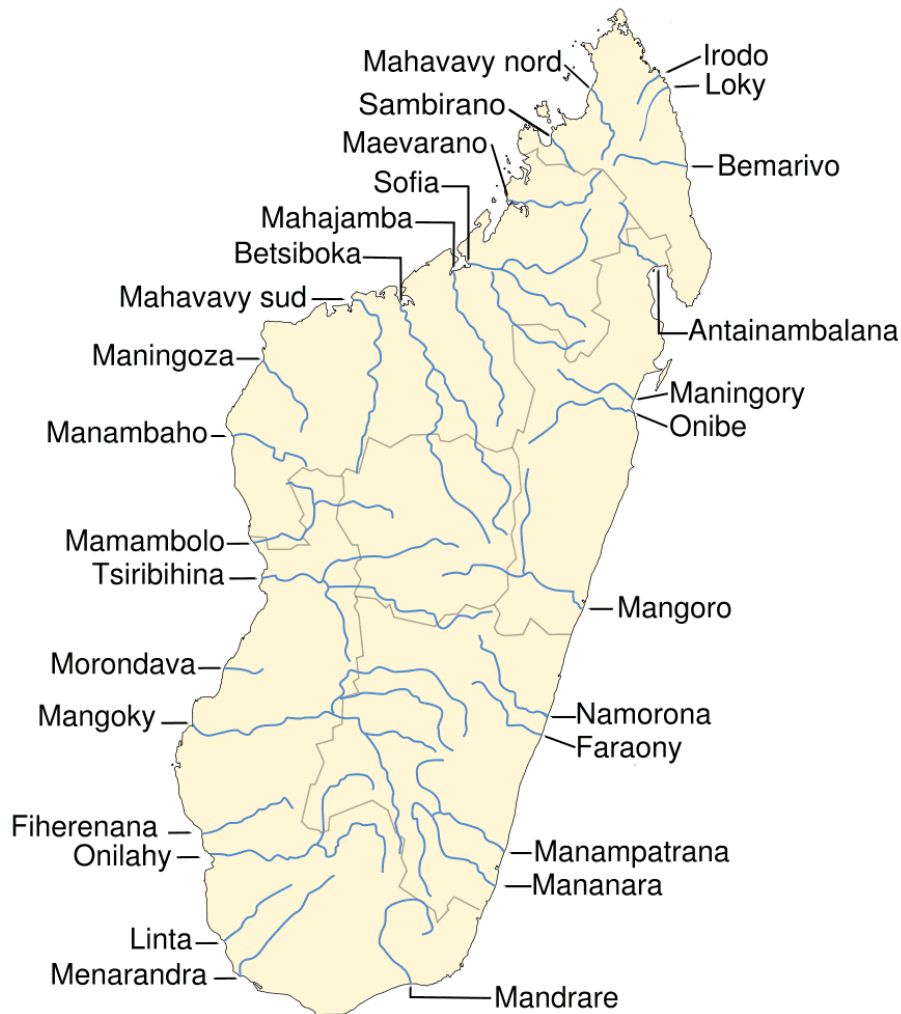
Figure 1.3: *The main rivers of Madagascar (Maps of the World, 2011)*

the eastern coast is that the discharge is at its absolutely minimum in September in an average year. Many of the smaller rivers were completely dry during the period of the cruise (Center for Sustainability and the Global Environment, 2010).

According to Aldegheri (1972), the main rivers with run-off into the Indian Ocean are from south to north Mananara (23°20'S), Mananjary (21°15'S), Mangoro (20°S), Rianila (19°S) and Maningory(17°12'S). Not all the rivers are indicated at the map. The Mangoro river is the largest when it comes to both drainage basin and volume transport.

Chapter 2

Data, Instrumentation and Methods

2.1   The Cruise

Cruise-data presented in this thesis were collected during the East Madagascar Current Ecosystem Survey conducted from August the 23rd to October the 1st, 2008. The cruise was concentrated on the southern and eastern Madagascar shelf, with focus on both biological and physical data sampling. Further details about the cruise are given in the cruise report (Krakstad *et al.*, 2008). In addition, both satellite data and models are used to improve the picture of the study area, as the cruise data are limited and not synoptic.

Table 2.1: *Geographical regions with boundaries and CTD-stations*

Region	Geographical boundaries	CTD stations
South	South of 25°15'S	852 - 894
South-east	25°15'S to 19°S	895 - 912 and 914 - 921
North-east	North of 19°S	922 - 966

The division of the research area is based on the bathymetry (Figure 2.1) and the current system (Figure 3.1), with a wide shelf and eddies in the southern region, a narrow shelf and the southwards directed branch of the EMC in the south-eastern region and the northwards directed branch of the EMC in the north-eastern region.

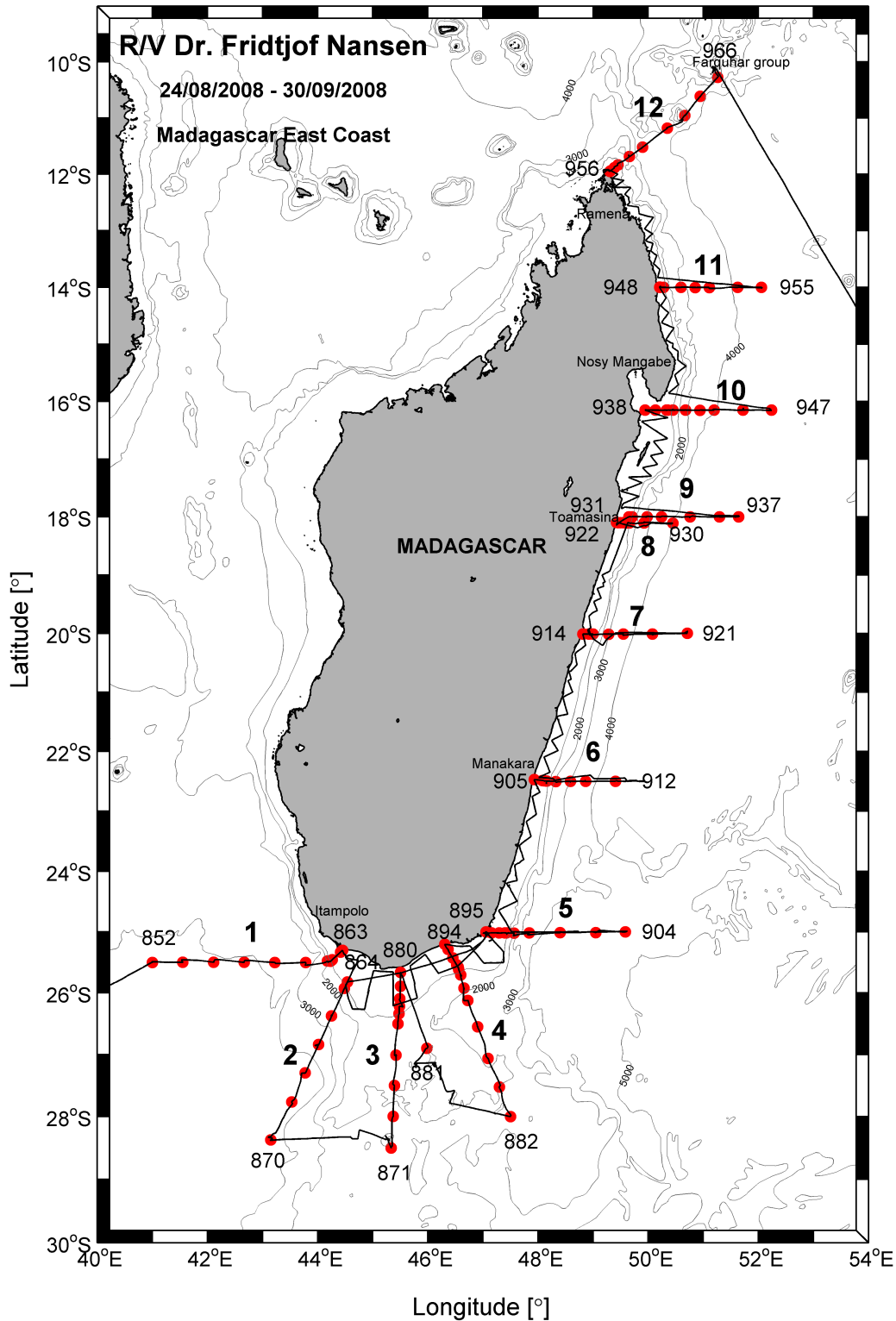**Figure 2.1:** *Map of the survey area with 1000, 2000, 3000, 4000 and 5000 meters isobaths. Vessel course track and hydrographical (CTD) stations are indicated. Hydrographical transects are labeled with bold fonts.*

2.2 ADCP

A vessel mounted 150 kHz Ocean Surveyor Acoustic Doppler Current Profiler (ADCP) from RD Instruments was run continuously during the cruise. The ADCP was set to ping synchronously with the echo sounder (Simrad ER60). The number of bins was set to 120, with a vertical bin-size of 4 meters and a blanking distance of 14 meters if the depth was more than 400 meters, and a vertical bin-size of 3 meters and a blanking distance of 16 meters if the depth was less than 400 meters (Krakstad *et al.*, 2008). The blanking distance is needed to avoid disturbances from the vessel. The typical velocity accuracy is ± 0.5 cms^{-1} and the measurement range is -5 ms^{-1} to 9 ms^{-1} (Teledyne RD Instruments, 2008).

The ADCP measurements did not have first priority. This was due to a compromise to optimize sampling of trawl catch data and carrying out hydrographical transects (CTD). Due to this, several uncertainties were introduced in addition to the natural uncertainties which appear when we are trying to describe the large scale current system by using ADCP-data. The two most outstanding problems were: (1) spurious data in the recordings caused by frequent changes in the ship's speed and direction and; (2) uncertainties related to non-synoptic measurements. The last one introduces problems with short-term fluctuations as tides, current meanders and wind intensifications (Ostrowski, 2005).

During the post-processing of the data, the bin-size was set to 12 meters and the blanking distance was set to 14 meters independent of depth. This makes data from shallow and deep areas comparable. All measurements from the ADCP where the vessel held less than 7 knots were removed. The speed of the vessel was used as a proxy for other processes disturbing the data (e.g. trawling and CTD). In addition, all measurements where the vessel changed direction more than 10 degrees or it changed velocity more than 2 knots during the averaging interval (3 minutes) were deleted. All data reported from the firmware WinADCP, with Percent-Good (PG) less than 98 were eliminated as well. By using four beams instead of three, it is possible to compare the results by excluding the beams one by one, and then use the four results to find an average value and the inaccuracy. The PG screening is performed on the data averaged in time and space (Teledyne RD Instruments, 2000). Current velocities of more than 200 cms^{-1} were removed, as this is physically unlikely in the research area.

The short-term averages (STA) files had to be reprocessed during the post-processing,

as the averaging interval was set to only 10 seconds during the cruise. This is too short to see any regular patterns in the data. The reprocessed STA-files are averaged over 3 minutes, a period short enough to be seen as a single point measurement. The long-term averages (LTA) files on the other hand were averaged over 20 minutes, and were less affected by small short time disturbances. In this thesis the LTA-files will only be used for verification of the STA-files. The STA-files are showing the same patterns as the LTA-files with a much higher number of data points. This is especially important in the shallow areas close to the coast where the vessel is changing direction frequently. Velocity and direction of the vessel are based on the STA-files recorded by WinADCP (Teledyne RD Instruments, 2001).

Because of disturbances from the vessel, the first bin is often removed, as it is considered unreliable. In this thesis each of the bins consists of 3 or 4 smaller bins dependent on the depth. This makes the first bin more reliable, and it will be used to resolve the currents at the shallow southern shelf. The depths given in the figures represent the middle of the 12 meters bins.

A weakness of the ADCP, which should be kept in mind during this thesis, is that it could be problematic measuring the speed of the water at steep slopes. Steep slopes are found at the shelf-break in the entire research area. It should also be noted that the resolution is dependent on time, and not space, hence low velocities would result in smaller spatial distances between the measurements. In relation to hydrographic- and trawl-stations the vessel could make turns, and thus measure the current velocities of the same area twice.

2.3   Thermosalinograph

The thermosalinograph used during this survey is a SBE 21 SEACAT, equipped with an in-line Turner Design SCUFA fluorimeter measuring the Sea Surface Fluorescence (SSF) in $\mu g l^{-1}$ (Krakstad *et al.*, 2008). The fluorescence is a proxy for the content of Chlorophyll-a (Chl-a). The thermosalinograph was run continuously, sampling the relative Sea Surface Temperature (SST), the Sea Surface Salinity (SSS) and the SSF at 5 meters depth every 10 seconds during the entire cruise.

When interpreting the plots based on the thermosalinograph data, it is important to keep in mind that the values are interpolated using linear interpolation, hence interpolation errors might appear. Between Transect 10 and Transect 11 (Figure

Table 2.2: *Range, initial accuracy and resolution of the sensors, S=Siemens (Sea-Bird Electronics, 2010b).*

	Range	Initial Accuracy	Resolution
Conductivity [Sm^{-1}]	0 - 7	0.001	0.0001
Temperature [°C]	-5 - 35	0.01	0.01

2.1) measurements are missing.

The data are reprocessed with the *Software Version Seasave Win32 V 5.30b*. In addition, spikes in temperature and salinity were removed manually. Errors in the thermosalinograph data could be related to washing of the instrument every night at 24 o'clock or mix-up of subsurface water by the vessel at the hydrographical and trawl stations.

2.4   CTD

The Conductivity Temperature Depth (CTD) profiler used during the survey was the Sea-bird's 911 plus CTD system, consisting of an Underwater Unit; the SBE9 plus, and a Deck Unit for real-time readout. The Underwater Unit was equipped with SBE 4C conductivity sensor, SBE 3 plus temperature sensor, Paroscientific Digiquarz pressure sensor, SBE 43 Dissolved Oxygen sensor and Chelsea Mk III Aquatracka fluorimeter. Range, initial accuracy and resolution of the different sensors are given in Table 2.3.

In addition to the sensors, the CTD is equipped with niskin bottles for water sampling, mounted on a SBE32 carousel. The water samples are used for calibration of the oxygen and conductivity sensor.

Table 2.3: *Range, initial accuracy and resolution of the sensors, S = Siemens (Sea-Bird Electronics, 2010a; Chelsea Technologies, 2008).*

	Range	Initial Accuracy	Resolution
Conductivity [Sm^{-1}]	0.0 - 7.0	0.0003	0.00004 at 24 Hz
Temperature [°C]	-5 - +35	0.001	0.0003 at 24 $sampl.s^{-1}$
Diss. Oxygen [mll^{-1}]	120% of surf. sat.	2% of sat.	
Fluorescence [μgl^{-1}]	0.01 - 100	0.02	0.01

The software communicating with the CTD is *SEASAVE Win 32 V 5.30a*. After the data are collected, the post-processing software, *SEASOFT*, filters the data, removes obviously bad measurements and consider problems like e.g. surface waves. In the end, the *SEASOFT* program runs the routine *Derive*, calculating oceanic parameters like e.g. density, depth, potential temperature and salinity by using the pressure, temperature and conductivity from the converted datafile. Everything done by the software is listed in the header of the CNV-file (Sea-Bird Electronics, 2003).

In addition to the post-processing carried out by the software, the resulting profiles are rinsed further manually by removing unrealistic spikes in both salinity and fluorescence. No manual despiking was carried out for temperature and oxygen.

At some of the hydrographical stations, there were taken several water samples for calibration of the conductivity and oxygen sensors. The samples were analyzed at the vessel using the Winklers method for oxygen and a Portsal salinometer for salinity. The following calibrations was obtained:

- Oxygen: y=1.0201x+0.2192

- Salinity: y=0.9961x

Factory slope and offset of the fluorimeter were 0.921 and -0.02 (Krakstad *et al.*, 2008).

The calibrations indicate that the measurements from the CTD are good, and as no statistics are included in the cruise report together with the calibrations, the data will be kept uncalibrated.

The hydrographical profiles are plotted from 6 meters depth down to a few meters above the seabed, or maximum 3000 meters depth. All plots are plotted with the coast to the left. As the gradients are usually much steeper in the upper layer, plots of upper 250 meters are made to emphasize the features of the upper layer. Due to low resolution of hydrographical stations close to the shelf-break in some of the transects, it is important to be aware of the possibility of interpolation errors above the shelf-break.

2.5 Meteorological Measurements

A WIMDA meteorological station was used for measuring the meteorological parameters during the entire cruise. The wind data were averaged over 10 minutes. In this thesis the wind is plotted with vectors showing magnitude and direction, making comparison with the ocean currents easier.

2.6 Models

MERRA Reanalysis of Wind

The *Modern Era Retrospective-analysis for Research and Applications* (MERRA) (Global Modeling and Assimilation Office (GMAO), 2010) is used for reanalysis of wind-data in 10 meters height. The temporal resolution was set to one hour, and the gridded spatial resolution was set to 50×50 kilometers. The reanalysis contributes to a more synoptic picture of the wind-field during the cruise. Monthly means are made for looking at the dominating wind directions of the season with respect to the current system. Details about the MERRA model can be found at the models web-page: `http://gmao.gsfc.nasa.gov/research/merra/intro.php`.

Tides

To look at the tidal currents' influence on the in-situ current (ADCP) measurements, the *TPXO7.1:Global Inverse Tide Model* (Egbert & Erofeeva, 2002) was applied. The tidal components in u (east-west) and v (north-south) direction were calculated at the same time and position, as the current (ADCP) measurements were carried out. In addition to the 10 most influencing constituents, the total water depth is taken into account for the calculation of the tidal currents. The model was validated with respect to sea surface elevation by Inocência (2011) at the coast of Mozambique in March 2011 with good results. For more information about the model see: `http://polaris.esr.org/ptm_index.html`.

2.7   Phytoplankton by Satellite Remote Sensing

To look at the content of chlorophyll in the sea surface, satellite remote sensing is applied. The satellite used for this purpose was NASA's Sea-viewing Wide Field-of-view Sensor (SeaWIFS), circling around the earth picturing the ocean surface for more than ten years (1998 - 2007). This does not cover the period of the cruise, which was carried out in 2008, but by plotting mean values for the octets (8 days) through 10 years it is possible to locate areas with in average high or low content of chlorophyll in the surface layer. The content of chlorophyll in the surface is calculated by looking at the color of the surface water.

Calculated chlorophyll in the surface layer is used as input in the Behrenfeld model, integrating and estimating the NPP of phytoplankton through the photic later of the water column in $mg\ C\ m^{-2}\ day^{-1}$, where C is carbon. The output of the model is gridded, with a grid size of 9 kilometers. More information about the model could be found in (Behrenfeld & Falkowski, 1997a) and (Behrenfeld & Falkowski, 1997b). The use of satellite remote sensing will be important during this thesis to find what areas to concentrate on, as the literature is limited. The satellite remote sensing also contributes in making a more generalized picture of the situation.

In shallow waters, problems may occur as a consequence of the difficulties of separating between the sea floor shining through the water column and the color of the water due to high concentrations of chlorophyll. At the eastern coast of Madagascar the shelf is relatively steep. Hence, the region related to this problem is not too large. On the other hand, the chlorophyll concentrations on the shelf is the most interesting in this study.

2.8   Matlab Tools

To make plots, calculations and maps, Rich Pawlowiczs oceanographic Matlab tool-boxes *Seawater, Ocean and m_map* are used.

Vectorized General Bathymetric Chart of the Ocean (GEBCO) data from the GEBCO Digital Atlas are used to plot the isobaths (IOC, IHO and BODC, 2003). There are sources of inaccuracy in the GEBCO data of this region, as there has been little surveying activity. This inaccuracy is especially related to the shelf-break.

Chapter 3

Results

3.1 ADCP Current Measurements

3.1.1 Horizontal Distribution

Figure 3.1 shows the horizontal distribution of currents at 44 meters depth measured by the ADCP. At the south-western corner of Madagascar, south in the Mozambique Channel (Figure 3.1c), the currents are north-easterly directed west of ∼43°E. Closest to the south-western coast, the currents are southerly directed, aligned with the coast. When the southward directed coastal current reaches the shallow areas south of Madagascar, it tightens up outside the 1000 meters isobath further east. The boundary between the south-eastward directed coastal current and the south-westward directed current to the south, seems to be forced towards the coast. In spite of some irregularities, the current follows the 1000 meters isobath from west to east.

At the south-eastern corner of Madagascar, at *Tôlanaro*, 25°15'S (Figure 3.1c), the north-eastward directed current from south, meets the stronger, southwards directed coastal current aligned with the eastern coast of Madagascar. The north-eastward directed current is squeezed onto shallower areas by the southward directed current, resulting in irregularities at the western side of the boundary. South of *Tôlanaro*, the southward directed current is following outside the 1000 meters isobath, leaving the coast.

South of Madagascar and south of the 1000 meters isobath, the currents are no

(a) *North-east*
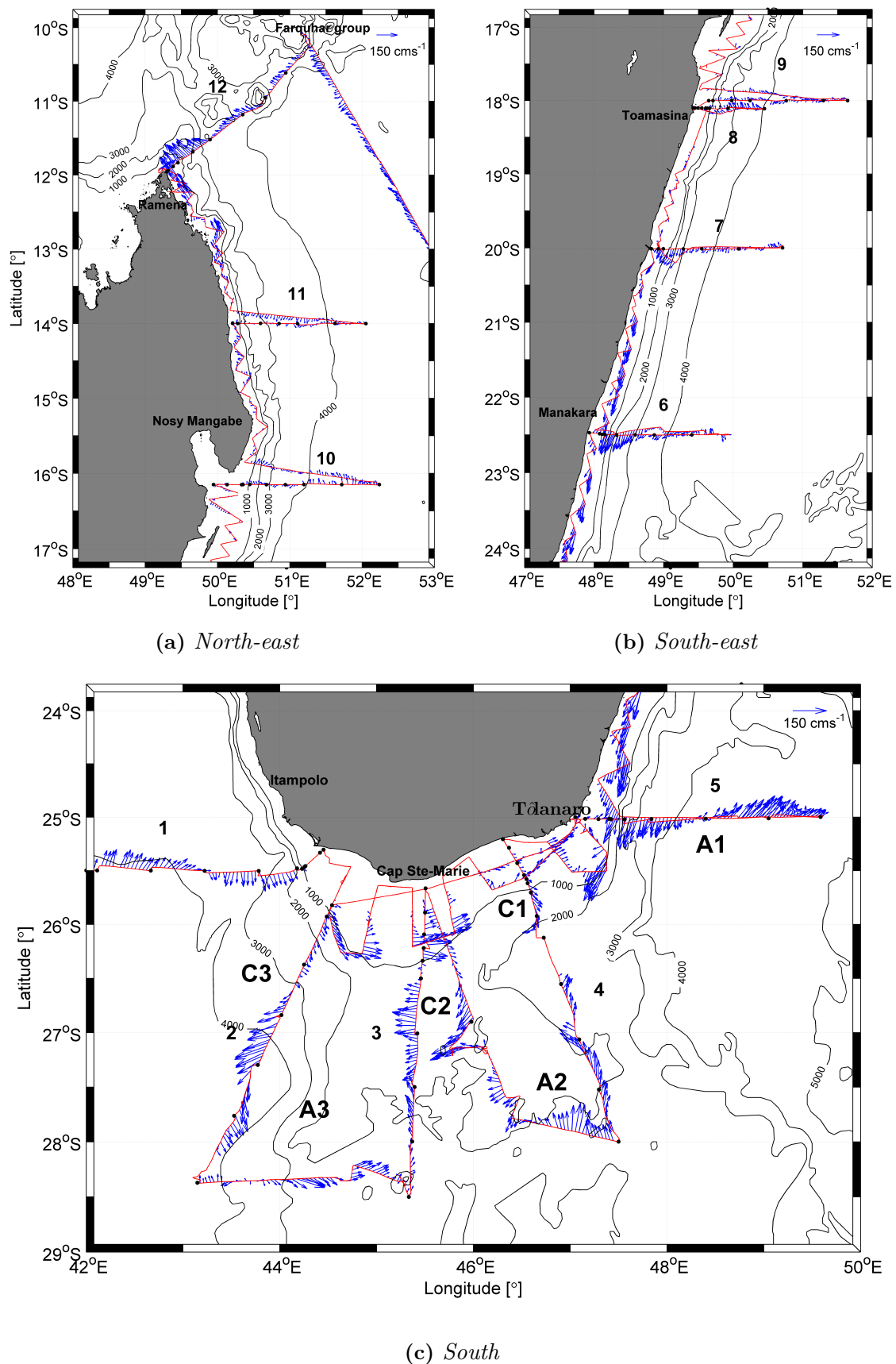
(b) *South-east*

(c) *South*

Figure 3.1: *ADCP: Currents at 44 meters depth for the (a) north-eastern, (b) south-eastern and (c) southern coast. Velocity scale indicated in upper right corner. Black dots indicate hydrographical stations and bold fonts indicate transect numbers. 1 in 4 measurements are plotted.*

longer aligned with the coast. Figure 3.1c indicates three large anticyclonic eddies, labelled A1, A2 and A3, and three smaller cyclonic eddies, labelled C1, C2 and C3.

From transect 5 (25°15'S) to transect 7 (20°S) (Figure 3.1c and 3.1b) the coastal current forms a southwards directed jet with maximum velocity of 150 cms^{-1}, 50 kilometers off the coast in transect 5. In this transect, the boundary between the south-westerly directed coastal current and the north-easterly directed current to the east, is located 140 kilometers off shore. The strength of the jet and the distance from the coast to the center of the jet is decreasing northwards, while the width of the coastal current is increasing to 150 kilometers in transect 7. Northward from transect 5 the boundary between the oppositely directed currents becomes gradually more diffuse.

Between transects 7 and transect 8 (18°S) (Figure 3.1b) the currents are weak at the narrow shelf, and it is difficult to see any clear pattern. When reaching transect 8, the coastal current has changed direction. It is now in general northwards directed and aligned with the coast. The northward directed contribution of the current is varying in width along the northern coast. It is relatively wide in transect 8 and 9 (18°S), narrower in transect 10 (Figure 3.1a) and very narrow in transect 11, where the current is northerly directed only in the very innermost part of the transect. North of transect 11, the northward directed current is widening again, and it is directed north-westwards along the entire transect from the northern tip of Madagascar to the Farquhar group, 51°15'E and 10°15'S.

In transects 8 and 9, the southward directed current is located outside the 4000 meters isobath. In transect 10, the current is northward directed, except between the 3000 and 4000 meters isobaths, where it is southward directed. Further north, in transect 11, the current is southward directed all the way from the 2000 meters isobath to the 4000 meters isobath, with merely a few minor irregularities. Inside the 2000 meters isobath, the northward directed current is weak and narrow. The strength of the northward directed coastal current increases as it approaches the northern tip of Madagascar. The current passes the northern tip as a jet with maximum velocity of 160 cms^{-1} close to the coast. This jet is directed north-westwards and is approximately 100 kilometers wide.

South-east of the Farhquhar group (10°15'S, 51°15'E) the currents are directed north-westwards.

Exceptions from the large scale pattern
are found south of the bay of Nosy
Mangabe (16°15'S - 16°45'S) (Figure
3.1a). Here the currents are southerly
directed close to the coast, even though
the general pattern at this area indicates
northward directed currents.

At the northern tip of Madagas-
car (Figure 3.2), the currents are
north-easterly directed at the south-
western side of the northern tip, per-
pendicular to the north-westwards di-
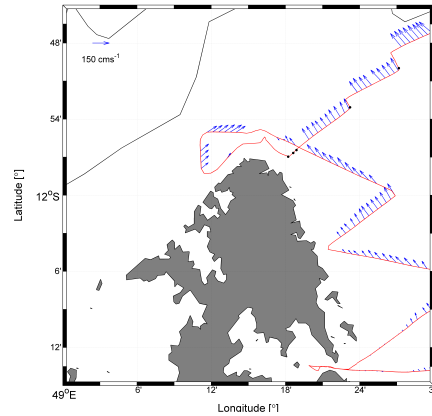rected currents at the north-eastern
side.

Figure 3.2: *ADCP: Close-up of currents
at the northern tip of Madagascar at 44 me-
ters depth. Velocity scale indicated in upper
left corner. Black dots indicate hydrographi-
cal stations.*
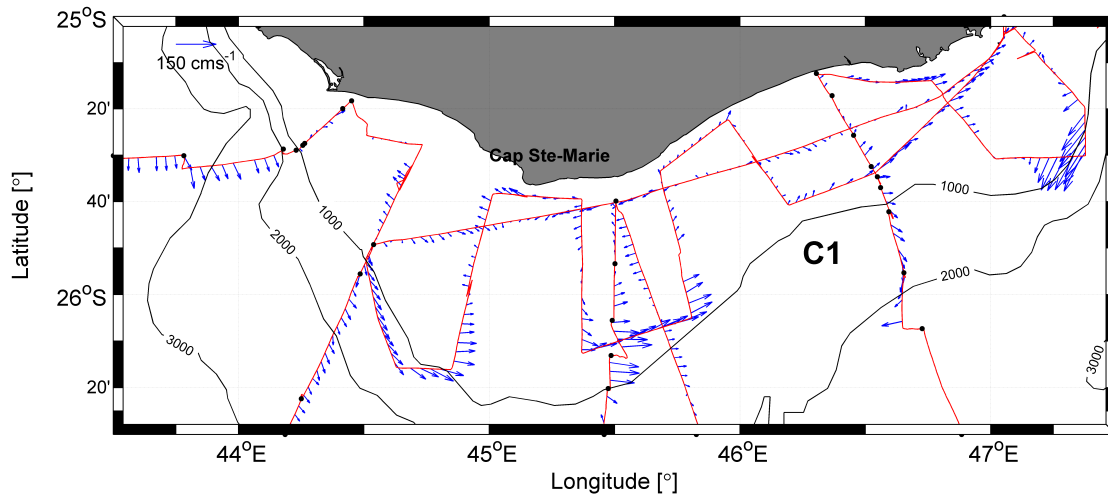
Figure 3.3: *ADCP: Currents at 20 meters depth at the southern shelf of Madagas-
car. Velocity scale indicated in upper left corner. Black dots indicate hydrographical
stations. 1 in 4 measurements are plotted.*

Figure 3.3 shows a close-up of the horizontal current distribution at 20 meters depth
in the shallowest part of the southern shelf of Madagascar. Closest to the coast, the
currents are generally directed westwards, opposite of the currents following the 1000
meters isobath (Figure 3.1c). At 45°45'E (Figure 3.3) the currents are oppositely
directed as the vessel arrives and leaves the coast carrying out the transect.

3.1.2 Vertical Structures

Figure 3.4: *ADCP: Stickplot of transect 3 and map with transect 3 indicated. Note that blanking distances between the lines in the stickplot are not to scale with depths.*

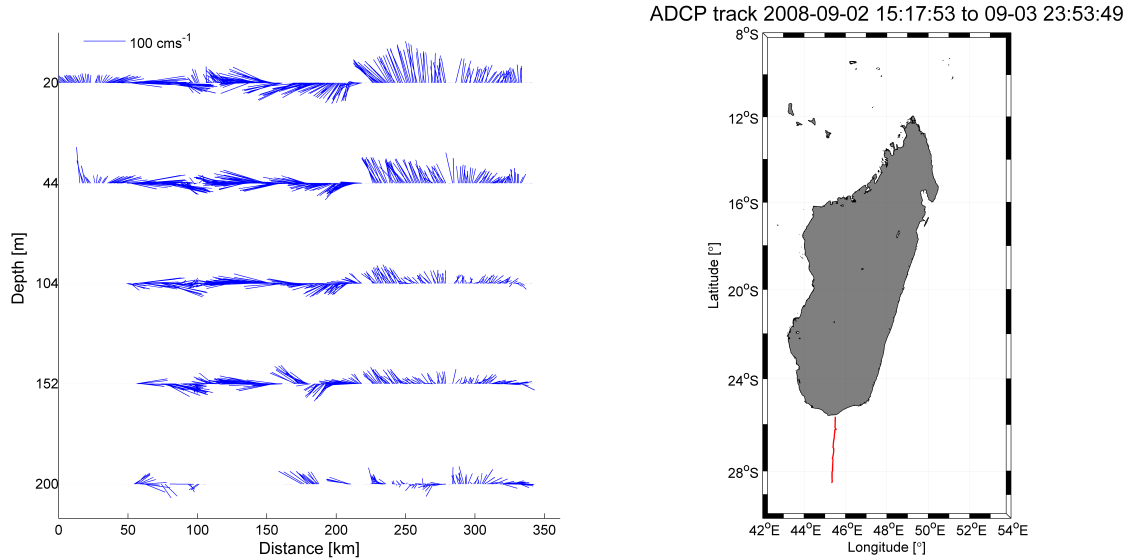Figure 3.4 shows mainly barotropic currents, were the signals seen in the surface layer at the southern coast of Madagascar can be identified all the way down to 200 meters depth. This transect cuts right through the eddy-like feature, A3, pinpointed in Section 3.1.1. Changes in direction of the currents with depth are minor, but the magnitude of the current velocities are generally decreasing with depth. The maximum of the currents in transect 3 was almost 130 cms^{-1}, at 20 meters depth, about 70 kilometers out in the transect.

At the south-eastern corner of Madagascar (Figure 3.5), the stickplot reveals strong barotropic currents, aligned with the coast. Pattern seen in the surface layer are consistent down to 200 meters depth. The magnitudes of the currents are however decreasing with increasing depth. Figure 3.5 shows maximum current velocity ∼150 cms^{-1}, 25 - 50 kilometers out in the transect. Northwards along the coast, the currents become more irregular throughout the transects, and the strength of the jet close to the coast is in general decreasing northwards, both in the surface and in the deeper waters.

Further north, in transect 7 (not shown) the currents are less barotropic. The strong currents found close to the coast almost disappears at 152 meters depth. The boundary between the two oppositely directed currents of transect 7 is not as
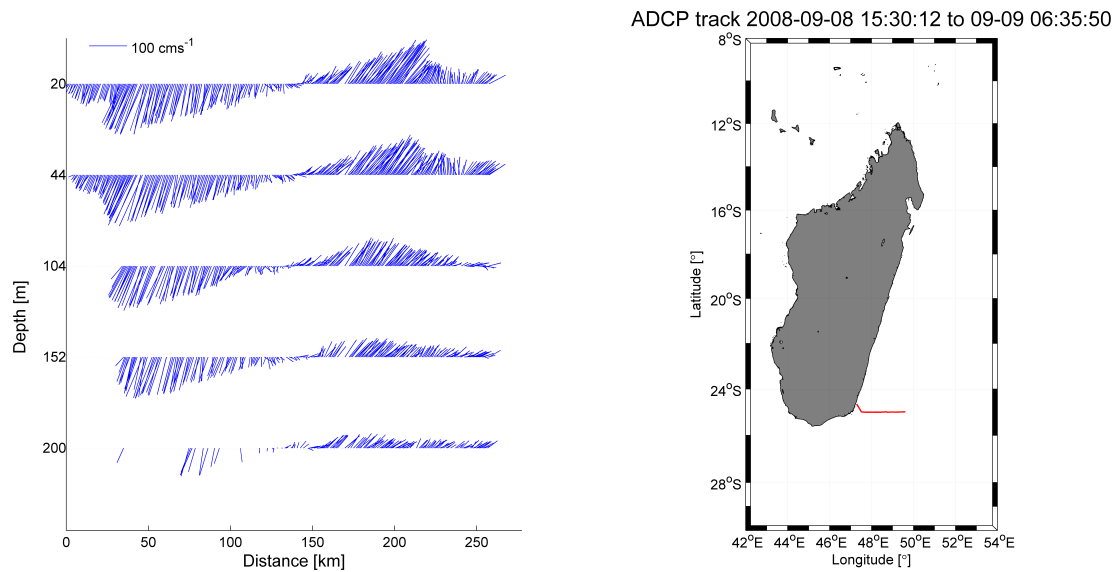
Figure 3.5: *ADCP: Stickplot of transect 5 and map with transect 5 indicated. Note that blanking distances between the lines in the stickplot are not to scale with depths.*

sharp as in transect 5.

At the narrow shelf, between transects 5 and 7 (Figure 3.1b and 3.1c) there seem to be few irregularities down to 104 meters depth, but from 150 meters depth, the irregularities are increasing (not shown). Some of the currents at these depths are directed straight towards the coast. At the very innermost part of transect 7 (not shown), the currents are weaker. At 104 meters depth, some of the currents are even directed northward. In the area closest to the coast, the currents are more easterly directed at 104 meters depth than at 44 meters depth. The maximum magnitude of the velocities in transect 7 was almost 100 cms^{-1}. The velocity of the currents seems to be higher in areas where the currents are regular.

Between transect 7 and 8 the coastal boundary current changes direction, and from transect 8 it is northerly directed (Figure 3.1b and 3.1a). The vertical distribution of the northward directed coastal current in transect 10 (Figure 3.6), shows that the current is mainly northward directed in the inner 90 kilometers of the transect. From ∼90 - 145 kilometers off the coast, the currents are heading southwards before they again are heading northward farther off shore. The maximum measured current velocity in this transect is almost 60 cms^{-1} at 200 meters depth. The strength of the current is increasing as it becomes more regular and northward directed outside about 150 kilometers off coast. It should be noticed that transect 10 is located right

south of Nosy Mangabe, with its tongue of land reaching far out into the transect.

In deeper waters between transect 9 and transect 10 (Figure 3.1b), the currents are again slightly more irregular (not shown). The boundary between the northerly directed coastal current, and the southerly directed current outside, seems to move off coast with increasing depth (Figure 3.6).

In transect 12, 10 - 12°S (not shown), more than 160 kilometers off shore, the southward component of the currents are increasing with increasing depth.
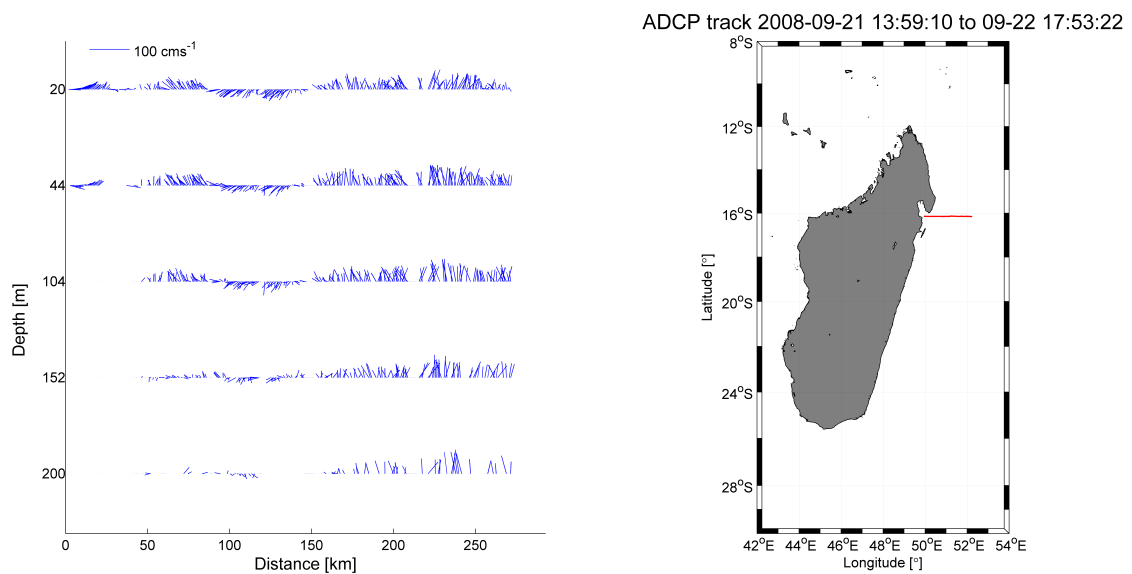

Figure 3.6: *ADCP: Stickplot of transect 10 and map with transect 10 indicated. Note that blanking distances between the lines in the stickplot are not to scale with depths.*

3.2   Measured and Modeled Wind Distribution

Figure 3.7 shows the measured 10 minutes averaged wind from the WIMDA mete-
orological station at the vessel during the cruise, together with the mean monthly
reanalyzed MERRA wind of September 2008. As a consequence of the different
averaging intervals, the observed wind is stronger than the MERRA wind. Even
though the strength of the winds are different, the direction of the winds generally
coincide well. The MERRA wind (Figure 3.7) also coincides well with the current
(ADCP) measurements at 44 meters depth at the eastern coast (Figure 3.1).

The mean monthly reanalyzed MERRA wind of September 2008 (Figure 3.7) shows
zonal wind of $\sim$5 ms^{-1} from the Indian Ocean reaching the eastern coast of Mada-
gascar at $\sim$19°S. The wind splits into a northward and southward directed flow,
blowing around the island. The meridional component increases northwards and
southwards along the coast.

The MERRA wind field in August 2008 (not shown), representing the first few days
of the cruise, shows generally more zonal wind. At the southern coast, the wind was
more aligned with the coast in August than in September, 2008. The zonal wind of
August reaches the coast farther south ($\sim$21°S) than the more meridional wind of
September.

As the hitting point moves northwards from August to September 2008, and the
meridional component increases with distance from the hitting point, the merid-
ional component of the southern and south-eastern coast is increasing, while the
meridional component at the northern coast is decreasing. In October (not shown),
the wind field is very much the same as in August for the northern part, while
the wind at the southern and south-eastern coast is much stronger with a stronger
meridional component. In October, the wind is no longer aligned with the southern
coast.
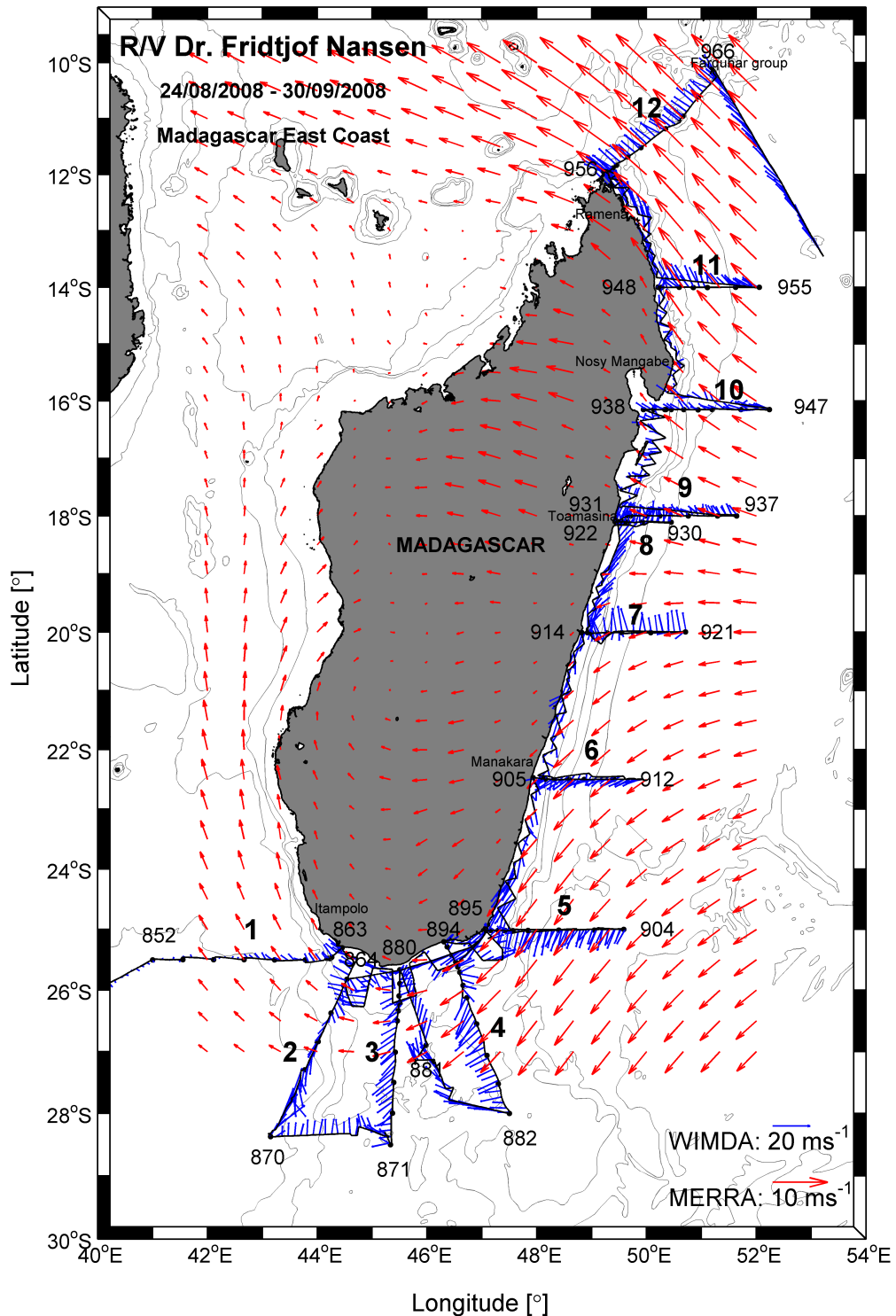
Figure 3.7: *Reanalyzis and observations: MERRA monthly averaged windfield for September 2008 (red arrows) together with measured wind from the WIMDA meteorological station at the vessel (blue arrows). The 1000, 2000, 3000, 4000 and 5000 meters isobaths, vessel course track and hydrographical (CTD) stations are indicated. Hydrographical transects are labeled with bold fonts. Note that observed wind and MERRA wind are not to scale. Velocity scales are indicated in lower right corner.*

3.3   Definition of Water Masses

Table 3.1: *Abbreviations of the Water Masses*

Abbreviation	Water Mass
TSW	Tropical Surface Water
STSW	Sub-Tropical Surface Water
ITW	Indonesian Throughflow Water
SICW	South Indian Central Water
AAIW	Antarctic Intermediate Water
RSIW	Red Sea Intermediate Water
IIW	Indonesian Intermediate Water
NIDW	North Indian Deep Water
CDW	Circumpolar Deep Water
NADW	North Atlantic Deep Water

The water masses at the coast of Madagascar are divided into three groups dependent of their depths/densities; surface water, intermediate water and deep water.

The surface water of the south-western Indian Ocean consists of three different water masses. The upper one is the relatively high oxygen, fresh and warm TSW originating from the Tropics. The low content of salinity (S< 35.5) is a result of excess precipitation over evaporation (Read & Pollard, 1993), and influence of low-salinity ITW carried westward by the SEC (Donohue & Toole, 2003). The TSW is also relatively warm with temperatures exceeding 23°C (Read & Pollard, 1993). The underlying STSW, originating from the Sub Tropical Indian Ocean, consists of low oxygen water with salinities exceeding 35.5 (Gründlingh *et al.*, 1991). The high salinity is a result of excess evaporation over precipitation (Donohue & Toole, 2003). According to Donohue & Toole (2003), the STSW carries a high amount of nutrients due to in-situ bacterial break down of organic matter. Below the STSW, around the thermocline depth ($\sim$400 - 800 meters), the SICW is located with its characteristic oxygen maximum. This water mass could also be identified in the TS diagram by its relatively linear relationship between potential temperature and salinity between 9°C and 14°C (Gründlingh *et al.*, 1991).

The intermediate water is defined as water with densities between $\sigma_\theta = 26.9$ and $\sigma_\theta = 27.7$ (Donohue & Toole, 2003), consisting of AAIW, RSIW and IIW. According to

Donohue & Toole (2003), the strongest signal of AAIW is low salinity and relatively high oxygen, with densities between $\sigma_\theta = 27.2$ and $\sigma_\theta = 27.4$ at 800 - 1200 meters depth. The RSIW is recognized by its salinity maximum and minimum oxygen content compared with other Indian Ocean intermediate water masses (Roman & Lutjeharms, 2007). The RSIW is originating from the Red Sea and the Persian Gulf (You *et al.*, 2003). The IIW is relatively fresh, high silicate water advected towards the eastern coast of Madagascar with the SEC (Talley & Sprintall, 2005). As there exists no measurements of silicate, which makes this water mass difficult to recognize, this water mass will not be taken into further consideration, but it is expected to be associated with the EMC, freshening the RSIW.

The deep water consists of NIDW, CDW and the NADW, and is located near 2500 meters depth. The originally relatively fresh and oxygen rich CDW of this region is influenced by the highly saline NADW, to be identified by higher both salinity and oxygen than the NADW along the southern and eastern coast of Madagascar (Park *et al.*, 1993; Dickson & Brown, 1994). The CTD profiles, and hence the description of the water masses, are limited to 3000 meters depth (Krakstad *et al.*, 2008). The description of the deep water masses will be carried out in Section 4.1.6.

3.4 Horizontal Distribution of SSS, SST and SSF

The horizontal distribution of SSS (Figure 3.8) reveals that the surface salinity in general decreases northwards. At the southern and south-eastern coasts, the surface water is relatively saline (S~35.6) closest to the coast, while it is slightly fresher (S~35.5) farther away from the coast. In addition to a tongue of relatively fresh (S~35.1) water, following the 2000 meters isobath south-westwards from the south-eastern corner of the island, another patch or relatively fresh (S~35.1) water is observed with its center at hydrographical station 868. This patch could also be related to the anticyclonic eddy, A3 (Figure 3.1c). At the south-eastern coast, the patterns are relatively homogeneous with S~35. Relatively fresh water (S~34.8) is observed in the inner parts of transect 6, transect 7 and north of transect 9, related to the outlet of the Mananara, Mangoro and Maningory rivers respectively. Just south of Nosy Mangabe (transect 10) there is a large patch of very fresh water (S~34.2). The surface water of the northern coast is generally fresher close to the coast than offshore.

The horizontal distribution of SST (Figure 3.9) reveals that the temperature of the surface water is in general increasing northwards. Closest to the southern and south-eastern coast the temperature is low ($\sim$20.5°C), and it is in general increasing with increasing distance from the coast. A south-westwards directed tongue of warmer water ($\sim$23°C) is observed from just outside the south-eastern corner of the island, coinciding with the tongue of fresh water observed in the horizontal distribution of SSS (Figure 3.8). It could also be related to the southward directed branch of the EMC leaving the coast at the south-eastern corner of the island (Figure 3.1c). Outside this tongue, the water is colder ($\sim$20 - 21°C). In the south-eastern region, the SST is monotonically increasing northwards, only interrupted by a patch of warmer water in the center of transect 7, and colder water closest to the coast in the southernmost part of the region. In the southern part of the north-eastern region, the temperatures are highest closest to the coast, while the core of maximum SST is moved off coast northwards.

The horizontal distribution of SSF (Figure 3.10) reveals that the general content of fluorescence in the surface layer is higher in the southern region than in the north-eastern region. According to Pripp (2011) the diurnal variations in the fluorescence were small compared to the variations related to position. This conclusion was drawn based on data from the southern and western coast of Madagascar in 2009. The pattern is expected to be similar at the eastern coast, and diurnal variations in fluorescence will not be taken into further consideration in this thesis. The content of SSF at the eastern coast of Madagascar is generally very low, but some patches of relatively high SSF are observed. The highest amount of fluorescence (1.28 μgl^{-1}) was measured at the south-eastern corner of the island, and relatively high values were obtained at the narrow shelf all the way north to 23°30' S. In addition, the patterns seen in salinity and temperature with a south-westwards directed tongue, could also be recognized in the SSF. Scattered patches of relatively high fluorescence are observed in the southern region. In the north-eastern region, the SSF is low everywhere, only with exception of some slightly higher values in the outer part of transect 12, close to the Farquhar group.

Figure 3.8: *Horizontal distribution of SSS at 5 meters depth. Vessel course track, 1000, 2000, 3000, 4000 and 5000 meters isobaths, hydrographical stations and numbers of hydrographical transects are indicated. Note missing values between transect 10 and 11. The white patch closest to the coast north of transect 7 is due to rinsing of the data.*

Figure 3.9: *Horizontal distribution of SST at 5 meters depth. Vessel course track, 1000, 2000, 3000, 4000 and 5000 meters isobaths, hydrographical stations and numbers of hydrographical transects are indicated.*
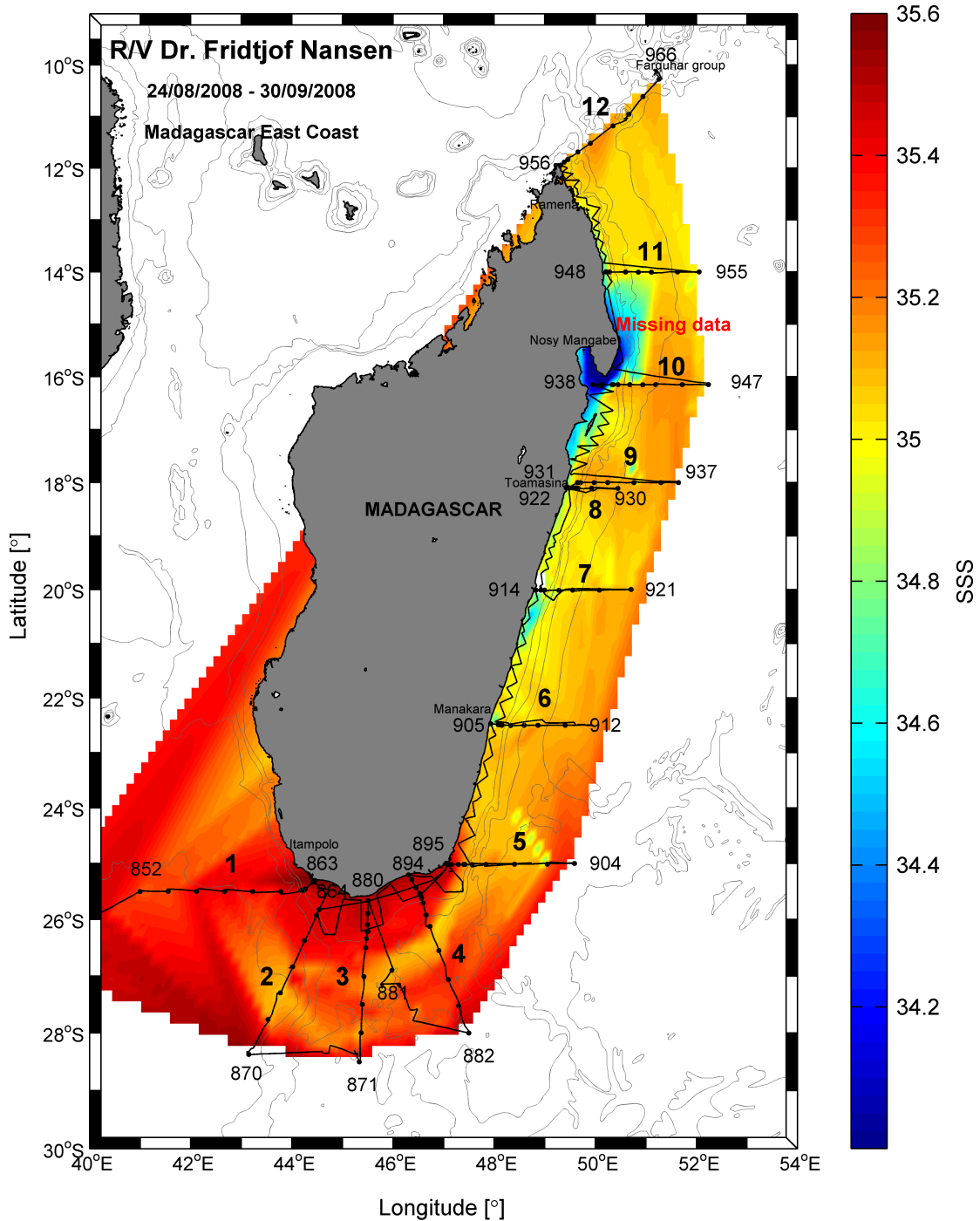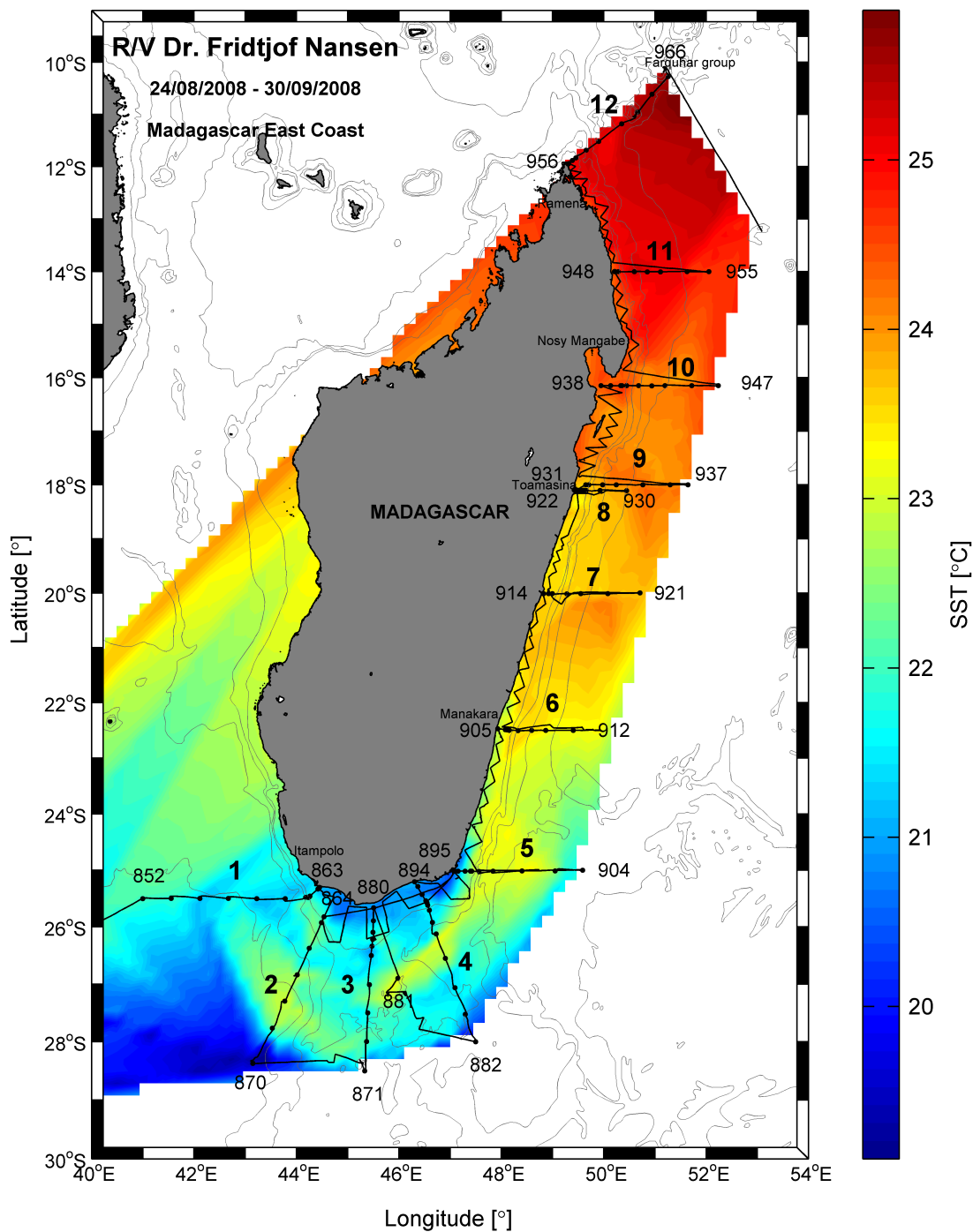
Figure 3.10: *Horizontal distribution of SSF at 5 meters depth. Vessel course track, 1000, 2000, 3000, 4000 and 5000 meters isobaths, hydrographical stations and numbers of hydrographical transects are indicated. Note missing values between transect 10 and 11.*
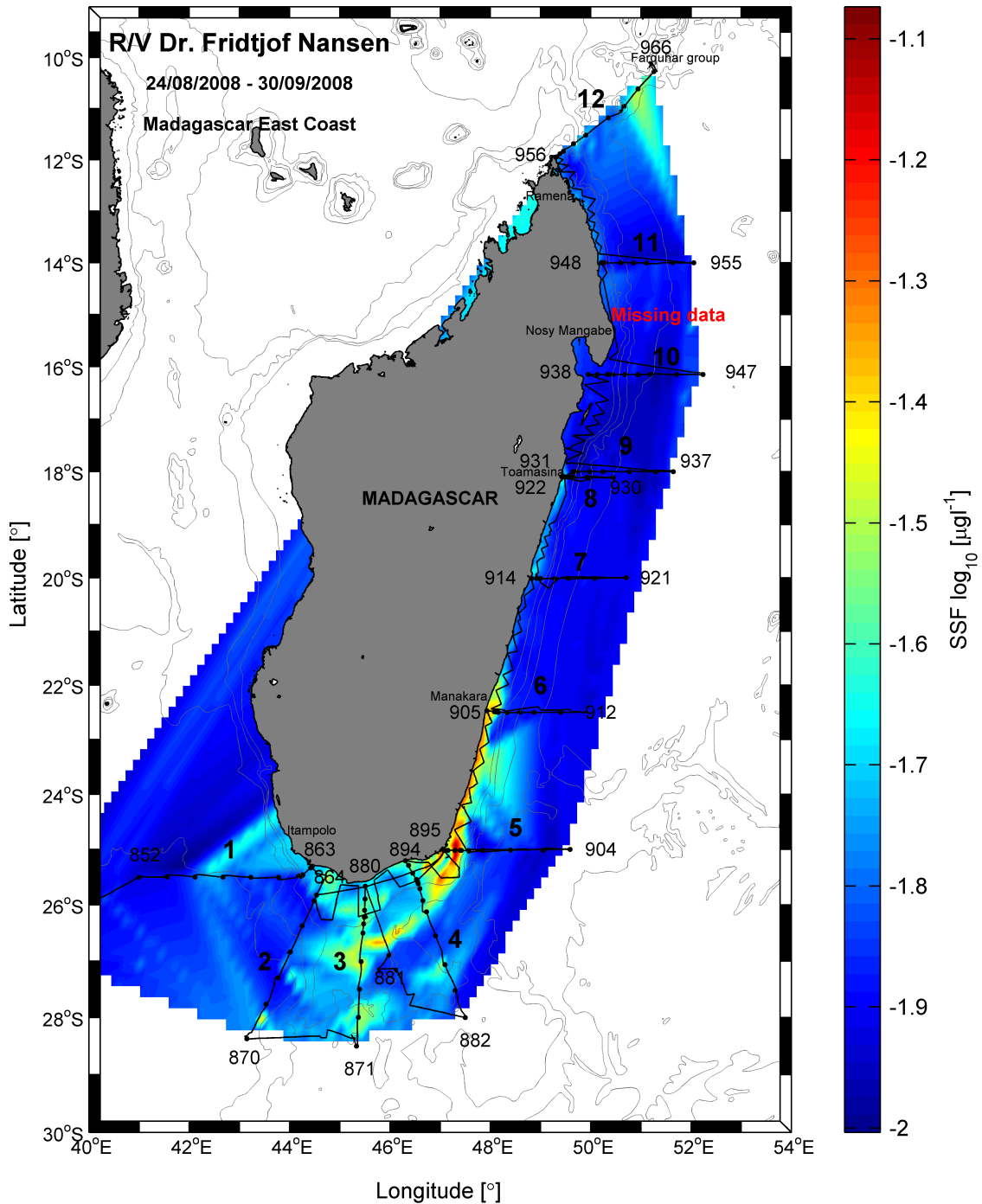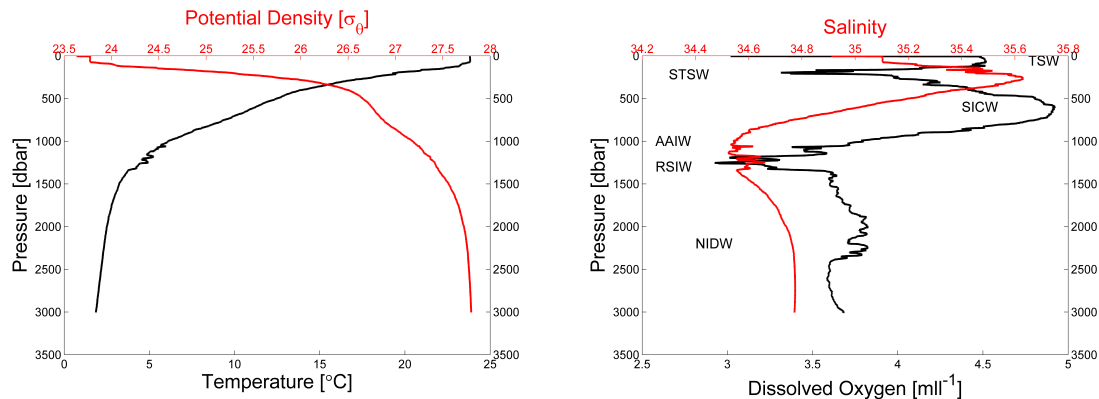
3.5   Description of Water Masses

The water masses are identified mainly on the basis of their salinity and oxygen content. Hence, Temperature-Salinity (TS) and Temperature-Oxygen (TO_2) diagrams are used for the identification.

(a) *Potential density and temperature plotted against depth.*

(b) *Salinity and dissolved oxygen plotted against depth.*

Figure 3.11: *Vertical profiles of (a) Potential density and temperature and (b) Salinity and dissolved oxygen for hydrographical station 902.*

Figure 3.11 shows vertical profiles of temperature, potential density, dissolved oxygen and salinity for hydrographical station 902, located outside the shelf-break at the south-eastern corner of Madagascar (Figure 2.1). The potential density follows the pattern of the temperature very closely (Figure 3.11a). As the potential density is determined by the temperature, and the temperature decreases with increasing depth in the entire research area, these two parameters will not be discussed further in the description of the deep water masses.

The TS diagram representing the north-eastern coast (Figure 3.12c), indicates relatively fresh and warm surface water, with salinities below 33 and temperatures between 23°C and 25°C. Figure 3.12 indicates that the span in salinity of the STSW is larger at the north-eastern coast than at the southern and south-eastern coasts. This indicates that the water masses of the north-eastern coast are less homogeneous, and that the thickness of the TSW varies more in this region, than in the two southern regions. It is also seen that the layer of TSW thickens northwards. The layer of SICW, showing a relatively linear relationship between the potential temperature and salinity, is thinner and less defined for the north-eastern region

Figure 3.12: *TS diagram of the (a) southern, (b) south-eastern, (c) north-eastern region and (d) the entire research area. Geographical boundaries are given in Table 2.1.*

(Figure 3.12c), than for the two southern regions (Figure 3.12a and 3.12b), indicating a thinner and less evident layer of SICW at the north-eastern coast. The temperature of the surface water is increasing northwards, lifting the water masses in the TS diagram.

Similar to the TS diagrams (Figure 3.12), the spread in the measurements of oxygen (Figure 3.13) is largest at the north-eastern coast (Figure 3.13c). The TO_2 diagram also reveals that the minimum oxygen, related to the STSW, is deepening northwards. From the southern coast (Figure 3.13a) to the north-eastern coast (Figure 3.13c) the oxygen minimum is depressed in the TO_2 diagram from $\sim20°C$ to $\sim15°C$.
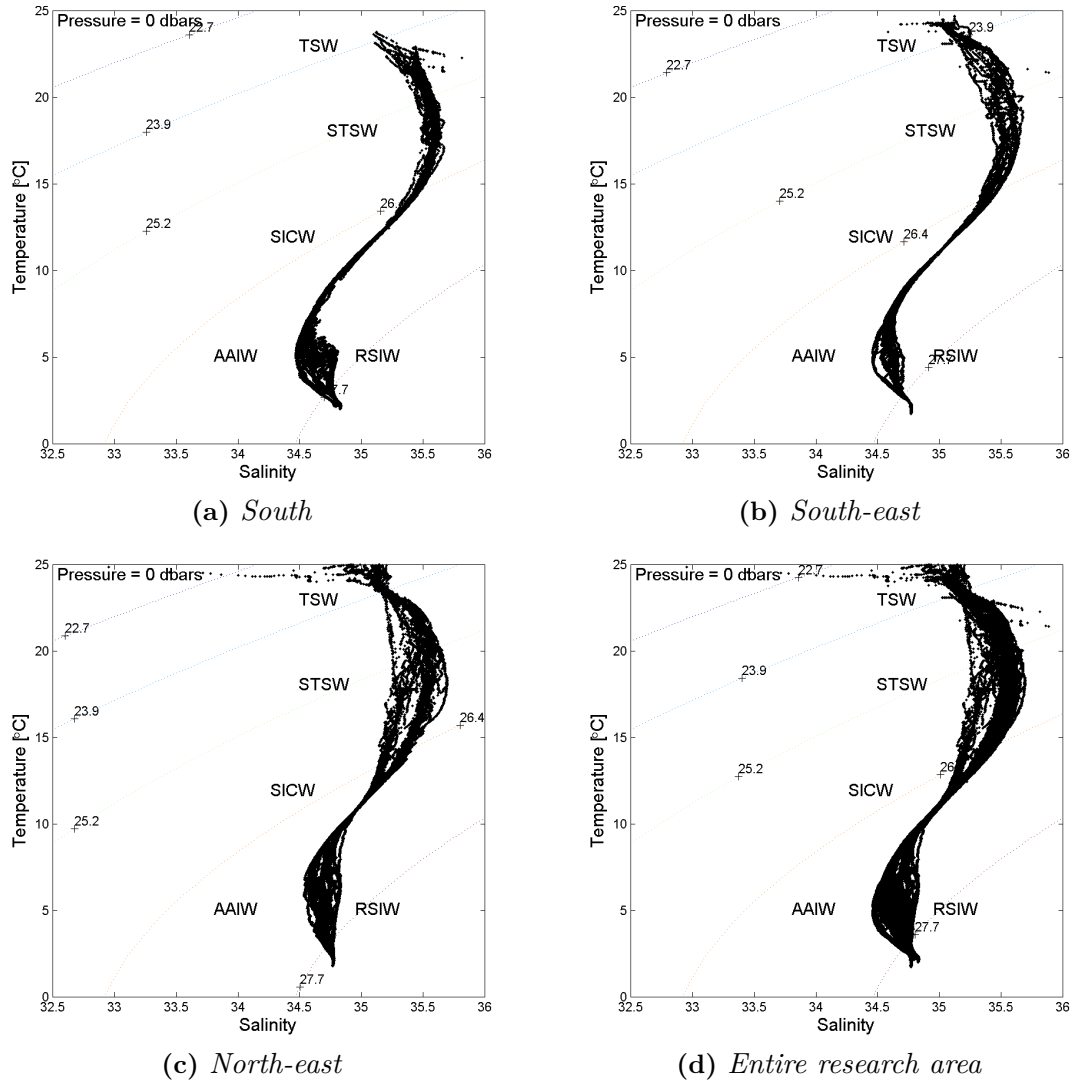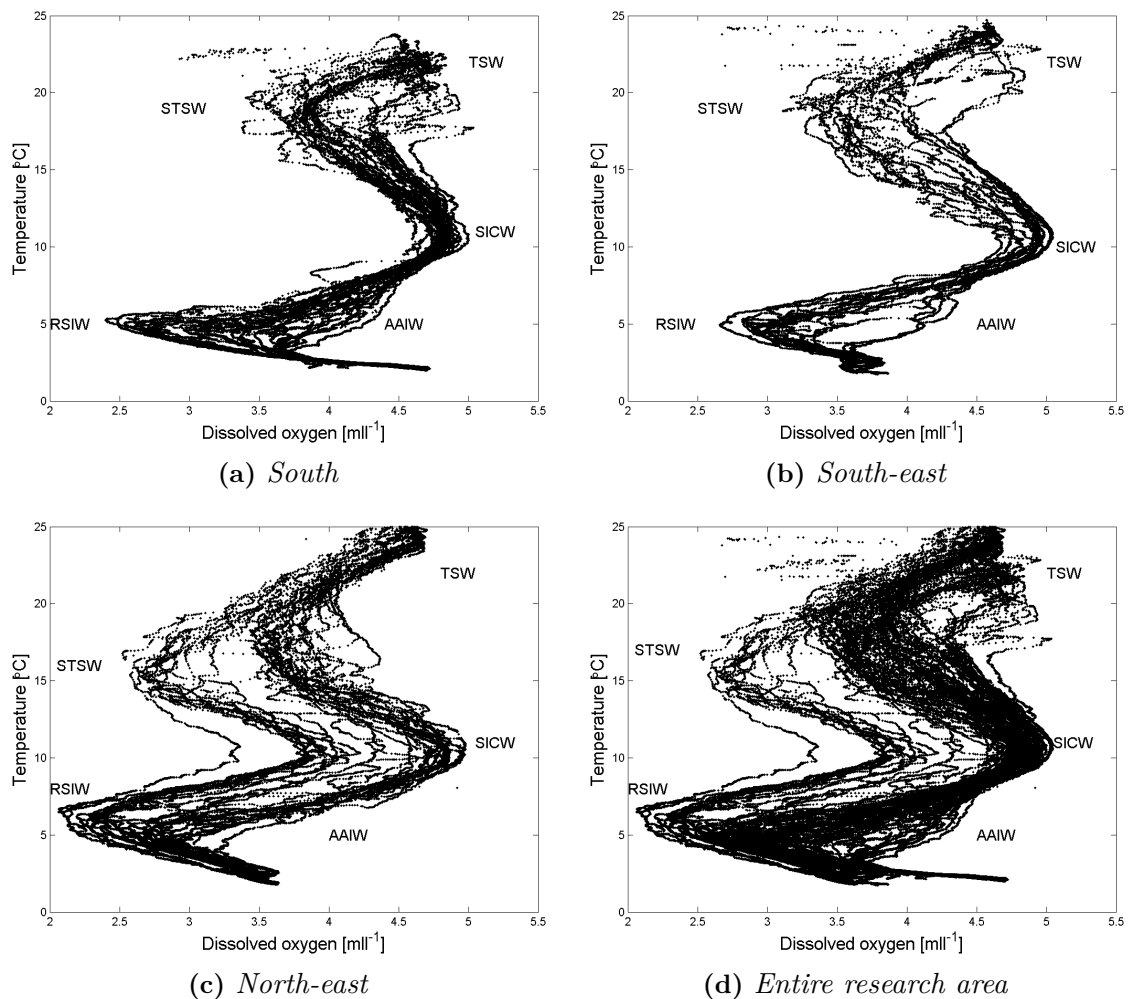
Figure 3.13: *TO$_2$ diagram of the (a) southern, (b) south-eastern, (c) north-eastern region and (d) the entire research area. Geographical boundaries are given in Table 2.1.*

The intermediate waters at the southern and south-eastern coasts are a mix of both AAIW and RSIW. By plotting the salinity and oxygen against pressure, station by station for each of the transects at the southern coast (not shown), it is seen that the salinity of the intermediate waters decreases while the content of oxygen increases with increasing distance from the coast. This indicates that the content of AAIW in the intermediate water increases southwards, while the content of the RSIW increases northwards. The RSIW seems to be located beneath the AAIW. The level of minimum values are sinking in the water column with increasing distance from the coast. Along the south-eastern coast, the intermediate water is more saline and contains less oxygen closest to the coast than farther off coast, indicating a higher content of RSIW closest to the coast, and a higher content of AAIW away from the

coast.

As the temperature gradients are small at large depths, it is hard to distinguish between the deep waters by looking at the TS and TO_2 diagrams. The deep waters will be presented and discussed in Section 4.1.6.

3.5.1 Hydrographical Transects

Hydrographical Structures in the Deep Waters (<3000 meters depth)

(a) *Salinity*

(b) *Dissolved Oxygen [mll^{-1}]*

Figure 3.14: *Hydrographical transect 3. (a) Salinity and (b) Dissolved oxygen down to 3000 meters depth. Ticks in the surface indicate CTD stations.*

Figure 3.14 shows the patterns in salinity and oxygen of hydrographical transect 3 (Figure 2.1), representing the southern coast. Beneath the saline and low oxygen STSW, the SICW is located at ∼300 - 700 meters depth with its oxygen maximum and salinity decreasing with increasing depth (Figure 3.14). In the intermediate water (700 - 1500 meters depth), it is difficult to separate between the relatively oxygen rich and fresh AAIW and the relatively saline and oxygen depleted RSIW. This is because the intermediate water of this region is in general both relatively fresh and oxygen depleted. This indicates that these two intermediate water masses are relatively well mixed. By plotting temperature and oxygen against depth for each of the stations in the transect (not shown), it can be seen that there are stronger signals of RSIW, with lower content of oxygen and higher salinity closest to the coast, and stronger signals of AAIW with higher content of oxygen and lower salinity in the outer part of the transect. It can also be seen that the minimum oxygen, related to the AAIW, was located a little higher in the water column (700

- 1200 meters depth) than the minimum oxygen, related to the RSIW (1200 - 1500 meters depth).

In transect 1 (not shown), the AAIW and the RSIW was less mixed, but eastwards, the layer of AAIW is depressed from its original ∼800 - 1000 meters depth while the RSIW is lifted from its original from ∼1000 - 1300 meters depth. This causes difficulties when it comes to separating between these water masses. The most oxygen depleted RSIW was found in transect 1.

(a) *Salinity*   **(b)** *Dissolved Oxygen [mll⁻¹]*
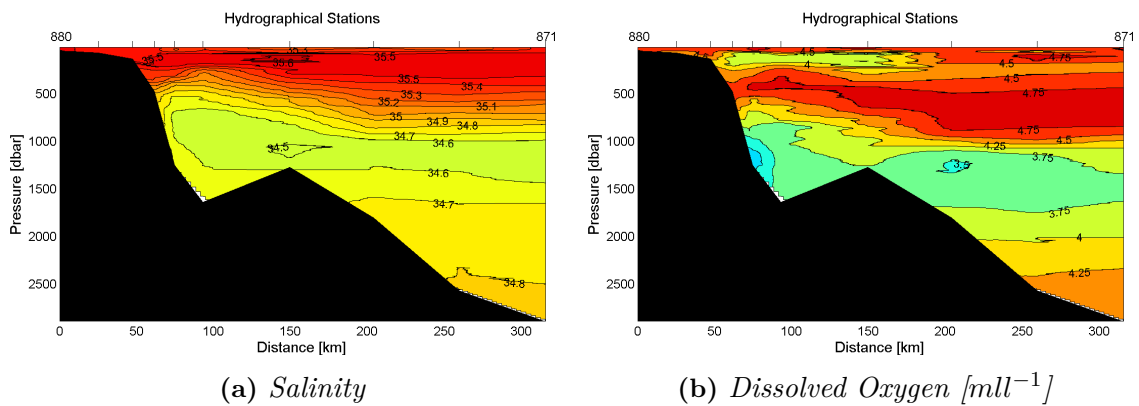
Figure 3.15: *Hydrographical transect 5. (a) Salinity and (b) Dissolved oxygen down to 3000 meters depth. Ticks in the surface indicate CTD stations.*

In transect 5 (Figure 3.15), the southernmost transect at the south-eastern coast (Figure 2.1), the SICW is located at ∼300 - 800 meters depth. As seen in the TO_2 and TS diagram (Figure 3.12 and 3.13), the layer of SICW becomes thinner and less evident northwards. The content of oxygen in the SICW is decreasing all the way from transect 6 (not shown) and northwards, indicating that the SICW becomes less characteristic and dominant.

The underlying RSIW (∼1000 meters depth) on the other hand, becomes thicker and more evident with lower values of oxygen northwards in the south-eastern region. In transect 5 (Figure 3.15b), the minimum content of oxygen is ∼3 mll^{-1} at ∼1000 meters depth, while in transect 7, the northernmost transect of the south-eastern region, the minimum content is 2.75 mll^{-1}. This minimum value is located further offshore than for the previous transects indicating that the RSIW is located farthest away from the coast, while the AAIW is located closest to the coast. It is easier to separate between the intermediate water masses (800 - 1500 meters depth) at the south-eastern coast than at the southern coast. High salinity and low oxygen RSIW is located closest to the coast, while higher oxygen and lower salinity AAIW is found

in the outer part of the transects.

The intermediate water becomes more saline, and the layer of relatively fresh water at ∼1000 meters depth becomes less evident northwards along the coast. It is also seen that the content of oxygen at ∼1000 meters depth decreases northwards throughout this region. This indicates that the AAIW is gradually being replaced by the RSIW northwards along the south-eastern coast (Figure 3.15).

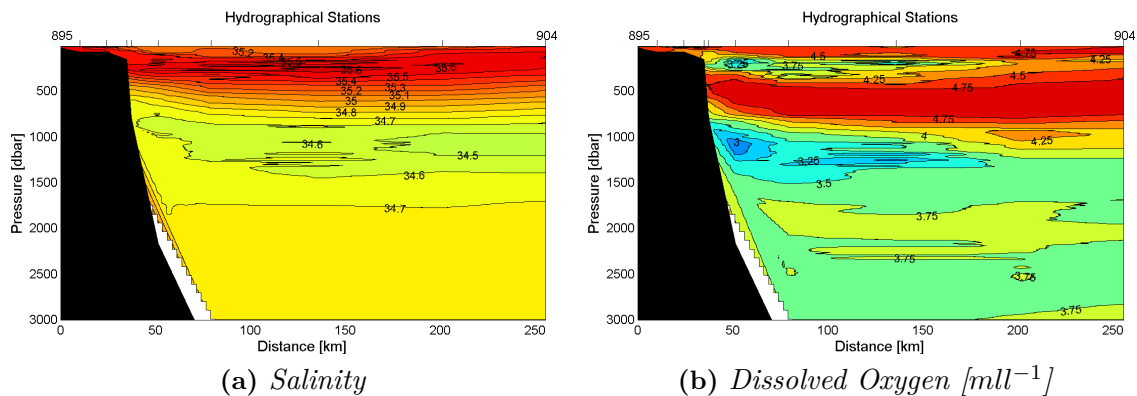**(a)** *Salinity*   **(b)** *Dissolved Oxygen [mll^{-1}]*
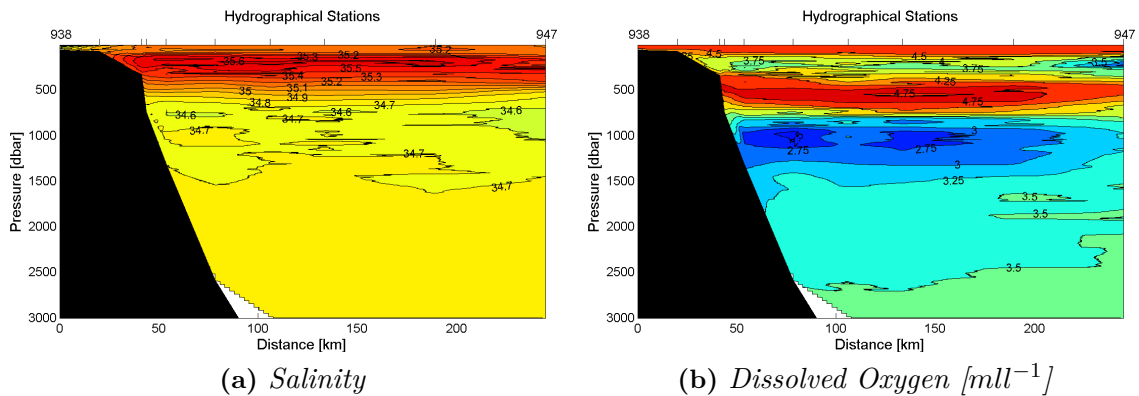
Figure 3.16: *Hydrographical transect 10. (a) Salinity and (b) Dissolved oxygen down to 3000 meters depth. Ticks in the surface indicate CTD stations.*

The same trends as observed at the south-eastern coast is also observed at the north-eastern coast represented by transect 10 (Figure 3.16). The oxygen rich SICW, located at ∼400 - 800 meters depth (Figure 3.16b), continues being less evident northwards, and in transect 12 (not shown) it is almost disappeared. On the other hand, the RSIW at ∼1000 meters depth continues being increasingly more evident northwards along the north-eastern coast. From transect 10 and northwards, the RSIW is located closest to the coast, while the fresher, higher oxygen AAIW is located offshore. North of transect 10, the salinity minimum at ∼1000 meters depth disappears.

In transect 8 (not shown), there are little structure, i.e. horizontal isolines.

Hydrographical Structures in the Upper Layer (<250 meters depth)

For biological purposes, the upper 250 meters of the water column are the most interesting, and will be investigated further in this section.

The salinity and oxygen for the upper 250 meters of hydrographical transect 3 (Figure 3.17a and 3.17b) reveal a ∼70 meters thick surface layer of relatively fresh

(a) *Salinity*

(b) *Dissolved Oxygen [mll^{-1}]*

(c) *Temperature [°C]*

(d) *Fluorescence [µgl^{-1}]*

Figure 3.17: *Hydrographical transect 3. (a) Salinity, (b) Dissolved oxygen, (c) Temperature and (d) Fluorescence for the upper 250 meters. Ticks in the surface indicate CTD stations.*

TSW (S<35.5) with high contents of oxygen ($\sim$4.5mll^{-1}). The dominant water mass of the surface layer of the southern region is the underlying STSW, which is in general located from $\sim$70 meters depth, recognized by both higher salinity (S>35.5) and in general less oxygen than the TSW. As seen in Figure 3.1c the southern coast is influenced by eddies. The eddies seems to rise or depress the boundary between the TSW and the STSW. The only transect in the southern region that seems not to be influenced by eddies is transect 1 (not shown). The eddies can depress the STSW to $\sim$130 meters depth.

The hydrographical transects of salinity and temperature for transect 3 (Figure 3.17a and 3.17c) show two upside-down domes of relatively fresh (S$\sim$35.25) and warm (up to 22.5°C) water in the surface layer, with its cores located at station 874 and 872. Above the shelf-break, another structure is located in the surface, with low salinity (S$\sim$35.3) and high temperature ($\sim$22.5°C).

Both the isohalines and the isothermals of transect 3 (Figure 3.17a and 3.17c) are rising above the shelf, indicating upwelling. At the inner part of the shelf, the water is more saline and colder than outside. This is observed in all the transects of the southern region. From about 70 meters depth and downwards, outside the shelf-break, the isohalines are sinking towards the coast, indicating downwelling. A dome-shape of colder and fresher water from below is observed both in salinity and temperature at ∼200 meters depth, ∼100 kilometers out in transect 3.

It should also be noticed that the highest temperature of the surface layer is related to areas of low salinity, i.e. the patterns of the temperature in the upper 100 meters are following the patterns of the salinity.

The highest amounts of fluorescence in the southern region are generally found on the shelf and at ∼50 - 80 meters depth outside the shelf-break. As seen in Figure 3.17d, the patterns are different in transect 3 where the highest amounts of fluorescence (∼0.76 $\mu g l^{-1}$) are found higher in the water column, 150 kilometers from the coast. The maximum fluorescence of transect 3 seems to be strongly related to areas of low salinity and high temperatures. The content of oxygen seems to be relatively high in areas of maximum fluorescence, and lower in the layer below these areas, in the entire region.

At the south-eastern coast, the EMC is southwards directed and aligned with the coast in the inner part of the transects, while it is northwards directed and aligned with the coast in the outer part of the transects (Figure 3.1b and 3.1c).

Figure 3.18a and 3.18b, showing the salinity and oxygen for the upper 250 meters of transect 5, reveal that the upper layer is dominated by the TSW, reaching down to almost 180 meters depth in the inner part of the transect, and 70 meters depth in the outer part. Beneath the TSW, the STSW is found. The STSW is also found in the inner part of the shelf. Northwards along the south-eastern coast, the boundary between the TSW and the STSW flattens out and is in general found at ∼150 meters depth.

The plots of salinity and temperature in the upper layer (Figure 3.18a and 3.18c) show two upside-down dome-shaped structures with low salinity (S∼35.15) and high temperatures (∼23.5°C) in the surface layer 50 and 125 kilometers off the coast, both being a part of a larger upside-down dome-shaped structure. Close to the shelf in the upper 140 meters, the isohalines and isothermals are rising towards the coast, indicating upwelling. Below this depth, both the isohalines and the isothermals are

(a) *Salinity*

(b) *Dissolved Oxygen [mll^{-1}]*

(c) *Temperature [°C]*
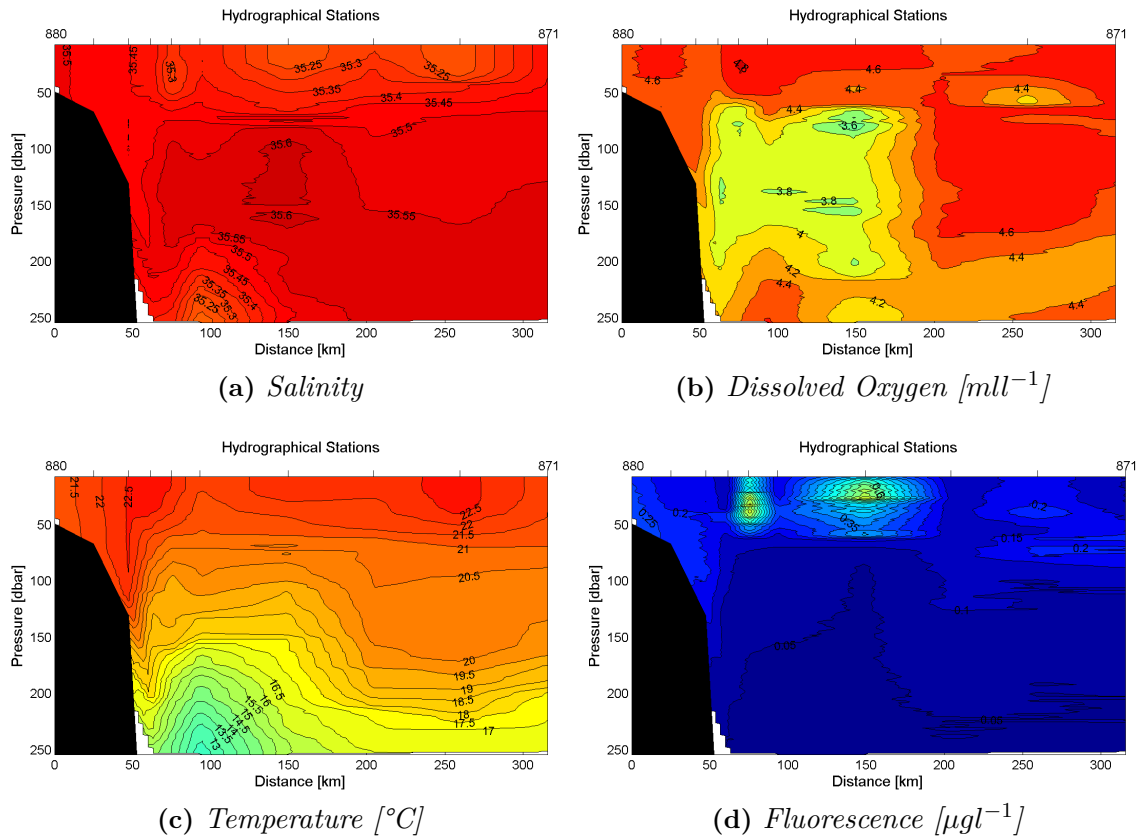

(d) *Fluorescence [µgl^{-1}]*

Figure 3.18: *Hydrographical transect 5. (a) Salinity, (b) Dissolved oxygen, (c) Temperature and (d) Fluorescence for the upper 250 meters. Ticks in the surface indicate CTD stations.*

indicating downwelling.

The fluorescence (Figure 3.18d) also indicates upwelling on the shelf, with high values (up to 1.28µgl^{-1}) in the surface layer above the shelf-break. This is the highest content of fluorescence measured in the entire research area. The surface water generally contains high values of oxygen (Figure 3.18b), except for in the surface layer above the shelf-break where the maximum fluorescence was observed. This is expected to be due to erroneous measurements due to the high concentrations of phytoplankton.

Upstream (Figure 3.1c and 3.1b) to transect 6 and 7 (not shown), the upside-down dome-shape observed in both the salinity and temperature of transect 5 (Figure 3.18a and 3.18c) fades out. A relatively sharp halocline is observed at ∼130 meters depth with some irregular patterns in salinity observed above. Both transect 6 and 7 indicate upwelling, but not as evident as in transect 5. The maximum fluores-

cence observed in the surface layer in transect 5 is gradually deepening and fading out northwards as the upwelling becomes weaker. In transect 7 (not shown) the fluorescence maximum ($\sim$0.17μgl^{-1}) is observed at $\sim$80 - 100 meters depth. As seen in transect 5, low oxygen is related to the highest fluorescence above the shelf-break. This was less evident in transect 7, as the fluorescence above the shelf-break was lower. An oxygen minimum is also observed immediately below the regions of high fluorescence.

(a) *Salinity*

(b) *Dissolved Oxygen [mll^{-1}]*

(c) *Temperature [°C]*

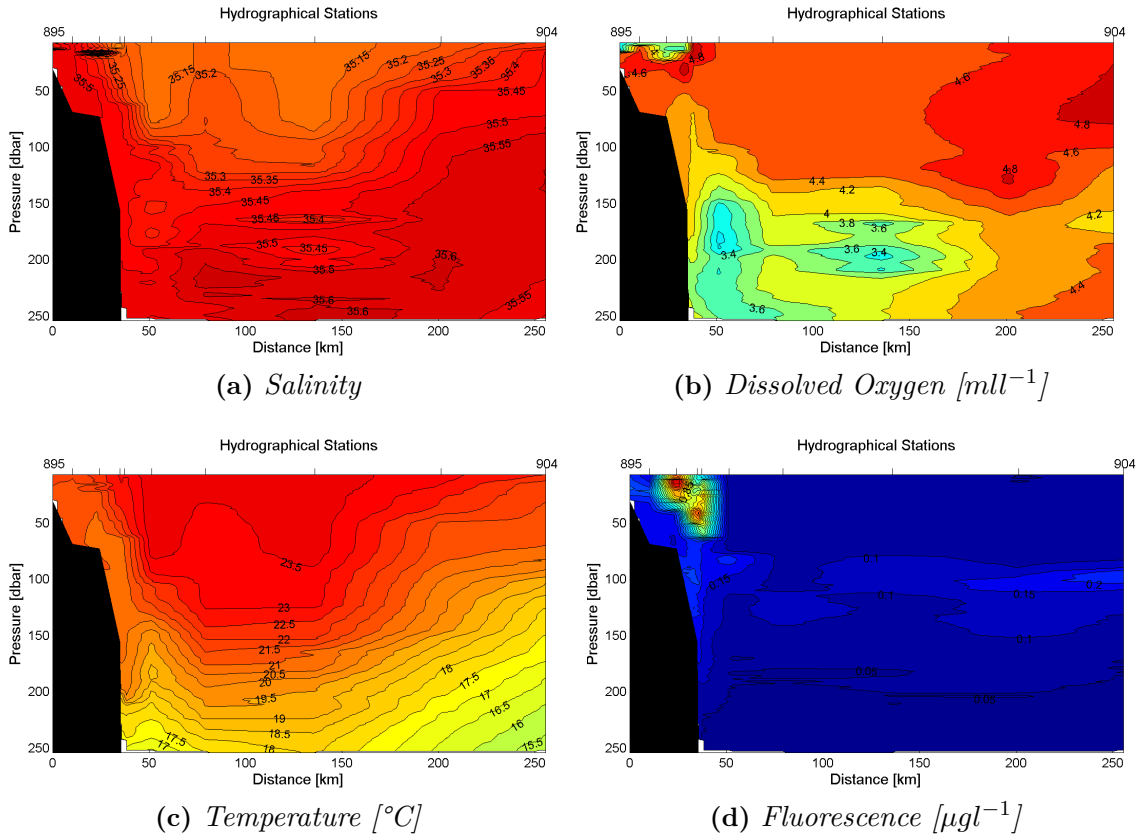**(d)** *Fluorescence [μgl^{-1}]*
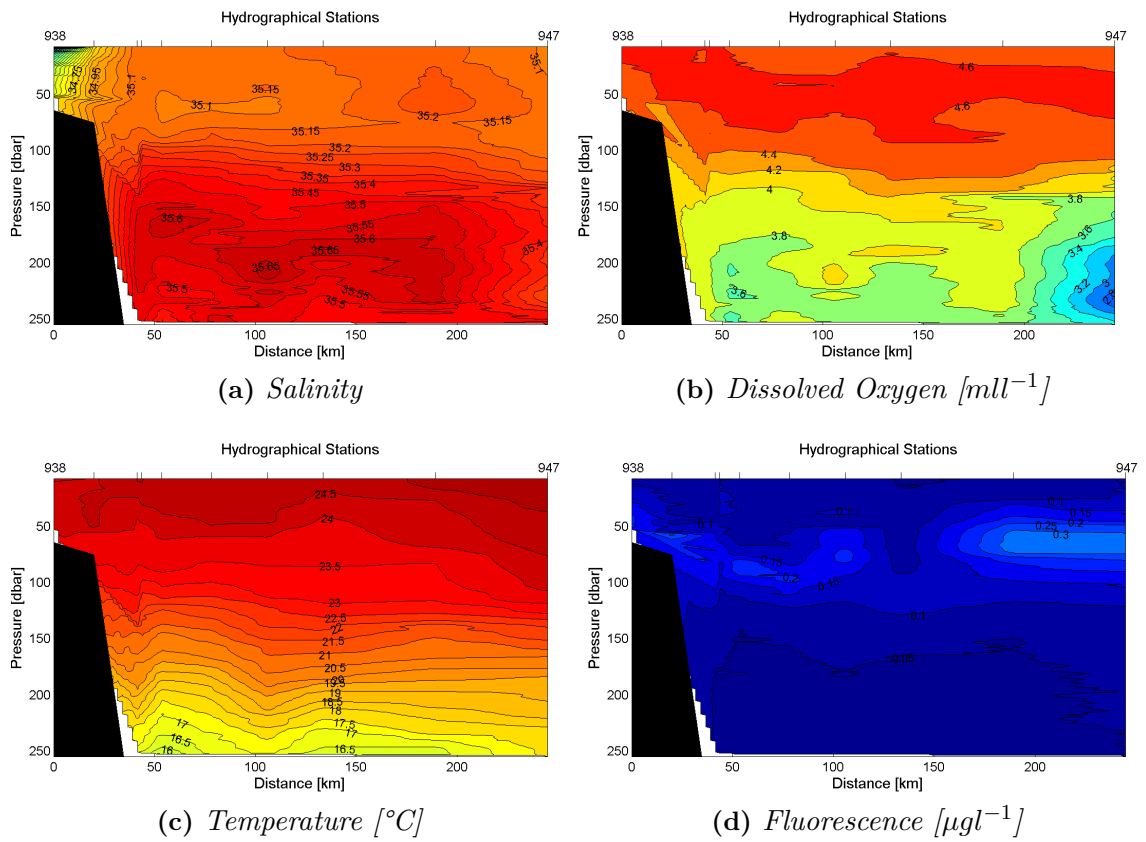
Figure 3.19: *Hydrographical transect 10. (a) Salinity, (b) Dissolved oxygen, (c) Temperature and (d) Fluorescence for the upper 250 meters. Ticks in the surface indicate CTD stations.*

At the north-eastern coast, the hydrographical structures in salinity and oxygen of transect 10 (Figure 3.19a and 3.19b), the central transect of the region, show a $\sim$140 meters thick layer of TSW in the inner 220 kilometers of the transect. The underlying STSW is in this transect limited to the inner 220 kilometers. The layer with salinity above 35.5 is only $\sim$60 meters thick. The thickness of the TSW is in general increasing northwards along the north-eastern coast, and in transect 12 (not shown), it is the only water mass recognized in the upper 250 meters.

On the shelf of transect 10, a layer of low salinity water (S∼32.7) is observed (Figure 3.19a). The water is fresher than any of the other water in the transect, indicating that this is due to fresh water run-off. On the shelf, the isohalines are almost vertical, indicating that the water column is well mixed. Such a pattern was observed in the inner part of transect 11 as well, but not as evident as in transect 10. Outside the shelf-break of transect 10, in deeper waters, the isohalines and isothermals (Figure 3.19a and 3.19c) indicate downwelling. Note that the region just outside the shelf-break is not too good resolved by the hydrographical stations. The strength of the downwelling seems to increase northward along the north-eastern coast (not shown). The temperature of transect 10 is high in the surface layer (up to 25°C, Figure 3.19c), both in the relatively fresh water close to the coast and further offshore. The isothermals are relatively horizontal, but a dip in the temperature close to the shelf from about 50 meters depth is observed.

The content of fluorescence is generally low (up to 0.32 $\mu g l^{-1}$) along the north-eastern coast, and the maximum fluorescence is found at ∼60 - 80 meters depth (Figure 3.19d). The water column is in general getting fresher and warmer and the content of oxygen in the surface layer is decreasing northwards (not shown).

3.6   Summary Results

The currents of the southern shelf are in general relatively barotropic (Figure 3.4). At the inner shelf, closest to the coast, the currents are directed westwards (Figure 3.3), while they are easterly directed further off shore (Figure 3.1c). South of the 1000 meters isobath, the current are more irregular and influenced by both cyclonic and anticyclonic eddies. The anticyclonic eddies seems to be the largest and most powerful. At the south-eastern coast, the currents are in general southwards directed closest to the coast and northwards directed outside. They are increasing in strength southwards from the bifurcation zone (∼19°S)(Figure 3.1b and 3.1c). At the north-eastern coast (Figure 3.1a), the currents are in general northerly directed, only interrupted by some irregularities. The strength of the northwards directed current is increasing northwards from the bifurcation zone. A westwards directed jet is observed around the northern tip of the island.

The modeled and observed wind distribution of the research area (Figure 3.7) coincides relatively well. The modeled mean monthly wind of September also coincides

to a high degree with the large scale current patterns of the eastern coast.

The horizontal distributions of SSS and SST (Figure 3.8 and 3.9) show that the surface water is in general fresher and warmer northwards. It is also seen that the water is more saline and colder closest to the southern and south-eastern coasts. Patches of high SSF (Figure 3.10) is also observed closest to the coast in these areas. A tongue of fresh, warm and fluorescence rich water is observed from outside the south-eastern corner of the island and south-westwards. The vertical distribution of the water masses reveal that the thickness of the TSW increases northwards along the coast. At the southern coast the thickness of the TSW seems to be highly influenced by the eddies, depressing or rising the isohalines and isothermals. In the southern region, the SICW with its oxygen maximum is evident at $\sim$300 - 700 meters depth. Northwards along the eastern coast, the SICW seems to become less evident. At the southern coast it is difficult to separate between the AAIW and the RSIW in the intermediate waters, but it is in general seen that the RSIW is located closest to the coast, and a little lower in the water column than the AAIW. The AAIW is generally replaced by the RSIW northwards along the eastern coast. The temperature is increasing northwards, lifting the water masses in the TS and TO_2 diagrams. The layer of RSIW is thicker in the north-eastern region than in the southern and south-eastern regions. The highest values of fluorescence are in general found at $\sim$50 - 80 meters depth, except of transects with upwelling, where high values are found in the surface above the shelf-break.

Chapter 4

Discussion

4.1 Current Dynamics

4.1.1 The South Equatorial Current

As observed in the horizontal current distribution at 44 meters depth (Figure 3.1b), the current splits at ∼19°S. For the equation of continuity to be fulfilled, there needs to be an inflow of water from the Indian Ocean. This westwards directed current is known as the SEC. To explain the location of the zonal SEC, the Sverdrup transport is taken into account. The Ekman pumping is generated by the curl of the wind stress, which leads to meridional transport. The Sverdrup relation for meridional transport is given by Equation 4.1.

$$V_{mer} = \frac{1}{\beta_0 \rho_0} (\nabla \times \vec{\tau}) \vec{k} \tag{4.1}$$

V_{mer} is the meridional transport, $\frac{df}{dy} = \beta_0 = constant$, ρ_0 is the density of the water, $\vec{\tau}$ is the wind stress and $\vec{k}$ is the vertical unit vector (Cushman-Roisin & Beckers, 2009). The mean monthly MERRA wind distribution for September 2008 (Figure 3.7) indicates that the vorticity is ∼0 at ∼19°S. This leads to small meridional transports, hence, the transport needs to be zonal. Sætre & Da Silva (1984) found that the hitting point of the SEC was dependent on the monsoon season. The flow of the SEC is persistent both during the north-eastern and south-western monsoon, but it appears to be stronger during the north-eastern monsoon. This cruise was carried

out in September, which is in the end of the south-western monsoon period (July-September) (Bearman *et al.*, 2004). The SEC is the northern part of the Southern Hemisphere Anticyclonic Gyre, and it is driven mainly by the local wind stress and the flow of the interior Subtropical gyre, but there is also a smaller contribution from the Indonesian throughflow (Quadfasel & Swallow, 1986; DiMarco *et al.*, 2002).

The horizontal distribution of the currents at 44 meters depth (Figure 3.1a) shows that the strength of the northwards directed EMC is increasing between 13.5°S and 11.5°S. An increase in the strength of the current northwards indicates that the SEC is wide and contributes with inflow of water all the way to the northern tip of Madagascar. This will be discussed further together with the volume transport in Section 4.1.5. At the northern part of the coast, a jet is observed. This strong but narrow jet is observed only during the south-western monsoon (Quadfasel & Swallow, 1986).

4.1.2   Bifurcation of the SEC

When the SEC hits the coast of Madagascar, it is expected to choose one way around the island; either south or north. The horizontal distribution of the currents (Figure 3.1b) reveals that this is not the case. When the SEC hits the coast at ∼19°S, it bifurcates into a northwards and a southwards directed branch of the EMC. One possible explanation of this bifurcation is found by looking at the conservation of the potential vorticity (Equation 4.2).

$$\frac{d}{dt}\left(\frac{\zeta + f}{H}\right) = 0 \;\Rightarrow\; \frac{\zeta + f}{H} = \text{constant} \tag{4.2}$$

The relative vorticity, ζ, is given by $\zeta = \frac{\partial v}{\partial x} - \frac{\partial u}{\partial y}$, f is the planetary vorticity and H is the thickness of the water column (Cushman-Roisin & Beckers, 2009). The relative and planetary vorticity of transect 3, 5 and 11 are given in Table 4.1. They are calculated by using the velocity gradients found in the contour plots of transect 3 (not shown), 5 and 11 (Figure 4.4a and 4.4c). Table 4.1 shows that the relative vorticity of the transects are of the same order of magnitude as the planetary vorticity. Hence, the requirement $|\zeta| << |f|$ is not fulfilled and the relative vorticity can not be neglected.

At the Southern Hemisphere (SH), the Coriolis parameter is negative and increasing

Table 4.1: *Planetary and relative vorticity for transects 3, 5 and 11.*

Transect	Planetary vorticity f [s^{-1}] $\times 10^{-5}$	Relative vorticity ζ [s^{-1}] $\times 10^{-5}$
3	-6.6	-2.8
5	-6.2	2.0
11	-4.1	-1.0
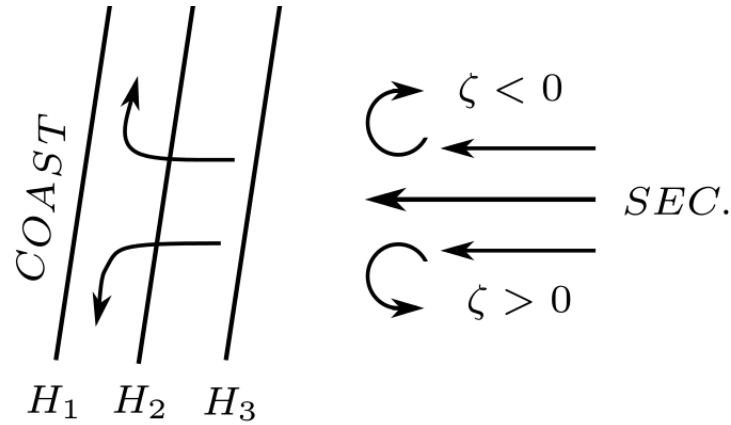
Figure 4.1: *Principle drawing of the bifurcation of the SEC into a northwards and southwards directed branch of the EMC. $H_1 < H_2 < H_3$, where H is the thickness of the water column and ζ is the relative vorticity.*

in magnitude polewards. When the SEC reaches the eastern coast of Madagascar, the thickness of the water column (H) is decreasing fast, as the slope of the shelf is steep. For the potential vorticity (Equation 4.2) to be conserved, the absolute value of the numerator ($|\zeta + f|$) needs to decrease. At the SH, the requirement could be fulfilled in the following ways:

- $\zeta < 0$:

    Northwards directed current and/or decreasing negative ζ

- $\zeta > 0$:

    $|\zeta| < |f| \Rightarrow$ Northwards directed current and/or increasing positive ζ

    $|\zeta| > |f| \Rightarrow$ Southwards directed current and/or decreasing positive ζ

Changing the planetary vorticity, f, is a much slower process than changing the relative vorticity, ζ. Hence, the relative vorticity will start making eddies. This might explain the eddy-like feature in transect 10 (Figure 3.1a). As the data used in this thesis represents a not synoptic snapshot with no temporal resolution, there

is no point in calculating the change in relative vorticity northwards or southwards along the coast.

A second possible explanation of the bifurcation is related to the wind system. The mean monthly MERRA wind distribution of September 2008 (Figure 3.7), reveals that the wind bifurcates at ∼19°S into a northwards and southwards directed flow around the island. The pattern in the measured ADCP current system at the eastern coast (Figure 3.1b and 3.1a) coincides to a high degree with the MERRA wind distribution of September 2008. South of the bifurcation, the frictional wind stress induces an Ekman transport away from the coast. Hence, a pressure gradient force is set up towards the coast. The Coriolis force acts to the left of the movement (away from the coast), and contributes to a southwards directed geostrophic current. North of the bifurcation, the frictional wind stress induces an Ekman transport towards the coast. Hence, the pressure gradient force is directed away from the coast. The Coriolis force is directed to the left of the movement (towards the coast), and contributes to a northwards directed geostrophic current.

Another possible explanation for the southwards directed current is also related to the wind system. The southwards directed branch of the EMC is possibly explained by the need of a western boundary current, for the vorticity balance of the Indian Ocean to be fulfilled. This will be discussed further in the next section.

It should also be noted that the SEC hits the coast oblique to the coast-line. This angle favor a southerly directed flow.

This bifurcation was also observed by e.g. DiMarco *et al.* (2002), to be located at ∼20°S, using ship drift and subsurface float tracks.

4.1.3   The East Madagascar Current

The winds of the southern Indian Ocean form an anticyclonic circulation, where the zonal wind, hitting the eastern coast of Madagascar, forms the northern boundary. In the north-western part of the circulation, Madagascar presents a western boundary. This part of the discussion will again be based on the conservation of potential vorticity (Equation 4.2). Changes in H do not affect the steady state requirement that the vorticity over the whole gyre must be constant, as one circuit in the gyre results in no net change in vorticity, hence for simplicity, H is chosen to be constant.

$$\frac{d}{dt}(\zeta + f) = \text{sum of frictional effects} \tag{4.3}$$

The contribution to the relative vorticity from the wind is positive for the entire southern Indian Ocean. The relative vorticity in the current increases along the western boundary and decreases along the eastern boundary. Hence, there is a net increase of relative vorticity along the western boundary and no net change in the relative vorticity along the eastern boundary. For the vorticity balance in the southern Indian Ocean to be fulfilled, a strong western boundary current with a strong negative velocity shear towards the coast, is needed (Pond & Pickard, 2007). This pattern is observed in both the horizontal current field of the south-eastern region (Figure 3.1b and 3.1c) and in the vertical distribution of the currents along transect 5 (Figure 3.5a). A narrow and intense western boundary current was also observed by Lutjeharms *et al.* (1981). Penven *et al.* (2006) state that the western boundary currents are driven by zonally integrated wind-stress curl over the width of subtropical basins.

The high velocity core of the southwards directed branch of the EMC follows the shelf-break along the entire coast, indicating that the current is topographically steered. For comparison, the Agulhas current and the trajectories exhibits great stability along the near uniform, narrow continental shelf at the south-eastern coast of Africa. The steep slope stabilizes the Agulhas current (Lutjeharms & de Ruijter, 1996). The same kind of bathymetry is found at the eastern coast of Madagascar, hence, the same behaviour is expected from the southwards directed branch of the EMC.

At the south-eastern corner of the island, it is observed both in the horizontal (ADCP) current field (Figure 3.1c) and in the vertical distribution of the currents in transect 5 (Figure 3.5), that the current is southwards directed in the inner half of the transect, while it is northwards directed in the outer half of the transect. This could possibly be explained by a retroflection of the EMC when it leaves the coast of Madagascar. One argument for the northwards directed current in the outer half of transect 5 to be the retroflection of the southwards directed branch of the EMC, can be seen in the hydrographical transects of salinity and temperature of the upper 250 meters of the transect (Figure 3.18a and 3.18c). The relatively warm and fresh TSW is expected to be connected to the southwards directed branch of the EMC. By comparing the width of the upside-down dome-shape of relatively fresh and warm water with the width of the current (Figure 3.5a), it is seen that

the upside-down dome-shape in transect 5 ($\sim$250 kilometers) is about as wide as both the southwards and the northwards directed current ($\sim$250 kilometers). This indicates that the water masses of both currents originate from the same region. Further, this indicates that these are two parts of the same current, retroflecting towards north-east at the south-eastern corner of the island. This retroflection is difficult to observe in the horizontal distribution of SSS, SST and SSF (Figure 3.8, 3.9 and 3.10), as the area where the current is expected to retroflect is not covered by direct measurements from the thermosalinograph. The retroflection is not observed in the SeaWIFS images of the region (Figure 4.10a) either. This may be explained in two ways: (1) The chlorophyll rich water from the south-eastern coast of Madagascar is located in the very inner part of the EMC, hence, is not likely to retroflect (Quartly *et al.*, 2006) and; (2) The retroflection seems to vary in time, and the SeaWIFS pictures are averaged for one period over 10 years, hence, the pattern of the retroflection may have been smoothed out. By looking at a run of the ocean current model; the Regional Ocean Modeling System (ROMS, Figure 4.2) from September the 9th, 1996, it is seen that it has succeeded in reproducing the observed pattern of a retroflection at the south-eastern corner of the island.
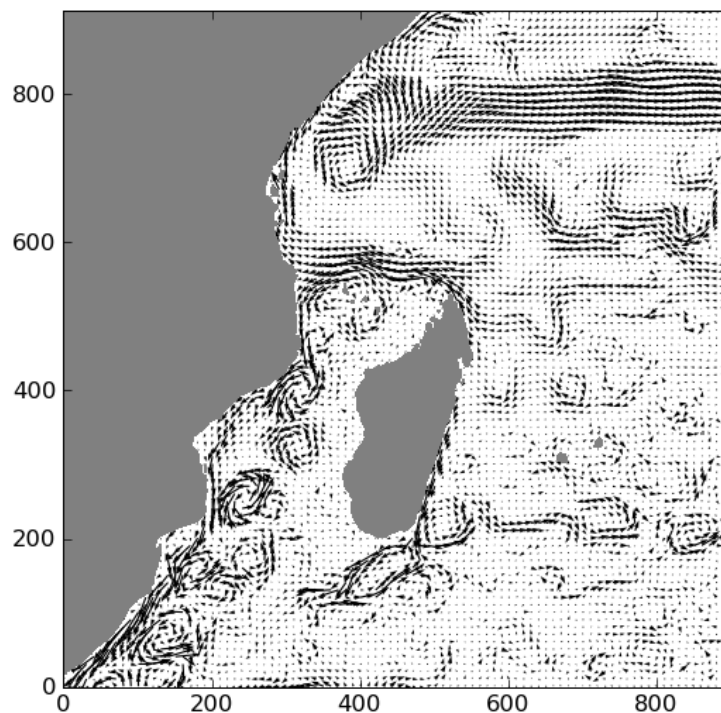

Figure 4.2: *ROMS: Mean horizontal current field for September the 9th, 1996. Arrows indicate horizontal currents (The model is run by Paul Budgell and the output data is plotted by Ingrid A. Johnsen).*

Two possible theories explaining the retroflection of the EMC are; (1) By applying the equation for conservation of potential vorticity (Equation 4.2). When the current enters the shallower southern region, the thickness of the water column (H) decreases. The planetary vorticity, f, is more negative southwards and the relative vorticity, ζ, is forced to become increasingly positive. Hence, positive (anticyclonic) vorticity is induced, causing the retroflection. (2) When the current leaves the coast, the pressure gradient force set up towards the coast disappears, and an inertial motion towards the left is possible. The Coriolis force is then balanced by the centripetal force. However, the radius in the corresponding inertial circle was calculated to be only $\sim$24 kilometers, while the observed radius of the retroflection is $\sim$120 kilometers.

The retroflection of the EMC might also explain the observed acceleration of the EMC southwards along the south-eastern coast (Figure 3.1b and 3.1c). It seems to feed the EMC with water as it propagates southwards. The intermediate water of the retroflected part of the current contains more AAIW than the water located in the inner part of transect 5 (Section 3.5.1).

The retroflection of the EMC was also observed by Lutjeharms & Machu (2000), using remote sensing methods. By using satellite remote sensing and surface drifters, Lutjeharms *et al.* (1981) observed that the high velocity core of the EMC is restricted to the edge of the continental slope and the speed of the EMC increases downstream. They also observed and concluded that the EMC retroflects, and when it does so, various eddies and current fragments may become detached. Lutjeharms & Machu (2000) state that the EMC retroflects at 27°S. In this study, one part of the current seems to be directed south-westwards while the rest of the current seems to retroflect. Lutjeharms *et al.* (1981) also claim that the leakage of a strong westerly directed current right south of Madagascar is an evidence supporting the theory of a retroflecting EMC. Lutjeharms & Machu (2000) claim that there is no indication of any subsequent westward penetration of the current's water, apart from inside the eddies travelling westwards.

4.1.4   Geostrophic Approximation

In a geostrophic flow, the Coriolis force is balanced by the pressure gradient force. The geostrophic shear flow was calculated by using the thermal wind equation, Equation 4.4 (Pond & Pickard, 2007).

$$\frac{\partial}{\partial z}(\rho V_H) = -\frac{g}{f}\frac{\partial \rho}{\partial n_H} \tag{4.4}$$

ρ is the density, V_H is the horizontal velocity and n_H is the direction perpendicular to the direction of the current, g$\sim$9.81 ms^{-2} is the gravitational constant. The Coriolis parameter $f = 2 \times \Omega \times \sin \phi \approx -0.5 \times 10^{-4}$ s^{-1}, where $\Omega = 7.2921 \times 10^{-5}$ $rads^{-1}$ is the angular velocity of the earth and ϕ is the latitude.
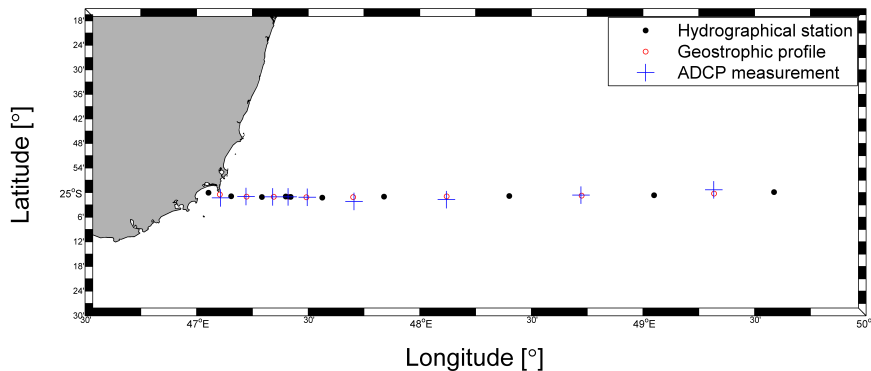

Figure 4.3: *Location of the hydrographical stations, the calculated geostrophic velocity profiles and the ADCP measurements used for adjusting the geostrophic velocity profiles of transect 5.*

The geostrophic velocity profiles are calculated halfway between two stations in the hydrographical transects (Figure 4.3). At a reference level, the velocity is set to the velocity measured by the ADCP at the same location and depth. The reference level is chosen to 176 meters or the bottom depth, based on the quality of the ADCP measurements. The calculated geostrophic velocities are directed perpendicular to the transects.

Figure 4.4 shows that the geostrophic approximation in general coincides well with the observed (ADCP) current velocities both in the south-eastern region (transect 5, Figure 4.4a and 4.4b) and in the north-eastern region (transect 11, Figure 4.4c and 4.4d). The accordance between the observed (ADCP) current velocities and the calculated geostrophic velocities seems to increase with increasing current velocities.

The geostrophy does not fully explain the dynamics of the current system, e.g. terms describing friction is not taken into account. This could e.g. lead to errors close to the coast and in the surface and bottom Ekman layer. In the plots of the calculated geostrophic velocities (Figure 4.4b and 4.4d), straight lines between the hydrographical stations are assumed. As the vessel did not move in perfect lines, the patterns are observed closer to the coast in the plots of the geostrophic currents
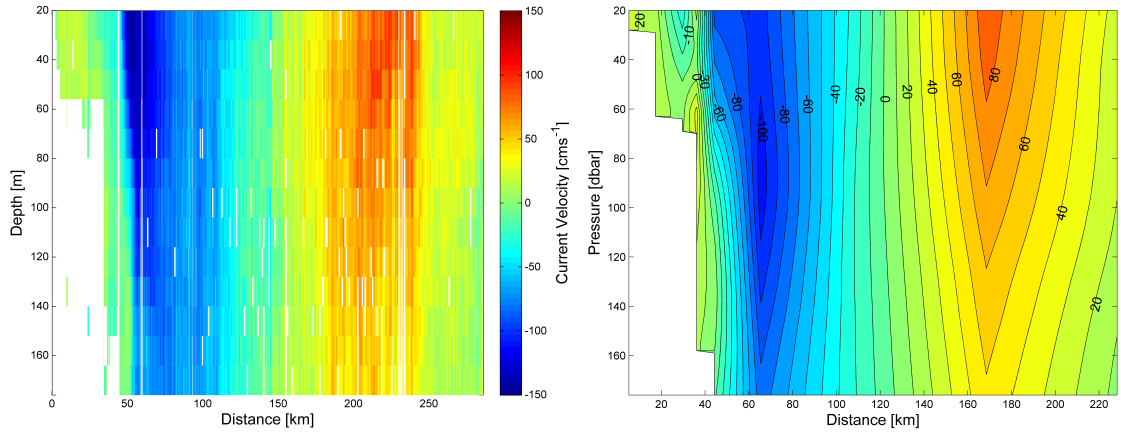
(a) *ADCP: Current velocity northwards, transect 5.*

(b) *Calculated geostrophic velocity [cms^{-1}] northwards, transect 5.*
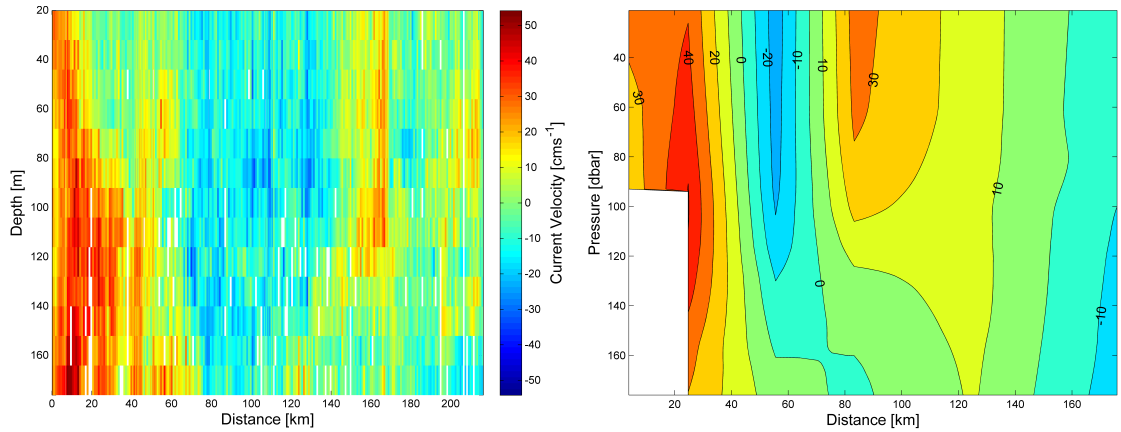
(c) *ADCP: Current velocity northwards, transect 11.*

(d) *Calculated geostrophic velocity [cms^{-1}] northwards, transect 11*

Figure 4.4: *(a) Northwards directed current velocities measured by the ADCP, transect 5. (b) Northwards directed calculated geostrophic velocities, transect 5. (c) Northwards directed current velocities measured by the ADCP, transect 11. (d) Northwards directed calculated geostrophic velocities, transect 11. The general rinsing process is turned off, and the PG limit is set to 95%. The reference level is chosen to 176 meters depth. Note that (a) and (b) are not to scale with (c) and (d).*

(Figure 4.4b and 4.4d) than in the plots of the observed (ADCP) currents (Figure 4.4a and 4.4c).

4.1.5 Volume Transport of the EMC

By calculating the volume transport of the northwards and southwards directed branch of the EMC through several of the transects, it is possible to describe

the progress of the current northwards and southwards from the bifurcation zone (∼19°S). The volume transport through the transects are calculated by using Equation 4.5.

$$V = \int_0^L \int_{z=-h}^0 v \ dzdx \tag{4.5}$$

V is the volume transport, L is the width of the transect, h is the thickness of the water column and v is the velocity perpendicular to the transect.

As the ADCP measurements are limited to ∼180 meters depth, geostrophy needs to be assumed to calculate the volume transport down to 3000 meters depth. The geostrophic velocity profiles are adjusted by the ADCP measurements at 176 meters depth, or at the seabed. For comparison, volume transports using 20 meters depth as a reference level, are calculated. Volume transports between 14 and 182 meters depth are calculated for comparison with the volume transports measured by the ADCP. Geostrophic volume transports where v=0 at z=-h are also calculated.

The volume transports are calculated through the inner 136 kilometers of transect 5, the inner 153 kilometers of transect 11, and the inner 142 kilometers of transect 12.
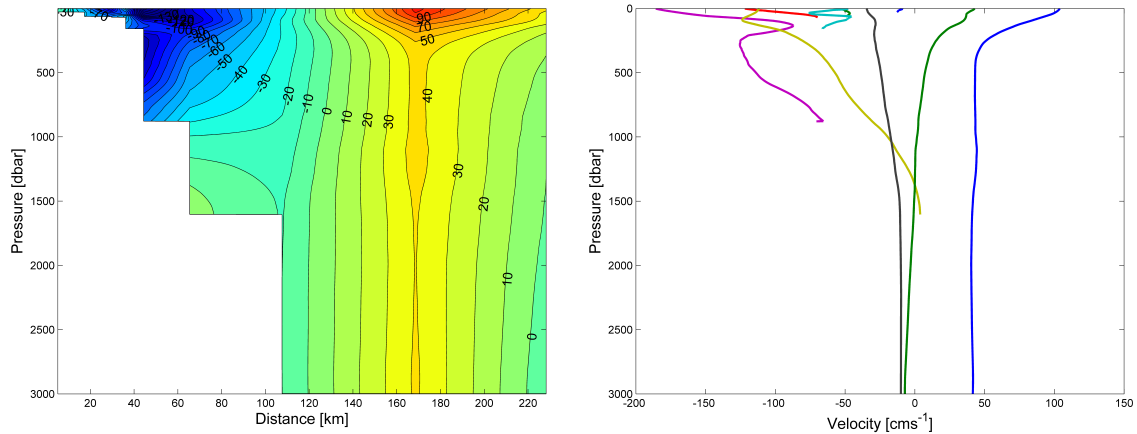
(a) *Calculated northwards geostrophic current velocities [cms⁻¹], transect 5.*

(b) *Geostrophic current velocitiy profiles, transect 5.*

Figure 4.5: *Geostrophic current velocities [cms⁻¹] down to 3000 meters depth for transect 5, adjusted with respect to ADCP measurements at 176 meters depth.*

Table 4.2 indicates that the observed (ADCP) and calculated geostrophic volume transports in the upper layer (14 - 182 meters) coincides well for all three transects.

Table 4.2: *Geostrophic volume transport through transects 5, 11 and 12.*

	Transect 5 136 km	Transect 11 153 km	Transect 12 142 km
ADCP obs. 14 - 182 m.	7.8 Sv S	0.4 Sv N	15.8 Sv NW
Calc. 14 - 182 m. Ref. level 176 m.	7.0 Sv S	0.4 Sv N	14.4 Sv NW
Upper 3000 m. Ref. level 176 m.	25.7 Sv S	21 Sv N	61 Sv NW
Upper 3000 m. Ref. level 20 m.	42 Sv S	53 Sv S	127 Sv NW
Upper 3000 m. v(3000)=0	34 Sv S	9 Sv N	15 Sv NW

The observed volume transports are generally slightly larger, or the same, as the calculated volume transports. Geostrophy adjusted by the observed currents at 176 meters depth is a good approximation.

The volume transports calculated down to 3000 meters depth using 20 meters depth as a reference level, are generally larger, and for transect 11, even oppositely directed than the volume transports through the same cross section calculated using 176 meters depth as a reference level. This could possibly be explained by the currents at 20 meters depth being directly influenced by the wind. As there are large distances between some of the hydrographical stations and the water column is very thick (3000 meters), the volume transports are very sensitive to errors in the measured current velocities at the reference level.

Table 4.3: *Geostrophic volume transports of the EMC calculated by Swallow* et al. *(1988), Schott* et al. *(1988) and Lutjeharms* et al. *(1981) compared to those calculated in this thesis (Voldsund).*

	Swallow		Schott		Lutjeharms		Voldsund	
Methods: CTD +					Surf. drifter		ADCP	
Position [°S]	12	23	12	23	12	23	12	25
Reference depth [m]	1100	1170	1100	1170	-	0	176	176
Transect length [km]	115	110	115	110	-	-	142	136
Transect depth [m]	1100	1170	1100	1170	-	500	3000	3000
Volumetransport [Sv]	**30**	**21**	**27**	**20**	-	**41**	**61**	**26**

Swallow *et al.* (1988) and Schott *et al.* (1988) calculated the volume transports using 1100 and 1170 meters as reference levels, but in contrast to what is done in

this thesis, the velocity is set to zero at the reference level. Both Swallow *et al.* (1988) and Schott *et al.* (1988) compared their results with volume-transports calculated in the upper layer using both current meter moorings and ADCP. The comparison showed good results. This could be explained by the geostrophic velocity being small at this depth for the southern branch of the EMC (not shown). Table 4.3 shows that the volume transports calculated in this thesis are according well with those calculated by Swallow *et al.* (1988) and Schott *et al.* (1988). The larger deviation between the volume transports in transect 12 (12°S) than in transect 5 (25°S) could be explained by transect 12 having a much larger cross section between the two reference depths. This leads to larger volume transports between ∼1100 and 3000 meters depth in transect 12 than in transect 5.

The volume transport calculated by Lutjeharms *et al.* (1981), 41 Sv for the upper 500 meters at 23°S, is much larger than the volume transport calculated in this thesis, 25.7 Sv for the upper 3000 meters at 25°S. This could be explained by the fact that Lutjeharms *et al.* (1981) used the surface as the reference level. This gives a transport almost as large as for the full depth (42 Sv, 3000 meters) using 20 meters depth as reference level (Table 4.2). This transport is overestimated due to influence from the wind.

Swallow *et al.* (1988) state that the directly recorded currents show no seasonal signal below 200 meters depth. Above 200 meters depth, historical data suggest a seasonal amplitude in transport of ±2 Sv at 23°S and ±0.2 Sv at 12°S.

As seen in Table 4.2, the volume transport increases northwards between transect 11 and 12. Due to continuity, there needs to be an inflow of water between these two transects. It is difficult to observe the nearly zonal incoming current in the ADCP measurements, as they are carried out close to the coast. By looking at the current field from a run of the Regional Ocean Modeling System (ROMS, Figure 4.2), an incoming current is observed between ∼13°S and 14°S. In the horizontal current field at 44 meters depth (Figure 3.1a), the northwards directed branch of the current is observed to accelerate between ∼13.5°S and ∼12°S. This coincides with the inflow of the north-westwards directed current observed in Figure 4.2, feeding the northwards directed branch of the EMC with water. This second current could be another branch of the SEC, in the literature referred to as a wide current by e.g. Bearman *et al.* (2004).

4.1.6   Water Masses

The horizontal distributions of SSS and SST (Figure 3.8 and 3.9) indicate that relatively fresh and warm TSW, influenced by the the relatively fresh IIW from the SEC, is advected southwards along the coast from the bifurcation zone by the southwards directed branch of the EMC. At the south-eastern corner of the island, the EMC leaves the coast. A tongue of relatively fresh and warm water is observed southwestwards from offshore the south-eastern corner of the island. This indicates that the EMC is not retroflected in its entirety, but that some of the current follows the bathymetry south-westwards into the southern region. This could possibly explain why what looks like the cyclonic eddy C2 (Figure 3.1c), in hydrographical transect 3, is related to downwelling patterns, with relatively fresh and warm surface water (Figure 3.17a and 3.17c) together with a large content of fluorescence in the surface layer (Figure 3.17d). This could possibly be explained by advection of relatively fresh and warm TSW water from the not retroflecting part of the EMC. The high fluorescence in the surface layer indicates that the water which does not retroflect, is originating from the upwelling cell inshore of the EMC at the south-eastern corner of the island. This is supported by Lutjeharms & Machu (2000). On the other hand, if the water advected south-westwards was only originating from the upwelling cell inshore the EMC, the water would be expected to be both more saline and colder. Another explanation for this tongue could be that the relatively fresh and warm water could be traced inside the anticyclonic eddies travelling south-westwards.

In Section 3.5, the intermediate waters at the southern and south-eastern coast of Madagascar was shown to consist of both AAIW and RSIW. The RSIW was located closest to the coast. Gründlingh *et al.* (1991) state that the RSIW flows southwards through the Mozambique Channel in the layer between the isopycnals 1027.0 and 1027.7. At the southern coast it interacts with the AAIW resulting in a variety of mixing and interleaving processes. At the south-eastern coast, the RSIW is advected southwards along the eastern coast with the EMC, while the content of AAIW is higher in the retroflected part of the current.

As the temperature gradients are small in the deep waters, it is difficult to distinguish between the intermediate and deep water masses in original TS and TO_2 diagrams. By plotting the salinity and oxygen against pressure for the southern and southeastern region (Figure 4.6), it is possible to differ between the deep water masses. The salinity and oxygen profiles of the north-eastern region follow the profiles of the south-eastern region very tight and is not taken into further consideration. Figure
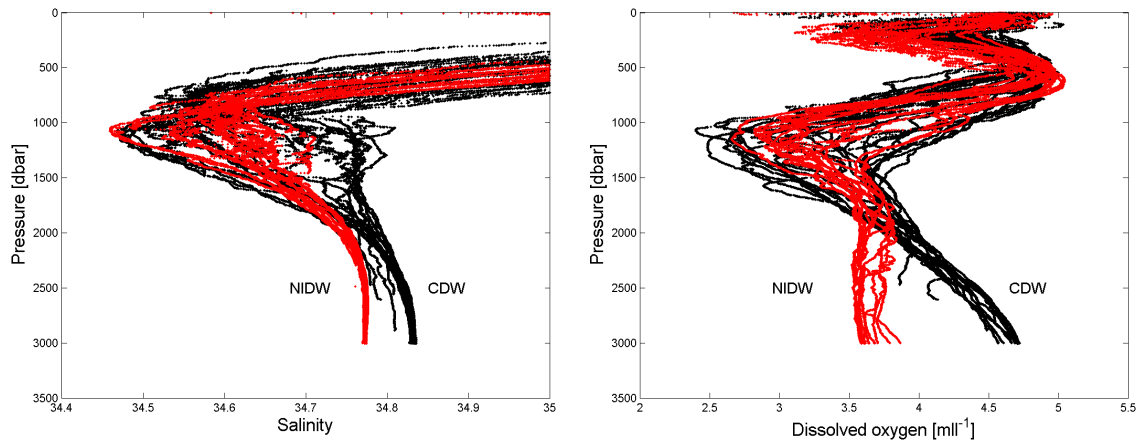
(a) *Salinity-Pressure, southern (black) and south-eastern coast (red)*

(b) *Dissolved oxygen-Pressure, southern (black) and south-eastern coast (red)*

Figure 4.6: *(a) Salinity plotted against pressure down to 3000 meters depth for the southern coast (black) and south-eastern coast (red). (b) Dissolved oxygen plotted against pressure down to 3000 meters depth for the southern coast (black) and south-eastern coast (red). Geographical boundaries are given in Table 2.1.*

4.6 indicates that the water masses of the southern and south-eastern region are separated by a sharp boundary below 2000 meters depth. The deep water masses (>2000 meters) of the southern coast, are both relatively saline (S~34.83) and carries high contents of oxygen (~4.6 mll^{-1}). At the south-eastern coast, the water masses are less saline (S~34.77) and contain less oxygen (~3.6 mll^{-1}). As seen in Section 3.3, the CDW is related to both high contents of oxygen and high salinities due to influence from the highly saline NADW, while the NIDW is characterized by both lower salinities and oxygen than the CDW (Park *et al.*, 1993).

One possible explanation of the sharp boundary in the deep water between the southern and south-eastern region, could be that the deep water masses originate from the Mozambique Channel. Then it would be reasonable to find the same water masses at the same depths there. By comparing the results of this survey with the results of the survey carried out by R/V Dr. Fridtjof Nansen between August the 26th and October the 2nd, 2009, it was seen that this high values of oxygen was not observed at all, not even at the southern coast (Pripp, 2011). This may indicate errors in the calibration of the oxygen sensor. The observed salinity between ~1500 - 3000 meters depth in the Mozambique channel was lower than the salinity observed at these depths at the southern coast. Hence, the sharp boundary at >2000 meters depth is most likely not caused by water flowing into the southern region from the Mozambique Channel.

A second, and more likely theory, is related to the retroflection of the EMC. As
the EMC seems to reach all the way down to the seabed (Section 4.1.5) and it is
expected to retroflect when it leaves the coast of Madagascar, it would act like a
boundary that hampers the CDW and NADW from being transported northwards
along the eastern coast. It should also be noted that the southern region is in general
shallower than the south-eastern region.

4.1.7 Eddies

At the southern shelf, the anticyclonic eddies A1, A2 and A3, and the cyclonic
eddies C1, C2 and C3 are observed in the horizontal current field carried out by
the ADCP (Figure 3.1c). The eddies could also be recognized in the hydrographical
transects, where the anticyclonic eddies are related to downwelling patterns with
warm and relatively fresh surface water, while the cyclonic eddies are related to
upwelling patterns with cold and relatively saline surface water. These patterns
are demonstrated in Figure 4.7, showing the hydrographical patterns of salinity and
temperature along transect 2. Inshore the large anticyclonic eddy A3 (Figure 3.1c),
the cyclonic eddy C3 may be observed in the temperature pattern. This pattern is
difficult to see in the hydrographical transect of salinity (Figure 4.7a). The upwelling
pattern seen in the temperature, could possibly also be explained by warm water
advected eastwards with the currents from the Mozambique Channel (Figure 3.1c).

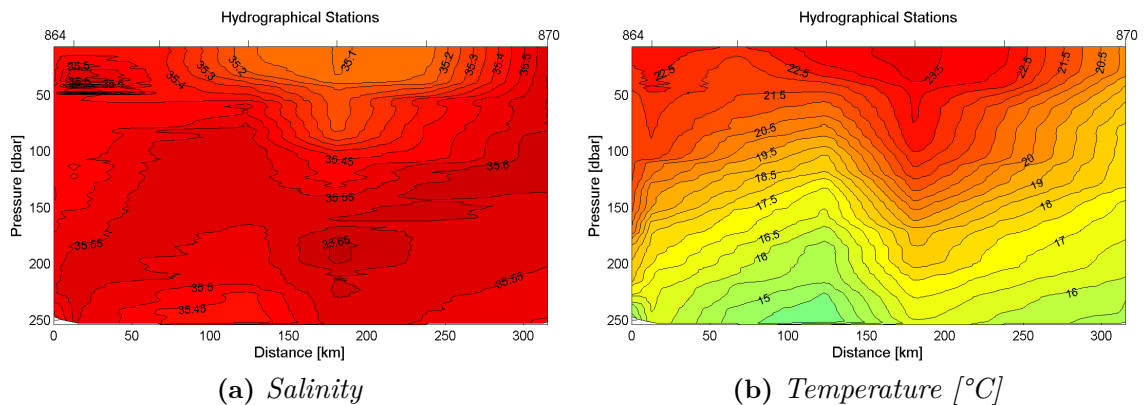**(a)** *Salinity*   **(b)** *Temperature [°C]*

Figure 4.7: *Hydrographical transect 2. (a) Salinity and (b) Temperature for the
upper 250 meters. Ticks in the surface indicate CTD stations.*

Both the horizontal current field (Figure 3.1c) and the hydrographical transects of
salinity and temperature (Figure 4.7) indicate that the center of the anticyclonic
eddy is located at hydrographical station 868.

As the density mainly depends on the temperature, it is observed that the pycnocline inside the anticyclonic eddy A3 is deeper than the pycnocline of the cyclonic eddy C3. The eddies are influencing the hydrographic pattern all the way down to 250 meters depth.

According to de Ruijter *et al.* (2004), some of the eddies at the southern coast of Madagascar seem to originate from east of Madagascar. As discussed in Section 4.1.3, anticyclonic (positive) relative vorticity, ζ, is induced when the southwards directed branch of the EMC leaves the south-eastern coast and enters the shallower southern region. This will stimulate positive vortex formation (anticyclonic eddies). The cyclonic eddies on the other hand, are generated before the EMC leaves the coast. Friction against the shore would create a narrow band of accumulated cyclonic (negative) relative vorticity at the inshore edge of the EMC (Figure 3.5a). This may contribute to the formation of cyclonic eddies at the inshore side of the separated jet. The same argument was used by Backeberg & Reason (2010) for the explanation of the formation of anticyclonic eddies at the northern coast of Madagascar. Lutjeharms *et al.* (1981) state that the EMC is shedding of vortices when it retroflects at the south-eastern corner of the island.

These mechanisms of the formation of the eddies could possibly explain the different hydrographical patterns inside the cyclonic and anticyclonic eddies. The cyclonic eddies seem to draw their water from inshore the EMC, an area of upwelling. They will then be connected to upwelling patterns. The anticyclonic eddies on the other hand, seem to draw their water from the EMC itself, which carries relatively fresh and warm water, often connected to downwelling.

The eddies could be classified by calculating the Rossby number, $R_0 = \left| \frac{U}{fL} \right|$ (non-linear term divided by Coriolis). U is the difference between maximum positive and maximum negative velocity in an arbitrary direction inside the eddy, L is the length scale of the variations, and f is the Coriolis parameter. The maximum change in velocity, U, inside A3 in transect 2, is $\sim$215 cms^{-1}, and the length scale, L, is $\sim$100 kilometers (Figure 4.8a). The planetary vorticity, f, is given in Table 4.1 to be -6.6$\times 10^{-5}$ s^{-1}. Then $R_0 = 0.32 < 1$, hence, the anticyclonic eddy A3 is classified as quasi-geostrophic. This is supported by Figure 4.8 showing the measured current (ADCP) velocities compared to the calculated geostrophic velocities adjusted by the ADCP measurements at 130 meters depth through C3 and A3 along transect 2 (Figure 3.1c).

The eddies propagate south-westwards at the southern coast of Madagascar with
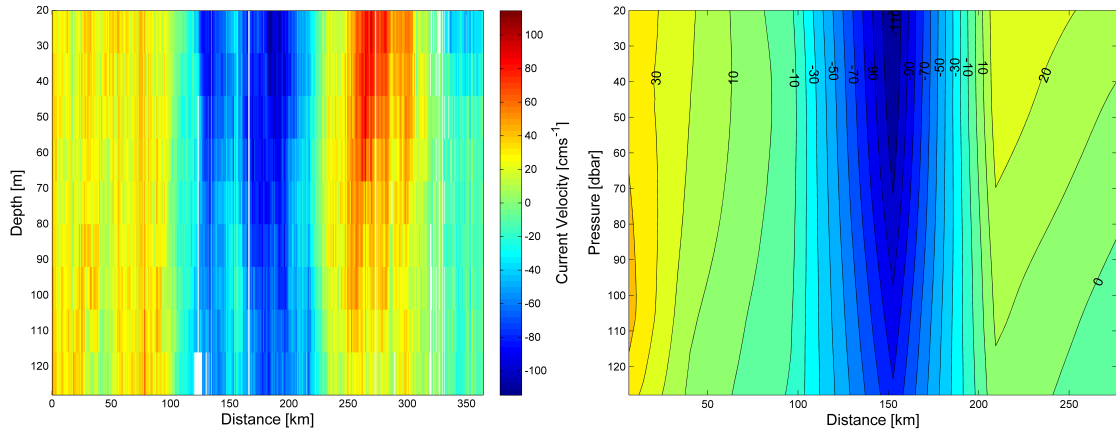
(a) *ADCP: Current velocity perpendicular to transect 2.*

(b) *Calculated geostrophic velocity [cms⁻¹] perpendicular to transect 2*

Figure 4.8: *(a) Current velocities perpendicular to transect 2, measured by the ADCP. (b) Calculated geostrophic velocities perpendicular to transect 2. The general rinsing process is turned off, and the percent good limit is set to 95%. Note that the distances from the coast are not to scale.*

speeds between 5 and 10 cms^{-1}, feeding the Agulhas current with water (de Ruijter *et al.*, 2004; Quartly *et al.*, 2006).

4.1.8 Tidal Influence

The tidal currents are calculated by the TPXO7.1 Global Inverse Tide Model. Time and position of the vessel is given by the ADCP, and the tidal currents are plotted at the track of the ship. In general, the contributions from the tides to the current system are very small, as the water column is in general very deep. The strongest tidal currents are found in the shallow areas of the southern shelf (Figure 4.9). The tidal components of the currents were not strong enough to reverse the measured currents at any location. The influence from the tides could only be seen as a minor rotation, or change in strength of the currents. The maximum tidal current calculated at time and position of the vessel is ∼65 cms^{-1}, close to the shore, east of Cap Ste-Marie. At this location, the in-situ currents measured by the ADCP (Figure 3.3) were small, hence, by removing the tidal contribution, the vectors rotated from being northerly directed to being north-easterly directed and increasing in magnitude.
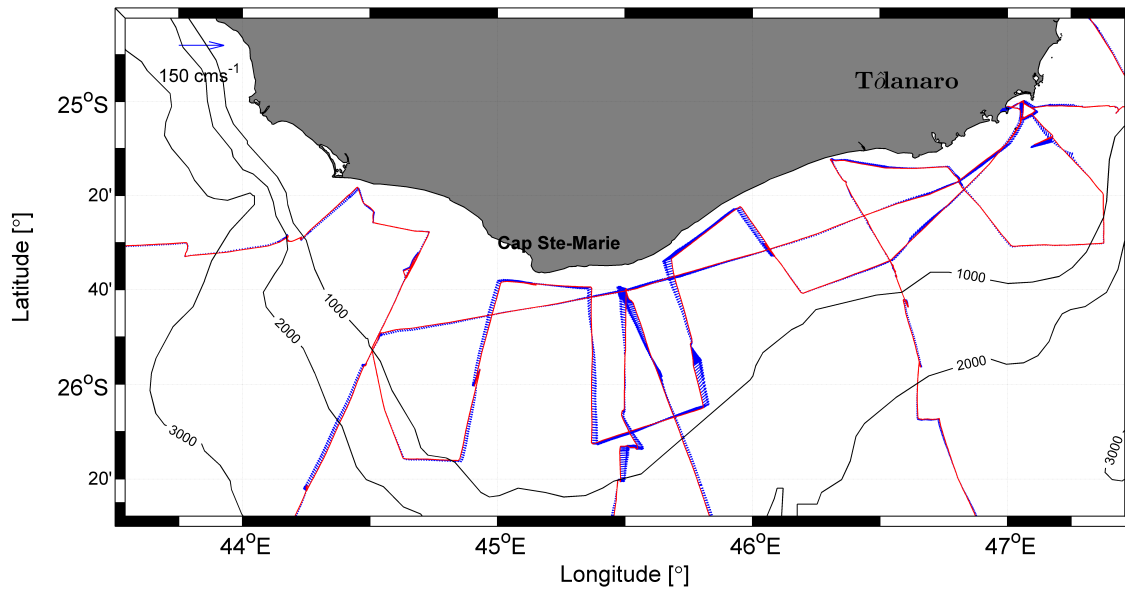
Figure 4.9: *TPXO7.1: Modeled tidal currents at the time and position of the research vessel. Velocity scale indicated in upper left corner.*

Tidal Mixing Fronts

To determine if there are possibilities for a tidal mixing front (a boundary between stratified and unstratified water set up by tidal currents (Mann & Lazier, 2006)) to develop at the southern shelf of Madagascar, the empirical relationship, Equation 4.6, is used (Brown & Bearman, 2006).

$$P = \frac{H}{u_s^3} \tag{4.6}$$

H is the thickness of the water column and u_s is the mean maximum surface tidal current speed (mean of maximum magnitude of the tidal current speeds on both floods and ebbs). If the value of P is between 70 and 80 $m^{-2}s^3$, a tidal front is expected to develop in shelf waters. On the other hand, if P is smaller than 70 $m^{-2}s^3$, a well mixed water column is expected, while if P is larger than $80m^{-2}s^3$, stratified conditions are expected (Brown & Bearman, 2006).

By looking at the hydrographical transects for salinity and temperature at the southern coast (transects 1 - 4), it is seen that the water column is to some extent mixed shallower than 50 meters depth. This mixing is most evident in transect 1 (not shown) and 3 (Figure 3.17a and 3.17c). Transect 3 is also the transect with the strongest tidal currents and will be the one investigated further.

For the inner part of transect 3, the mean maximum surface tidal current speed is calculated to ∼35 cms^{-1} (41.6 cms^{-1} maximum for that month, two weeks back and two weeks forth). The thickness of the water column is measured to ∼50 meters. By using Equation 4.6, P∼1166 $m^{-2}s^3$ » 80 $m^{-2}s^3$, and the tidal currents are not strong enough to be responsible for the mixed conditions. For a tidal front to develop in this area, the mean of maximum tidal current speeds, on both floods and ebbs, should exceed 85 cms^{-1}. The strongest tidal currents calculated for this cruise was 65.4 cms^{-1}. For a tidal front to develop with this tidal current, the water column should be less than ∼22 meters thick. Hence, the tidal currents are most likely not responsible for the mixing of the water column at the southern coast.

Even though the tidal currents are not strong enough for tidal fronts to occur, the tides could contribute to increase the turbulence at the shelf-break.

The oppositely directed currents observed at the southern shelf (Figure 3.3), when arriving and leaving the coast of Madagascar, are observed in a region with relatively strong tidal influence. Even though the tidal currents are compensated for, the currents are still not merging. Since the differences in the currents are this large, the reversal of the currents could possibly be due to an eddy passing by.

4.2   Up- and Downwelling

At the southern coast of Madagascar, the SSS and SST measured by the thermosalinograph (Figures 3.8 and 3.9) reveals relatively high SSS and low SST closest to the shore. This is also observed in the hydrographical transects, with isohalines and isothermals rising towards the coast at the inner part of the shelf (Figure 3.17a and 3.17c). Both these patterns are related to upwelling, where colder, more saline STSW is forced towards the surface. The upwelling is in general driven by the wind system in the surface Ekman layer, and by the current system in the bottom Ekman layer.

The MERRA mean monthly wind distribution of August 2008 (not shown) reveals a westwards directed zonal wind aligned with the southern coast, causing coastal upwelling. The MERRA mean monthly wind is more zonal in August than in September and October. It should be noted that the zonal (alongshore) component is almost disappeared in the mean monthly MERRA wind of October, hence, the wind-driven upwelling of this region is expected to be seasonal.

The currents at the inner part of the southern shelf (Figure 3.3) are in general directed westwards. A bottom drifted Ekman transport is set up by friction towards the seabed, and the transport in the bottom Ekman layer will be directed to the right of the current, in this case towards the coast. As the westwards directed currents seem to be limited to the inner part of the shelf, the bottom drifted upwelling will be limited to the same area. Outside the shelf-break the currents are in general directed eastwards, causing downwelling outside the shelf-break (Figure 3.17a and 3.17c). As the currents at the inner part of the southern shelf are relatively weak (Figure 3.3), it is reasonable to assume that the upwelling at the southern coast is mainly wind-driven.

An upwelling cell at the southern shelf was also observed in satellite pictures of the surface temperature in February by DiMarco *et al.* (2000). They showed that the wind of the season favor upwelling, but they did not exclude the possibilities for contributions from the currents.

At the south-eastern coast, the SSS, SST and the hydrographical transects of salinity and temperature (Figure 3.8, 3.9, 3.18a and 3.18c) reveal upwelling patterns. Both the horizontal distributions of SSS and SST (Figure 3.8 and 3.9) and the vertical transects (not shown) indicate that the strength of the upwelling is decreasing northwards. The structure of the upwelling at the south-eastern corner of the island is the strongest observed in the entire research area. Structures in salinity and temperature in transect 5 (Figure 3.18a and 3.18c) indicate that the upwelling patterns reach as deep as ∼130 meters. Below this depth, downwelling with descending isohalines and isothermals are observed. The reason why the upwelling reaches this deep could possibly be that both the southwards directed wind (Figure 3.7) and the southwards directed branch of the EMC (Figure 3.1c) contribute to the upwelling.

In addition to the Ekman transport in the bottom Ekman layer, Lutjeharms & Machu (2000) explained this intense upwelling cell inside the EMC with the changing characteristics of the current due to changes in the bathymetry. The narrow shelf widens sharply from being about 20 kilometers wide at the south-eastern coast, to being wider and shallower, with a weaker continental slope at the southern coast. They also state that there seems to be no correlation between the local wind and the presence of the upwelling cell. They claim the upwelling cell to be prevalent at about 25°S under all wind conditions. Hence, they suggest that the upwelling is current-induced, where the upwelling is mainly caused by divergence. This theory is based on similar studies at the Agulhas Bank, carried out by Gill & Schumann (1979),

where the upwelling was demonstrated not to be wind-driven. The configuration in the current at the south-eastern corner of Madagascar, is nearly identical to the one observed at the Agulhas Bank. Lutjeharms & Machu (2000) also noted that there are no rivers or influx of nutrients known in this region that could cause a phytoplankton bloom of the size they observed in their study.

The upwelling cell at the south-eastern corner of the island was also observed by Ho *et al.* (2004) by interpreting SeaWIFS pictures. They concluded that both current and wind stress were mechanisms causing the upwelling. Empirical orthogonal function analysis carried out by Ho *et al.* (2004), indicated that the EMC modulation is a significant factor responsible for the variability in the upwelling. The analysis showed strong interaction between the upwelling and the EMC. In a study from January to March 2000, DiMarco *et al.* (2000) pointed out that the upwelling at the south-eastern coast was concurrent with anomalously high wind stress of the region, showing that the upwelling at the south-eastern corner is driven both by the currents and the wind.

North of the bifurcation ($\sim$19°S), at the north-eastern coast, the hydrographical transects of salinity and temperature (Figure 3.19a and 3.19c) indicate downwelling. This is due to both winds and currents being northerly directed, resulting in an Ekman transport directed towards the coast in the surface Ekman layer, and away from the coast in the bottom Ekman layer.

The Ekman transport in the surface layer depends on the wind-stress and the Coriolis parameter only, while the Ekman transport in the bottom layer depends on the currents and Coriolis parameter only. As both the alongshore (meridional) wind and currents increase with increasing distance from the bifurcation along the eastern coast, the Ekman transport increases as well. This could also be seen in the hydrographical transects where the upwelling is strongest at the south-eastern corner (Figure 3.18a and 3.18c), and the downwelling is strongest at the northern tip of the island (not shown).

4.3   Influence on the Biology

4.3.1   Phytoplankton
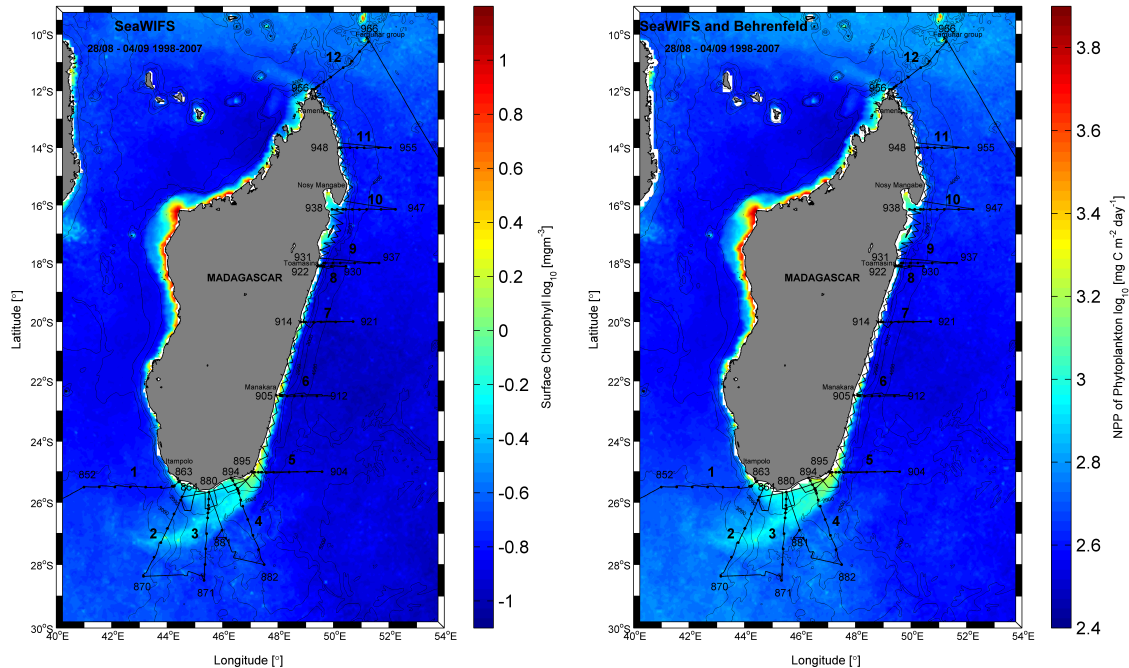
(a) *SeaWIFS: Chlorophyll in the surface: August the 28th to September the 4th, 1998 - 2007*

(b) *SeaWIFS and Behrenfeld: NPP of phytoplankton integrated through the water column: August the 28th to September the 4th, 1998 - 2007*

Figure 4.10: *SeaWIFS (Satellite): (a) Average horizontal distribution of surface chlorophyll August the 28th to September the 4th, 1998 - 2007. (b) Average NPP of phytoplankton integrated through the water column August the 28th to September the 4th, 1998 - 2007. C is carbon. Vessel course track, 1000, 2000, 3000, 4000 and 5000 meters isobaths, hydrographical stations and transect numbers are indicated.*

The SeaWIFS satellite pictures of sea surface chlorophyll (Figure 4.10a) reveals a tongue of increased amount of chlorophyll in the surface layer, located from the south-eastern corner of the island and south-westwards. This tongue is more evident in the end of August and in the beginning of September than in the rest of the cruise period (not shown). From September the 4th (not shown) the high amounts of surface chlorophyll seems to be limited to the shelf areas. The maximum surface chlorophyll is measured at the south-eastern corner of the island and just north of the inner part of transect 6. There could also vaguely be seen some increased values of chlorophyll in the surface layer in the inner part of transect 7, and in the bay

outside Nosy Mangabe (15°30'S).

The NPP of phytoplankton through the entire water column (Figure 4.10b), calculated by using the Behrenfeld model (Behrenfeld & Falkowski, 1997b,a), shows the same pattern as the observed surface chlorophyll, and will not be discussed further in this thesis.

The measured SSF (Figure 3.10) shows in general the same pattern as the measurements from the SeaWIFS (Figure 4.10a). This indicates that the thermosalinograph fluorescence measurements carried out during the cruise are relatively representative for the situation at the eastern coast of Madagascar from the end of August to the beginning of October. It also verifies the satellite data. As the chlorophyll is the lowest level in the food chain, it is directly linked to the physical processes.

4.3.2 The Southern Coast

The relatively high concentrations of chlorophyll in the surface layer of the southern coast (Figure 4.10a) could be related to the observed upwelling in this region (Section 4.2). The southern shelf is relatively wide and shallow, and the patterns in salinity and temperature of hydrographical transect 3 (Figure 3.17a and 3.17c) show a well-mixed water column at the inner part of the shelf. Even though the the fluorescence is higher offshore, it is seen in the hydrographical transect of fluorescence (Figure 3.17d) that the amount of fluorescence in the inner part of the shelf is slightly increased related to the surrounding water. The relatively wide and shallow shelf also increases the area where the thickness of the water column is thinner than the mixed layer. As the nutrients are unable to sink out of the mixed layer, this leads to an increased amount of nutrients within this layer, which is favourable for the biological production.

The tongue of relatively low SSS, relatively high SST and high amounts of SSF (Figure 3.8, 3.9 and 3.10) was discussed in Section 4.1.6 to be caused by advection of water south-westwards from the upwelling cell at the south-eastern corner of the island. Cyclonic eddies are generally related to high biological production, due to the shallow pycnocline. The large anticyclonic eddies A1, A2 and A3 (Figure 3.1c) are generally related to low biological production due to a deeper pycnocline. Lower SSF (Figure 3.10) is observed inside A2 and A3 (Figure 3.1c).
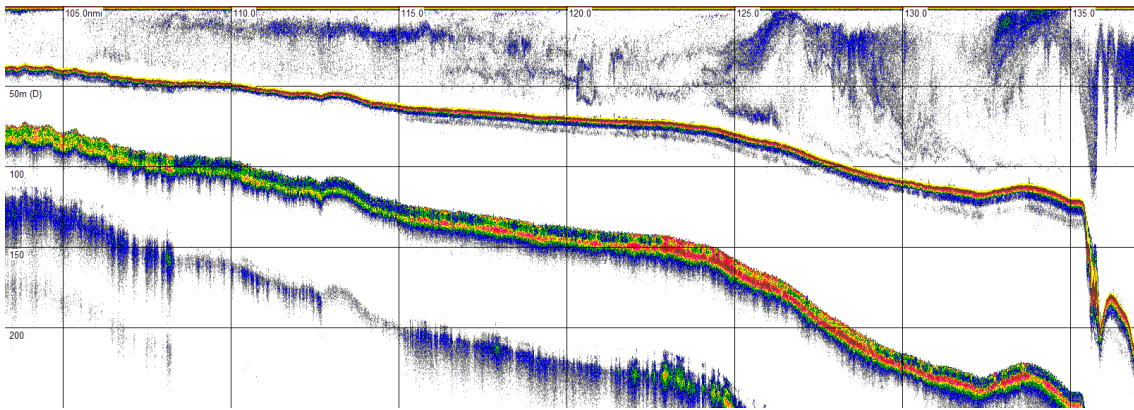
Figure 4.11: *Echogram of the inner part of hydrographical transect 3, Figure 2.1. The biomass through the water column is indicated from the coast to the shelf-break. The shelf is approximately 64.8 kilometers wide and 125 meters deep at the shelf-break (Krakstad, 2011, pers. com.).*

The echogram (Figure 4.11) shows the content of zoo plankton and fish in the water column from the inner shelf to the shelf-break along transect 3 (Figure 2.1). The zooplankton is feeding at the phytoplankton, making a close relation between the concentrations of these two groups. An increased concentration of zoo plankton is observed above the shelf-break and just inside it. The echogram was carried out by the SIMRAD ER 60 Echo sounder (Krakstad *et al.*, 2008).

Figure 4.11 also reveals wave like patterns in the high concentration of zoo plankton right above the shelf-break. This could possibly be explained by internal waves generated at the shelf-break. These waves would contribute to an increased biological production, as they act like nutrient pumps. However, by plotting the potential density of the transect and the density profiles inside and at the shelf-break (Figure 4.12), it is seen that the water column is well mixed on the shelf. Hence, there are no sharp pycnocline for the internal waves to be generated at. The only station with an observed pycnocline is station 877 (Figure 4.12b) which is located outside the shelf-break. It should be noted that the wave-like pattern follows the exact same pattern as the bathymetry, hence, it could possibly be caused by topographical effects.

Many fish species feed on the zooplankton. This makes a certain coherence between the plankton production and the fish production, but this is not absolute, as the fish are on a higher trophic level (Sundby, 2010, pers. com.). At the south-eastern corner of Madagascar, it is seen that the largest amounts of fish are found south-west (downstream) of the maximum phytoplankton production (Figure 4.13 and 4.14). The fish are usually feeding at the edge of the cores of high concentration of zoo-
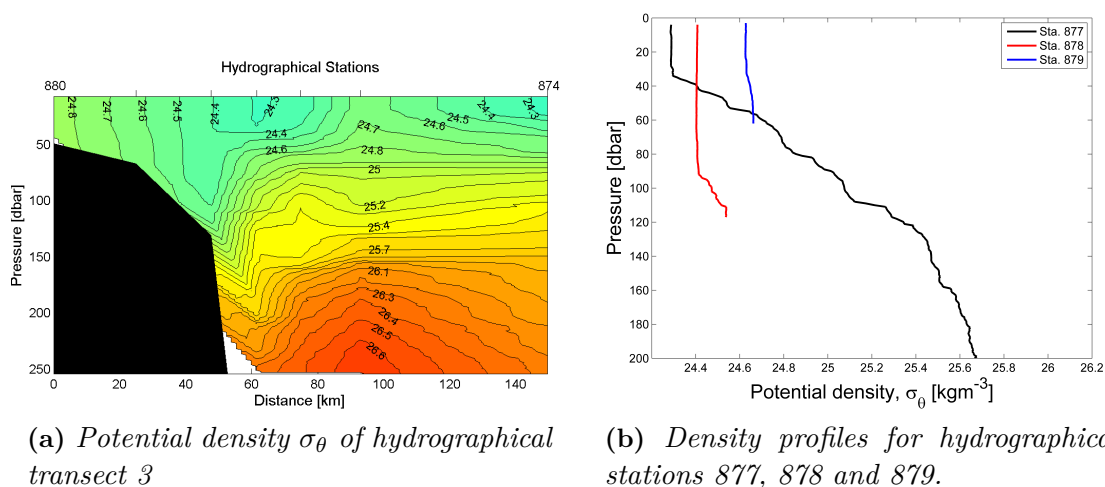
(a) *Potential density σ$_\theta$ of hydrographical transect 3*

(b) *Density profiles for hydrographical stations 877, 878 and 879.*

Figure 4.12: *(a) Vertical distribution of potential density, transect 3 (b) Potential density profiles of hydrographical station 877, 878 and 879. Station 879 is located closest to the coast, while 877 is farthest away from the coast.*

and phytoplankton, while the zooplankton are feeding at the edge of the cores of high concentration of phytoplankton.

In this section, Clupeoids will be referred to as Pelagic 1 while Carangids, Scombrids, Leiognathids and associated pelagic are referred to as Pelagic 2. Pelagic species usually form schools and have a diurnal vertical migration pattern (Sætre *et al.*, 1983). Pelagic 1 is the one of these two that is strongest related to high productivity as found in e.g. upwelling regions.

Table 4.4: *Acoustic estimates of Pelagic 1 and 2 (Krakstad* et al.*, 2008).*

Area	Biomass: Pelagic 1 [t]	Biomass: Pelagic 2 [t]
South	15 000	54 000
South-east	-	9 000
North-east	-	14 000

Table 4.4 reveals relatively large amounts of fish at the southern shelf, and both Pelagic 1 and 2 are represented. As seen in Figure 4.13 and 4.14, the patches of fish are larger at the southern coast compared to the south-eastern and north-eastern coasts (Figure 4.16 and 4.19). The estimated total amounts of biomass is estimated based on the echograms and an integration technique. The Large Scale Survey

System (LSSS) from Marec was used for integration (Krakstad *et al.*, 2008). The estimated biomass at the southern shelf is 69 000 tons, about 7 times the amount measured at the south-eastern coast, and about 5 times the amount of biomass measured at the north-eastern coast. These estimates include pelagic species only.
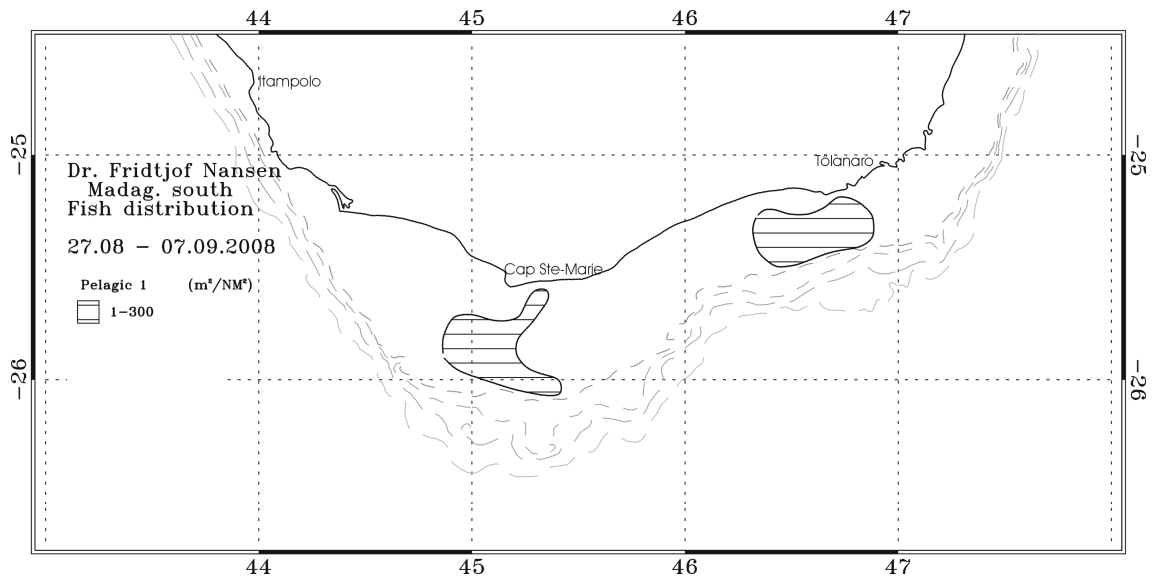
Figure 4.13: *Distribution of Pelagic 1 on the southern shelf of Madagascar (Krakstad* et al.*, 2008).*
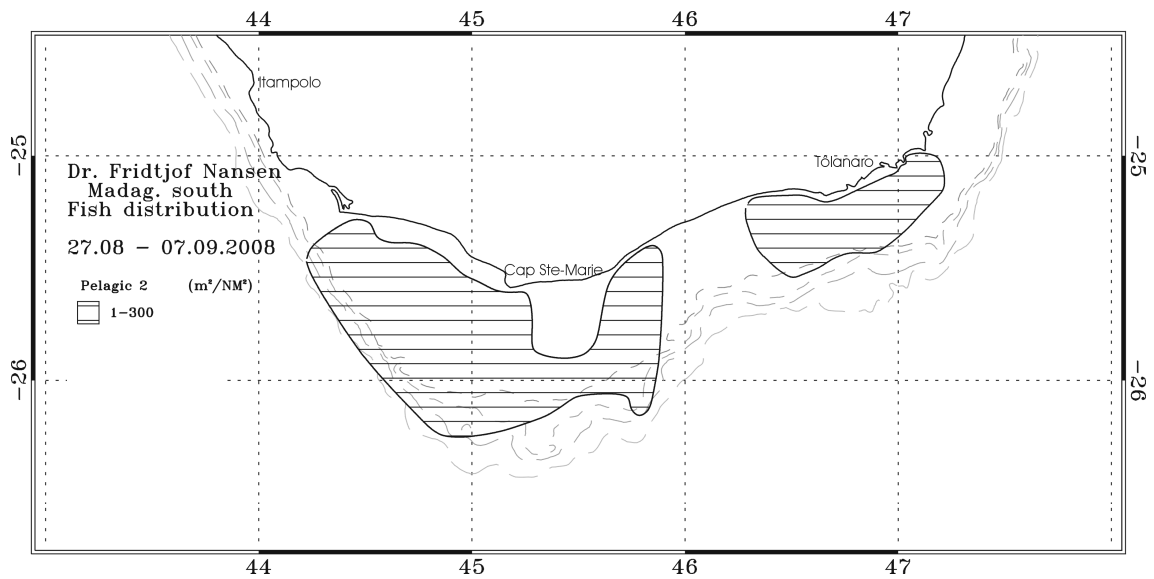

Figure 4.14: *Distribution of Pelagic 2 on the southern shelf of Madagascar (Krakstad* et al.*, 2008).*

During the cruise, frequent sighting of humpback whales, *Megaptera novaeangliae*, were made at the southern coast. The whales were observed closest to the coast, in the coastal upwelling zone. This was also the area of highest biological production. According to Krakstad *et al.* (2008), the southern and south-eastern coasts of Madagascar are well known from literature to have a high abundance of humpback whales at this time of the year. Whales observed were generally distributed on the shelf to maximum 50 meters depth and offshore, in the vicinity of the shelf-break,

all the way north to Toamasina (20°S) at the south-eastern coast. The number of observations was decreasing northwards (Krakstad *et al.*, 2008).

4.3.3   The South-eastern Coast

The content of observed SSF and surface chlorophyll (Figure 3.10 and 4.10a) is decreasing northwards along the south-eastern coast, as the strength of the upwelling decreases northwards (Section 4.2). At the south-eastern corner of the island, a biological hotspot is observed both in the hydrographical transect of fluorescence in transect 5 (Figure 3.18d), in the horizontal distribution of SSF (Figure 3.10) and in the horizontal distribution of sea surface chlorophyll carried out by SeaWIFS (Figure 4.10a). Both strong coastal and strong shelf-break upwelling was observed in this region, in addition to the theory of the divergence of the EMC leading to a strong upwelling cell (Section 4.2). The hydrographical transects of salinity and temperature (Figure 3.18a and 3.18c) also indicate a front above the shelf-break. This is probably a shelf-break front with the strongest temperature and salinity gradients right above the shelf-break. This front could be set up as a consequence of the topographically steered southwards directed branch of the EMC. Such fronts are connected to high biological production due to concentration of the nutrients. High concentrations of fluorescence (Figure 3.18d) are observed in the surface layer, right above the front.

The horizontal distribution of SSS (Figure 3.8) shows low values of salinity closest to the coast of transects 6 and 7, indicating fresh water run-off. The largest river of the eastern coast, the Mangoro river, has its outlet in the inner part of transect 7 (~20°S). This might explain the increased SSF (Figure 3.10) observed between transect 7 and 8, but it does not explain the deviation between the SeaWIFS pictures (Figure 4.10a) and the measured SSF (Figure 3.10) south of transect 7. This can possibly be explained by interanual variations.

The echogram of transect 6 (Figure 4.15) shows that the shelf rises at the shelf-break, before it breaks into the deep ocean. This ridge at the shelf-break is, according to Krakstad (2011, pers. com.), recognized as coral reefs, and they are observed more or less at the shelf-break along the entire eastern coast of Madagascar. The coral reefs filter the water, consuming phytoplankton. As the coral reefs are stationary, they need turbulence to increase the flow through the reef. This is obtained at the
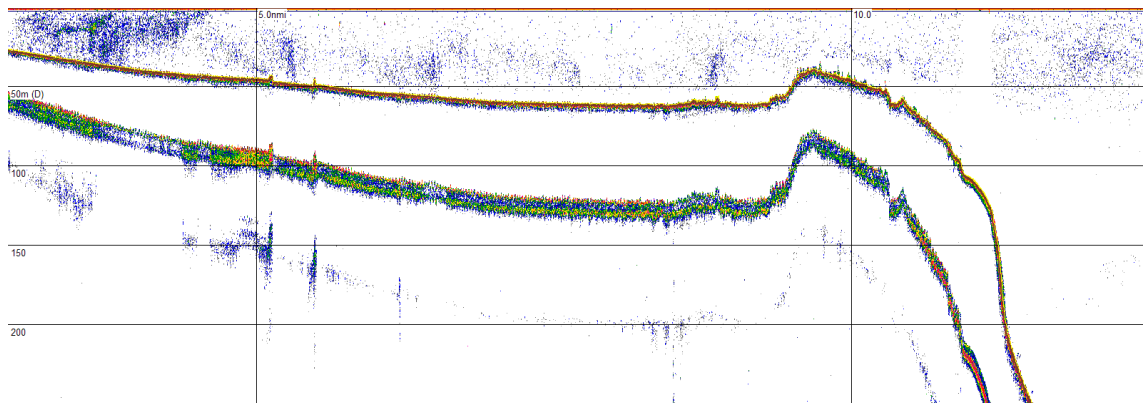
Figure 4.15: *Echogram of the inner part of hydrographical transect 6, Figure 2.1. The biomass through the water column is indicated from the coast to the shelf-break. The shelf is approximately 16 kilometers wide and 50 meter deep at the shelf-break (Krakstad, 2011, pers. com.).*

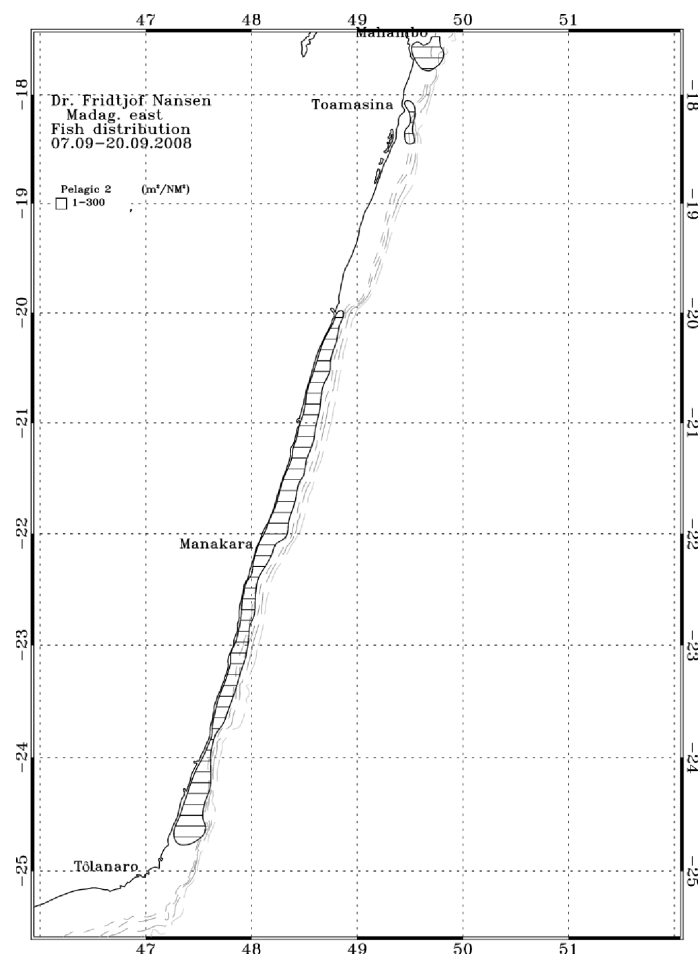shelf-break, where both tides, currents and internal waves generate turbulence.

Figure 4.16: *Distribution of Pelagic 2 on the south-eastern shelf of Madagascar (Krakstad et al., 2008).*

The density of Pelagic 2 (Figure 4.16) was decreasing northwards along the south-eastern coast. In the same region it was seen that the strength of the upwelling was decreasing. It should be noted that the outlet of Mangoro ($\sim$20°S) defines the northern boundary of the patch of increased density of fish in the south-eastern region.

4.3.4   The North-eastern Coast

At the north-eastern coast, low values of fluorescence are observed in the entire region (Figure 3.10). Even though the thermosalinoraph showed no SSF maximum (Figure 3.10), the decadal averaged SeaWIFS images 1998 - 2007 (Figure 4.10a) show increased values of surface chlorophyll in the bay just south of Nosy Mangabe, and around Ile Sainete-marie (island at 17°S).

Both coastal and shelf-break downwelling were observed at the north-eastern coast (Section 4.2). Even though this downwelling was weak (Figure 3.19a and 3.19c), as a result of weak wind (Figure 3.7) and currents (Figure 3.1a), it is not preferable for biological production.

The total estimated biomass of this region (14 000 tons) is greater than the total estimated biomass of the south-eastern region (9 000 tons). This could partly be explained by the wider ($\sim$45 kilometers) and shallower ($\sim$60 meters) shelf observed in the echogram of transect 10 (not shown). The main explanation however, seems to be discharge of fresh and nutrient rich water from the rivers. This is observed both in the horizontal distribution of SSS (Figure 3.8), and the hydrographical transect of salinity (Figure 3.19a). It also looks like the relatively fresh and nutrient rich surface water is advected northwards by the northwards directed branch of the EMC, but it is difficult to be certain due to missing measurements in this area. It could also be seen from the hydrographical transect of temperature (Figure 3.19c), that it is slightly colder at the very inner part of the shelf, related to the low salinities. Discharge of water from the rivers could increase the content of nutrients with several orders of magnitude (Bakun, 1996). The increase of nutrients in the surface water might explain the relatively high concentration of fish in this region.

By plotting hydrographical profiles of fluorescence, oxygen and temperature of station 942 (Figure 4.17), a maximum in the oxygen is observed in the same layer as the maximum fluorescence. This indicates that the phytoplankton is producing oxygen through photosynthesis. The upper zone of the thermocline is often related to a
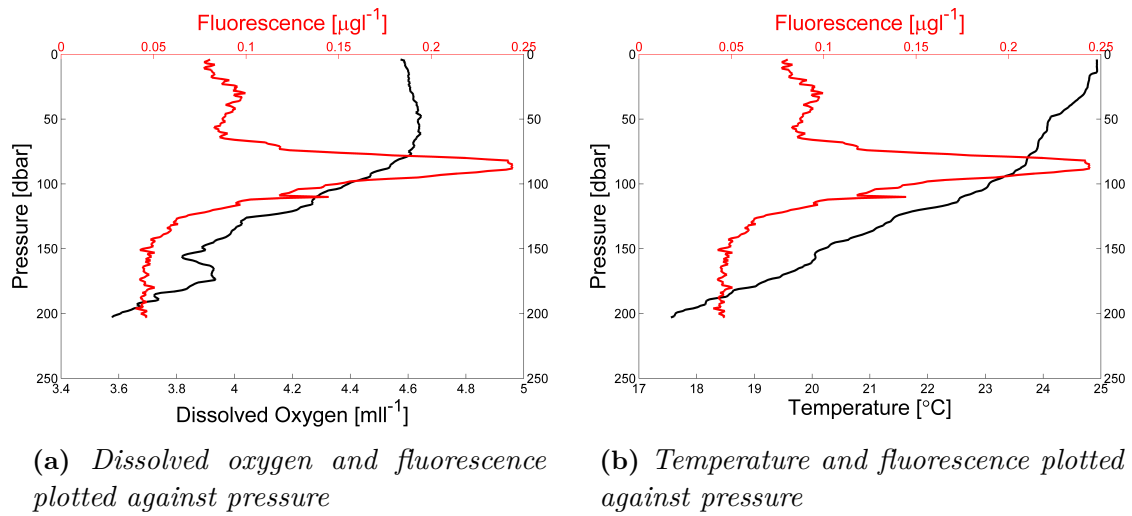
(a) *Dissolved oxygen and fluorescence plotted against pressure*

(b) *Temperature and fluorescence plotted against pressure*

Figure 4.17: *(a) Dissolved oxygen and fluorescence plotted against pressure and (b) Temperature and fluorescence plotted against pressure for the upper 200 meters of hydrographical station 942 (Figure 2.1) located between the 1000 and 2000 meters isobath in transect 10 at the north-eastern coast.*
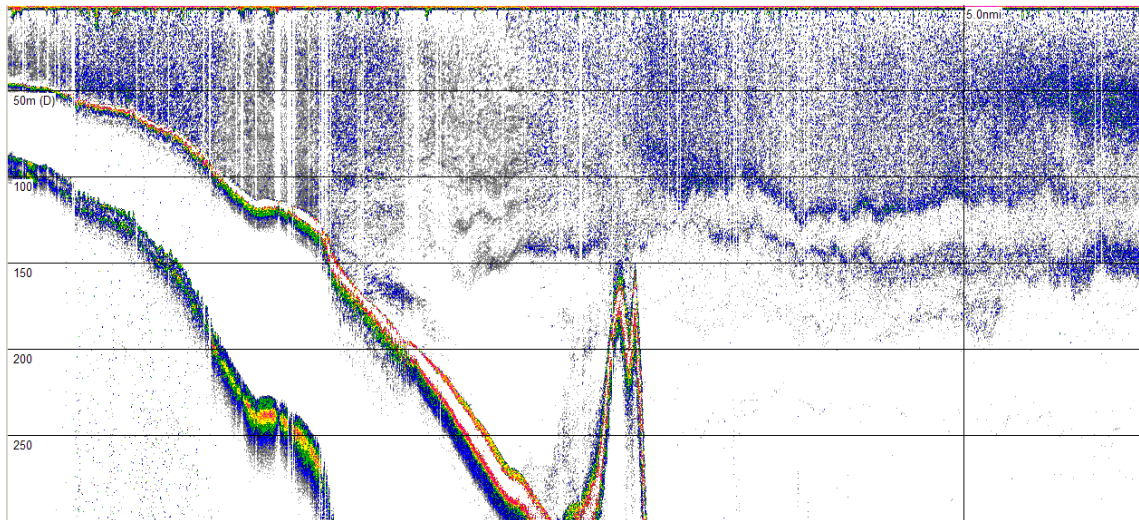
sharp nutricline.

Figure 4.18: *Echogram of the inner part of hydrographical transect 12, Figure 2.1. The biomass through the water column is indicated from the coast to the shelf-break. The shelf is approximately 7 kilometers wide and 150 meters deep at the shelf-break (Krakstad, 2011, pers. com.).*

The biomass estimates of the north-eastern coast (Figure 4.19) show a patch of relatively high density of Pelagic 2 between 16°S and 17.5°S, south of the mouth of Nosy Mangabe. This patch coincides very well with the patch of low SSS (Figure
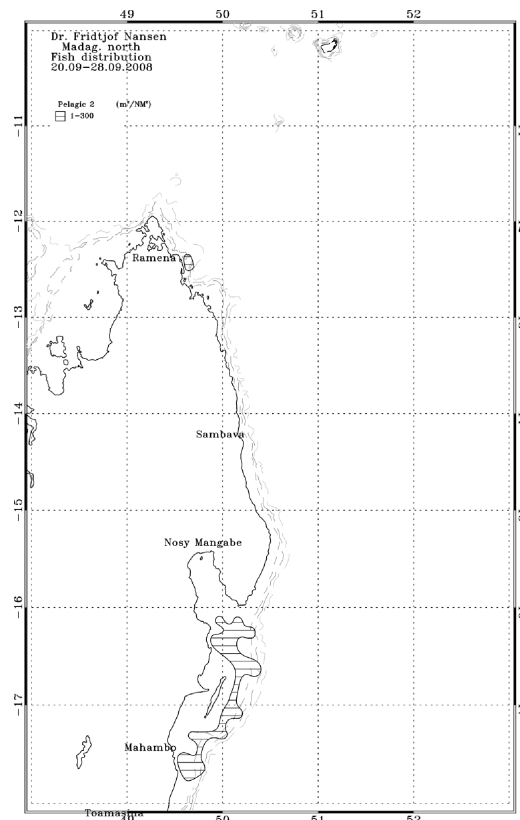
Figure 4.19: *Distribution of Pelagic 2 on the north-eastern shelf of Madagascar (Krakstad* et al.*, 2008).*

3.8).

According to Krakstad (2011, pers. com.), the composition of species north of the bifurcation of the SEC ($\sim$19°S) is different from the composition south of it. The environmental parameters of these areas are different, and they could possibly be considered as different biological subregions.

It seems to be possible to describe the main pattern in the biological production associated with the southern and eastern shelf of Madagascar with a gradient directed north-south with relatively high production at the southern coast, and relatively low production at the northern coast. The maximum concentration of fish is generally situated at the shelf-break, usually in the depression inside the coral reefs (Krakstad, 2011, pers. com.).

Chapter 5

Summary and Future Work

The zonal SEC hits the eastern coast of Madagascar at ∼19°S (Figure 3.1). The location of the SEC might be explained by the Sverdrup theory using the mean monthly MERRA wind (Figure 3.7). When the current hits the coast, it bifurcates into a northwards and a southwards directed branch of the EMC. The bifurcation seems to be forced by the wind system. Ekman transport towards the coast north of the bifurcation, and away from the coast south of the bifurcation, leads to geostrophic balanced currents both southwards and northwards. Conservation of potential vorticity could contribute to the explanation of the northwards directed current, and the need of a strong southwards directed western boundary current for the vorticity balance in the southern Indian Ocean to be fulfilled, could explain the southwards directed current. The southwards directed branch acts like a relatively strong (up to 150 cms^{-1}) topographically steered narrow western boundary current, with a volume transport of ∼26 Sv in the upper 3000 meters of the inner 136 kilometers of transect 5 (∼25°S).

At the south-eastern corner of Madagascar, the EMC leaves the south-eastern coast, and some of it seems to retroflect. This retroflection can possibly be explained by inertial motion, or conservation of potential vorticity. The southwards directed branch of the EMC is increasing in strength southwards along the coast, indicating that the retroflection acts like a stationary eddy, feeding the EMC with water. The retroflection is together with the bathymetry also expected to be the reason for the distinct separation between the deep (>2000 meters) water masses of the southern and south-eastern region. The generation of eddies at the southern coast seems to be related to the retroflection of the EMC. The anticyclonic eddies are shed off when

the current retroflects, while the cyclonic eddies are inducted inside the EMC due to friction towards the coast. The eddies are travelling south-westwards through the southern region, towards the African coast, feeding the Agulhas current with water (de Ruijter *et al.*, 2004; Quartly *et al.*, 2006). The anticyclonic eddies are related to downwelling patterns with a deep pycnocline, while the smaller cyclonic eddies are related to upwelling patterns and a shallow pycnocline. The part of the EMC that does not retroflect seems to be directed south-westwards into the southern region. It advects relatively fresh, warm and high fluorescence water from the south-eastern corner of the island into the southern region.

The currents of the northwards directed branch of the EMC are weaker (up to 60 cms^{-1}) just north of the bifurcation, but accelerate between 13.5°S and 12°S (Figure 3.1a). The volume transports are increasing between transect 11 and 12. The northwards directed branch of the EMC is supported by another incoming branch of the SEC, reaching the coast between ∼13.5°S - 12°S, following the EMC northwards around the northern tip of the island into the Mozambique Channel. This second branch of the EMC was also observed in a run of ROMS (Figure 4.2) at the same time of the year, in 1996. The north-westwards directed volume transport through the upper 3000 meters of the inner 142 kilometers of transect 12 (∼12°S), is calculated to 62 Sv, after adjusting the geostrophic profiles with the ADCP measurements at the reference level (176 meters).

Upwelling is observed on the shelf of the southern and south-eastern coasts. The upwelling at the southern coast seems to be mainly wind-driven, while the upwelling at the south-eastern coast seems to be stronger and driven by both the wind and the currents. The strongest upwelling (down to ∼130 meters depth) is observed at the south-eastern corner of the island. In this region, the bathytmetry changes dramatically, and the EMC is expected to diverge, explaining the increased upwelling. The north-eastern coast is related to down-welling patterns, with both the mean monthly MERRRA wind and the currents directed northwards, both leading to downwelling.

A close relation is observed between the physical processes and the biological response. Upwelling has turned out to be the most important physical factor stimulating biological production at the southern and south-eastern coasts. The north-eastern shelf is related to downwelling. Discharge of nutrient-rich water from the rivers seems to be the most important factor explaining the biological production in the north-eastern region. In addition, the width and depth of the shelf have also turned out to be important factors in determining the biological production along

the entire coast. A north-south gradient seem to be describing the biological production on the eastern shelf of Madagascar, with relatively large production in the southern region, and relatively low production in the northern region. The incoming southern branch of the SEC (∼19°S) seems to act like a sharp boundary when it comes to the composition of species. The environmental parameters of these areas are different, and they could possibly be considered as biological subregions.

In future studies of the East Madagscar Current System it would be interesting to carry out a meridional transect ∼200 kilometers off coast from ∼10°S - 21°S. This would be in order to gain better understanding of the incoming SEC. It would also be interesting to carry out one more transect south-eastwards from the south-eastern corner of the island. This would contribute to a better understanding of the retroflection of the EMC.

Bibliography

Aldegheri, M. 1972. Rivers and streams on Madagascar. *Biogeography and Ecology in Madagascar Dr. W. Junk Publishers, The Hague*, 261–310.

Backeberg, B.C., & Reason, C.J.C. 2010. A connection between the South Equatorial Current north of Madagascar and Mozambique Channel Eddies. *Geophysical Research Letters*, **37**(4), L04604.

Bakun, A. 1996. *Patterns in the ocean: ocean processes and marine population dynamics*. California Sea Grant College System. 323 pp.

Bearman, G., Brown, J., & Colling, A. 2004. *Ocean circulation*. Butterworth Heinemann in assosiation with The Open University. 286 pp.

Behrenfeld, M.J., & Falkowski, P.G. 1997a. A consumer's guide to phytoplankton primary productivity models. *Limnology and Oceanography*, **42**(7), 1479–1491.

Behrenfeld, M.J., & Falkowski, P.G. 1997b. Photosynthetic rates derived from satellite-based chlorophyll concentration. *Limnology and oceanography*, **42**(1), 1–20.

Brown, E., & Bearman, G. 2006. *Waves, Tides and Shallow-Water Processes*. Butterworth Heinemann in assosiation with The Open University. 227 pp.

Center for Sustainability and the Global Environment. 2010. *Global River Discharge Database*. Available at <`http://www.sage.wisc.edu/riverdata/`> [Downloaded May the 5th, 2011].

Chelsea Technologies. 2008. *AQUAtracka III In-situ fluorimeter, nephelometer*. Available at <`http://www.chelsea.co.uk/Factsheets/AQUAtrackaJuly08.pdf`> [Downloaded June the 2nd, 2010].

Cushman-Roisin, B., & Beckers, J.M. 2009. *Introduction to Geophysical Fluid Dynamics Physical and Numerical Aspects.* Academic Press. 774 pp.

de Ruijter, W.P.M., Aken, H.M., Beier, E.J., Lutjeharms, J.R.E., Matano, R.P., & Schouten, M.W. 2004. Eddies and dipoles around South Madagascar: formation, pathways and large-scale impact. *Deep Sea Research Part I: Oceanographic Research Papers*, **51**(3), 383–400.

Dickson, R.R., & Brown, J. 1994. The production of North Atlantic Deep Water: sources, rates, and pathways. *Journal of Geophysical Research*, **99**(C6), 12.319–12.341.

DiMarco, S.F., Chapman, P., & Nowlin Jr, W.D. 2000. Satellite observations of upwelling on the continental shelf south of Madagascar. *Geophysical research letters*, **27**(24), 3965–3968.

DiMarco, S.F., Chapman, P., Nowlin, W.D., *et al.* 2002. Volume transport and property distributions of the Mozambique Channel. *Deep Sea Research Part II: Topical Studies in Oceanography*, **49**(7-8), 1481–1511.

Donohue, K.A., & Toole, J.M. 2003. A near-synoptic survey of the Southwest Indian Ocean. *Deep-Sea Research*, **2**, 1883–1931.

EAF-Nansen. 2011. *EAF-Nansen Homepage.* Available at <`http://www.eaf-nansen.org/nansen/en`> [Downloaded May the 20th, 2011].

Egbert, G.D., & Erofeeva, S.Y. 2002. Efficient inverse modeling of barotropic ocean tides. *Journal of Atmospheric and Oceanic Technology*, **19**(2), 183–204.

Gill, A.E., & Schumann, E.H. 1979. Topographically induced changes in the structure of an inertial coastal jet Application to the Agulhas Current. *Journal of Physical Oceanography*, **9**, 975–991.

Global Modeling and Assimilation Office (GMAO). 2010. *MERRA: Modern Era Retrospective-Aanalysis for Research and Applications.* NASA Goddard Space Flight Center.

Gründlingh, M.L., Carter, R.A., & Stanton, R.C. 1991. Circulation and water properties of the southwest Indian Ocean, spring 1987. *Progress in Oceanography*, **28**(4), 305–342.

Ho, C.R., Zheng, Q., & Kuo, N.J. 2004. SeaWiFs observations of upwelling south of Madagascar: long-term variability and interaction with East Madagascar Current. *Deep Sea Research Part II: Topical Studies in Oceanography*, **51**(1-3), 59–67.

Inocência, P. A. 2011. *Validating the TMD model using tide gauges along the Mozambican coast.* Term paper, Dynamical Oceanography II, Eduardo Mondlane University, Mozambique.

IOC, IHO and BODC. 2003. *Centenary Edition of the GEBCO Digital Atlas, published on CD-ROM on behalf of the Intergovernmental Oceanographic Commission and the International Hydrographic Organization as part of the General Bathymetric Chart of the Oceans.* British Oceanographic Data Centre, Liverpool, U.K.

Krakstad, J.O., Mehl, S., Roman, R.E., Escobar-Porras, J., Stapley, J., Flynn, B., Olsen, M., & Beck, I.M. 2008. *East Madagascar Current Ecosystem Survey, 23 August - 01 October 2008.* Cruise reports, 'Dr. Fridtjof Nansen'. NORAD/FAO Project GCP/INT/730/NOR.

Lutjeharms, J.R.E. 2006. The coastal oceans of south-eastern Africa. *The Sea*, **14B**, 783–834.

Lutjeharms, J.R.E., & de Ruijter, W.P.M. 1996. The influence of the Agulhas Current on the adjacent coastal ocean: possible impacts of climate change. *Journal of Marine Systems*, **7**(2-4), 321–336.

Lutjeharms, J.R.E., & Machu, E. 2000. An upwelling cell inshore of the East Madagascar Current. *Deep-Sea Research Part I*, **47**(12), 2405–2411.

Lutjeharms, J.R.E., Bang, N.D., & Duncan, C.P. 1981. Characteristics of the currents east and south of Madagascar. *Deep Sea Research Part I: Oceanographic Research*, **28**, 879–899.

Mann, K.H., & Lazier, J.R.N. 2006. *Dynamics of marine ecosystems: biological-physical interactions in the oceans.* Blackwell publishing. 496 pp.

Maps of the World. 2011. *Madagascar Rivers.* Available at <`http://mapsof.net/ madagascar/static-maps/png/madagascar-rivers`> [Downloaded May the 5th, 2011].

Ostrowski, M. 2005. *Benefit Surveys Angola.* Cruise reports, 'Dr. Fridtjof Nansen', Institute of Marine Research, Bergen.

Park, Y.H., Gamberoni, L., & Charriaud, E. 1993. Frontal structure, water masses, and circulation in the Crozet Basin. *Journal of Geophysical Research*, **98**(C7), 12361–12.

Penven, P., Lutjeharms, JRE, & Florenchie, P. 2006. Madagascar: A pacemaker for the Agulhas Current system. *Geophysical Research Letters*, **33**, L17609.

Pingree, R.D., Pugh, P.R., Holligan, P.M., & Forster, G.R. 1975. Summer phytoplankton blooms and red tides along tidal fronts in the approaches to the English Channel. *Nature*, **258**, 672–677.

Pond, S., & Pickard, G.L. 2007. *Introductory dynamical oceanography.* Butterworth Heineman. 329 pp.

Pripp, T.E.B. 2011. *Physical influence on the biological production along the western coast of Madagascar.* Masters's Thesis, Geophysical Institute, University of Bergen.

Quadfasel, D.R., & Swallow, J.C. 1986. Evidence for 50-day period planetary waves in the South Equatorial Current of the Indian Ocean. *Deep Sea Research Part A. Oceanographic Research Papers*, **33**(10), 1307–1312.

Quartly, G.D., Buck, J.J.H., Srokosz, M.A., & Coward, A.C. 2006. Eddies around Madagascar–The retroflection re-considered. *Journal of Marine Systems*, **63**(3-4), 115–129.

Read, J.F., & Pollard, R.T. 1993. Structure and transport of the Antarctic circumpolar current and Agulhas return current at 40 E. *Journal of Geophysical Research*, **98**(C7), 12281.

Roman, R.E., & Lutjeharms, J.R.E. 2007. Red Sea Intermediate Water at the Agulhas Current termination. *Deep Sea Research Part I: Oceanographic Research Papers*, **54**(8), 1329–1340.

Sætre, R., & Da Silva, A.J. 1984. The circulation of the Mozambique Channel. *Deep Sea Research Part A. Oceanographic Research Papers*, **31**(5), 485–508.

Sætre, R., Strømsnes, K., Hansen, K., Abrahamsen, H., Schmidt, G., & Rakotondralambo, A. 1983. *Fisheries resources survey Madagascar, 16-28 June 1983.* Cruise reports, 'Dr. Fridtjof Nansen', Institute of Marine Research, Bergen.

Schott, F., Fieux, M., Kindle, J., Swallow, J., & Zantopp, R. 1988. The boundary currents east and north of Madagascar 2. Direct measurements and model comparisons. *Journal of Geophysical Research*, **93**(C5), 4963–4974.

Sea-Bird Electronics. 2003. *SEASOFT-Win32:SBE Data Processing.* Available at <`http://www.seabird.com`> [Downloaded June the 2nd, 2010].

Sea-Bird Electronics. 2010a. *Premium CTD Temperature Sensor SBE 3plus, Conductivity Sensor SBE 4, Dissolved Oxygen (DO) Sensor SBE 43.* Available at <`http://www.seabird.com`> [Downloaded June the 2nd, 2010].

Sea-Bird Electronics. 2010b. *SEACAT Thermosalinograph SBE 21.* Available at <`http://www.seabird.com`> [Downloaded June the 2nd, 2010].

Sundby, S. 1997. Turbulence and ichthyoplankton: influence on vertical distributions and encounter rates. *Scientia Marina*, **61**, 159–176.

Swallow, J., Fieux, M., & Schott, F. 1988. The boundary currents east and north of Madagascar 1. Geostrophic currents and transports. *Journal of Geophysical Research*, **93**(C5), 4951–4962.

Talley, L.D., & Sprintall, J. 2005. Deep expression of the Indonesian Throughflow: Indonesian intermediate water in the South Equatorial Current. *Journal of Geophysical Research*, **110**, 2004–2006.

Teledyne RD Instruments. 2000. *VmDas User's Guide.* Available at <`http://www.comm-tec.com/prods/mfgs/RDI/Software/Manuals/VMDAS-Manual/VmDas\%20Users\%20Guide.pdf`>[DownloadedMarchthe23rd,2010],.

Teledyne RD Instruments. 2001. *WinADCP User's Guide.* Available at <`http://www.comm-tec.com/prods/mfgs/RDI/Software/Manuals/WinADCP-Manual/WinADCP\%20User\%20Guide.pdf`> [Downloaded March the 23rd, 2010].

Teledyne RD Instruments. 2008. *Ocean Surveyor Vessel-Mount ADCP.* Available at <`http://rdinstruments.com/`> [Downloaded March the 23rd, 2010].

Tomczak, M., & Godfrey, J.S. 2003. *Regional oceanography: an introduction.* Daya Books. 402 pp.

Wright, P.C. 1999. Lemur traits and Madagascar ecology: coping with an island environment. *Yearbook of Physical Anthropology*, **42**, 31–72.

You, Y., Lutjeharms, J.R.E., Boebel, O., & de Ruijter, W.P.M. 2003. Quantification
of the interocean exchange of intermediate water masses around southern Africa.
Deep Sea Research Part II: Topical Studies in Oceanography, **50**(1), 197–228.